UNIVERSITÀ DEGLI STUDI DI UDINE

Corso di Dottorato di Ricerca in Ingegneria Industriale e dell'Informazione
Ciclo XXV

Tesi di Dottorato di Ricerca

DIRECTION OF ARRIVAL ESTIMATION FOR RADIO POSITIONING: A HARDWARE IMPLEMENTATION PERSPECTIVE

Dottorando
DANIELE INSERRA

Nome del Relatore
Prof. ANDREA M. TONELLO

Dicembre 2012

ANNO ACCADEMICO
2012/2013

to Sara, Elisabetta and Michele

Acknowledgements

I would like to acknowledge all the people who have shared with me these four years. Firstly, I'm grateful to my tutor, prof. A. Tonello, for introducing me into the radio communication world, and for giving me the possibility to do that from a hardware implementation perspective. Furthermore, I would like to thank him for the opportunity to become a member of his research group. This has enriched me as engineer from a professional experience point of view, and, the possibility to work in the WiPLi Lab (a very well equipped laboratory), has stimulated in me the interest and the passion to the RF and microwave issues. In this respect, I have to mention prof. P. Palestri, M. Midrio, and S. Boscolo for their support in solving my doubts concerning these subjects.

I would also like to thank prof. Markus Rupp and prof. Letizia Lo Presti for their helpful comments and suggestions that have surely improved this work in many aspects.

A special thank goes to my collegues, the WiPLi Lab members, who have shared with me these four years: the veterans M. Bellin and F. Pecile, the more expert Nicola and Salvatore, the meteors A. Omenetto and E. Paron, the graduating students F. Iannacone, S. Martella, and G. Brajnik, the new entry A. Pittolo, the "others" L. Celetto, A. Sebastianutti and R. Cesco Fabbro, and my fellows Massimo, Fabio, Marco, Luca, and Mauro.

The bigger thank goes to my family, to Sara, Elisabetta and Michele, to God who has given them to me, to my parents, my brothers and sisters. They have always helped me to give the right weight to the things, although sometimes I did not, and to see to the deeper meaning of life.

Finally, I acknowledge that part of the work herein presented was funded by CNIT, Consorzio Nazionale Interuniversitario per le Telecomunicazioni, with a doctoral research grant, and DM Elektron S.p.A..

Daniele Inserra *Udine, December 2012*

Contents

List of Tables

List of Figures

List of Acronyms

AAF anti-aliasing filter

ADC analog to digital converter

AGC automatic gain control

AM amplitude modulation

AoA angle of arrival

AP access point

API application programming interface

AS angular spread

ASK amplitude shift keying

AWGN additive white Gaussian noise

BS base station

BSF band select filter

CFO carrier frequency offset

CIR channel impulse response

CMX code-multiplexed

CP cyclic prefix

cPCI compact peripheral component interconnect

CPLD complex programmable logic device

CSF channel select filter

DANL display average noise level

DC direct current

DF direction finding

DoA direction of arrival

DSP digital signal processing

ENOB effective number of bits

ESPRIT estimation of signal parameters via rotational invariance

FAP first arrival path

FE front-end

FFT fast Fourier transform

FM frequency modulation

FMX frequency-multiplexed

FP full-parallel (uncoherent)

FPC full-parallel coherent

FPGA field-programmable gate array

FSK frequency shift keying

GNSS global navigation satellite system

GPIO general purpose input/output

GPS global positioning system

GS gain setting

ICI inter-carrier interference

IF intermediate frequency

IFFT inverse fast Fourier transform

ISI inter-symbol interference

ISM industrial, scientific and medical

LES linearly equispaced

LTE long term evolution

LNA low noise amplifier

LO local oscillator

LOS line-of-sight

MIMO multiple-input multiple-output

ML maximum likelihood

MMCX micro-miniature coaxial

MMSE minimum mean squared error

MUSIC multiple signal classification

MP multipath

MPC multipath component

MS mobile station

NF noise figure

NLOS non-line-of-sight

OFDM orthogonal frequency division multiplexing

PC personal computer

PCI peripheral component interconnect

PL path loss

PLL phase-locked loop

PM phase modulation

PN phase noise

PO phase offset

PSK phase shift keying

RBW resolution bandwidth

RF radio frequency

RMS root mean squared

RMSE root mean squared error

RSS received signal strength

RSSI received signal strength indicator

SAW surface acoustic wave

SDR signal to dc offset power ratio

SDRAM synchronous dynamic random access memory

SFDR spurious free dynamic range

SIMO single-input multiple-output

SINAD signal to noise and distortion ratio

SMA subminiature version A

SNR signal to noise ratio

SPDT single-pole double-through

TDoA time difference of arrival

THD total harmonic distortion

TMX time-multiplexed

ToA time of arrival

ToF time of flight

ULA uniform linear array

UWB ultra wideband

VGA variable gain amplifier

VHDL very high-level design language

WLAN wireless local area network

WSN wireless sensor network

ZP zero padding

Abstract

Nowadays multiple antenna wireless systems have gained considerable attention due to their capability to increase performance. Advances in theory have introduced several new schemes that rely on multiple antennas and aim to increase data rate, diversity gain, or to provide multiuser capabilities, beamforming and direction finding (DF) features. In this respect, it has been shown that a multiple antenna receiver can be potentially used to perform radio localization by using the *direction of arrival* (DoA) estimation technique.

In this field, the literature is extensive and gathers the results of almost four decades of research activities. Among the most cited techniques that have been developed, we find the so called high-resolution algorithms, such as multiple signal classification (MUSIC), or estimation of signal parameters via rotational invariance (ESPRIT). Theoretical analysis as well as simulation results have demonstrated their excellent performance to the point that they are usually considered as reference for the comparison with other algorithms. However, such a performance is not necessarily obtained in a real system due to the presence of non idealities. These can be divided into two categories: the impairments due to the antenna array, and the impairments due to the multiple radio frequency (RF) and acquisition front-ends (FEs). The former are strongly influenced by the manufacturing accuracy and, depending on the required DoA resolution, have to be taken into account. Several works address these issues in the literature. The multiple FE non idealities, instead, are usually not considered in the DoA estimation literature, even if they can have a detrimental effect on the performance. This has motivated the research work in this thesis that addresses the problem of DoA estimation from a practical implementation perspective, emphasizing the impact of the hardware impairments on the final performance. This work is substantiated by measurements done on a state-of-the-art hardware platform that have pointed out the presence of non idealities such as DC offsets, phase noise (PN), carrier frequency offsets (CFOs), and phase offsets (POs) among receivers. Particularly, the hardware platform will be herein described and examined to understand what non idealities can affect the DoA estimation performance. This analysis will bring to identify which features a DF system should have to reach certain performance.

Another important issue is the number of antenna elements. In fact, it is usually limited

by practical considerations, such as size, costs, and also complexity. However, the most cited DoA estimation algorithms need a high number of antenna elements, and this does not yield them suitable to be implemented in a real system. Motivated by this consideration, the final part of this work will describe a novel DoA estimation algorithm that can be used when multipath propagation occurs. This algorithm does not need a high number of antenna elements to be implemented, and it shows good performance despite its low implementation/computational complexity.

Chapter 1

Introduction

In this chapter, we describe the radio positioning systems, and, in particular, we introduce the DoA estimation problem that will be the subject of this work. Then, we give an overview on the thesis organization. More precisely, Section 1.1 treats the problem of localization by using radio techniques, and describes several methods that rely on different wave propagation properties. In Section 1.2, we set the objectives of the thesis and we give a brief outline. Finally, the list of the papers where part of the work of this thesis has been published is provided in Section 1.3.

1.1 Radio Positioning Systems

Over the past few decades, many types of radio positioning and/or navigation systems have been developed. The most famous example is the global navigation satellite system (GNSS) and its implementations: the United States global positioning system (GPS), GLONASS for the Russian government, and, more recently, the European GALILEO system.

GNSS, unfortunately, has some limitations, e.g., the lack of coverage into buildings [1]. Another shortcoming is the need of additional hardware that in some applications, as for example in a wireless sensor network (WSN) composed by many nodes, can not be tolerated [2]. In order to improve or complement this system, many other positioning techniques have been the subject of the research activities and have drawn considerable attention. These systems can exploit the existing networks, for example the base stations (BSs) of a cellular network, or the access points (APs) of a WLAN indoor network, or can be implemented with ad-hoc networks. The basic principle of these solutions is to use two or more BSs (or APs) to intercept the signal from the mobile user (also called mobile station, MS). After that, common approaches can be used to determine a measurement of the MS position, such as trilateration (or multilateration), and triangulation [3]. These are based on the estimation of the following radio parameters: the received signal strength (RSS), the time of arrival (ToA), and the direction of arrival (DoA). The firsts two are used to obtain an estimate

Type of environment	Path loss exponent n_p
Free space	2
Urban area cellular radio	2.7 to 3.5
Shadowed urban cellular radio	3 to 5
In building LOS	1.6 to 1.8
Obstructed in building	4 to 6
Obstructed in factory	2 to 3

Table 1.1: Path loss exponent values for different environments.

of the distance (also called *ranging*) between the BS and the MS, while the latter provides angular information. All these techniques need to work in line-of-sight (LOS) conditions. Now, we describe them in detail.

1.1.1 Received Signal Strength

This technique is based on the fact that the energy of a signal changes with the distance. In this way, the RSS at a BS conveys information about how far the MS is. However, in order to convert the energy information into a distance, the relation between distance and energy attenuation, or path loss (PL), has to be known. A common model for the PL called log-normal shadowing PL model [4] is given by

$$PL(d) = PL(d_0) + 10n_p \log_{10}\left(\frac{d}{d_0}\right) + v, \tag{1.1}$$

where $PL(d)$ is the PL in dB at a distance d, $PL(d_0)$ is the PL in dB at a short reference distance $d_0 < d$ (d_0 is usually taken as 1 m), n_p is called *path loss exponent*, while v is a Gaussian random variable representing log-normal shadow fading effects in multipath (MP) environment. In radio propagation channel studies, the random variable v is considered zero mean, i.e., $v \sim \mathcal{N}(0, \sigma_v^2)$, while its standard deviation σ_v depends on the characteristics of a specific MP environment. This model can be used for both indoor and outdoor environments. The most common values of n_p are shown in Tab. 1.1 for different types of environment [5].

The Cramer-Rao bound (CRB), i.e., a lower bound for the root mean squared error (RMSE) of the distance d estimated with the RSS is reported in [6] and reads

$$\mathrm{RMSE}_{\mathrm{RSS}}(d) \geq \frac{\ln 10}{10}\frac{\sigma_v}{n_p}d. \tag{1.2}$$

Some CRB curves are plotted in Fig. 1.1 as function of σ_v with different system parameters.

This method is very simple. However, it requires an accurate knowledge of the path loss exponent n_p, and also its accuracy depends on the standard deviation of v. Further, at least

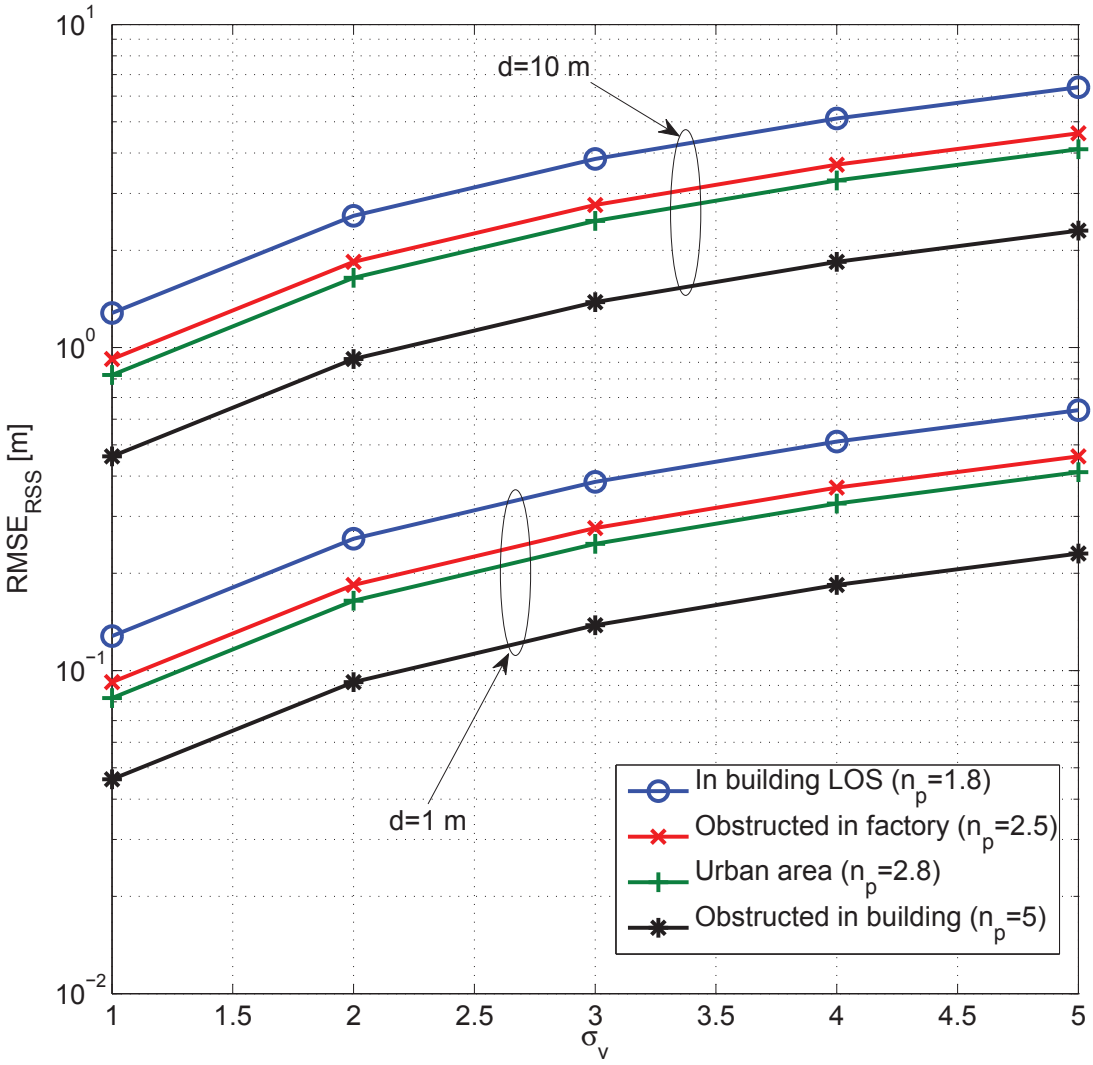

Figure 1.1: Cramer-Rao bound of the RSS technique as function of σ_v, path loss exponent n_p, and the distance d.

three BSs are required to perform the location estimation (in a 2-dimensional plane), i.e., the coordinates x, y of the MS.

1.1.2 Time of Arrival

The ToA of a signal traveling from one node to another, also called *time of flight* (ToF), can be used to estimate the distance between two nodes. If two nodes have a common clock, the node receiving the signal can determine the ToA of the incoming signal that is time-stamped by the reference node [6]. For a single path additive white Gaussian noise (AWGN) channel, it can be shown that the best achievable accuracy, expressed in term of root mean squared

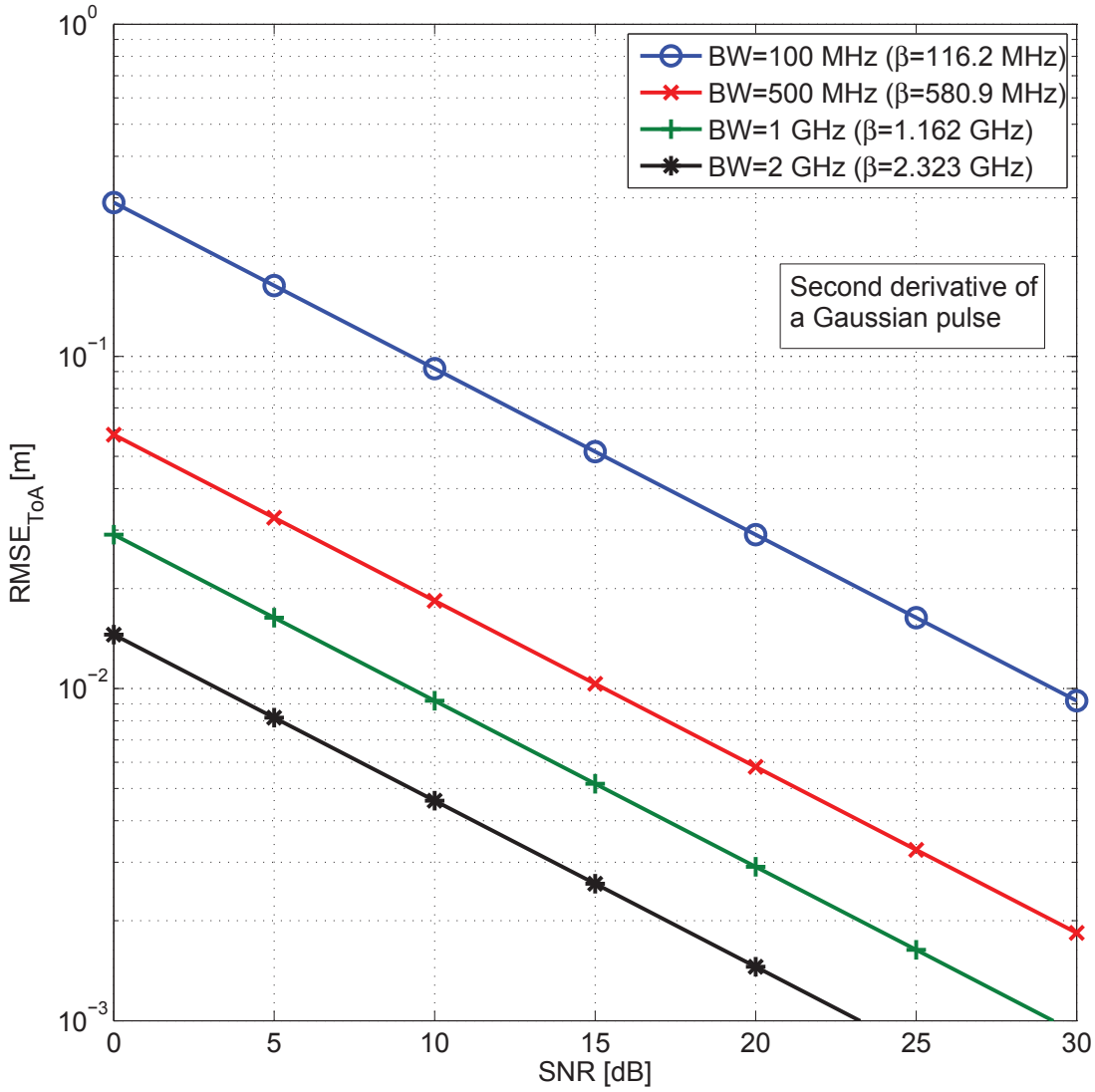

Figure 1.2: Cramer-Rao bound of the ToA technique as function of SNR and the signal bandwidth BW.

error (RMSE) of the distance d estimated from the ToA estimation, is lower bounded by [6]

$$\mathrm{RMSE}_{\mathrm{ToA}}(d) \geq \frac{c_0}{2\sqrt{2}\pi\sqrt{\mathrm{SNR}}\beta}, \tag{1.3}$$

where c_0 is the speed of light, SNR is the signal-to-noise ratio, and β is the *effective bandwidth* defined by

$$\beta = \sqrt{\frac{\int_{-\infty}^{\infty} f^2|S(f)|^2 df}{\int_{-\infty}^{\infty}|S(f)|^2 df}}, \tag{1.4}$$

with $S(f)$ the transmitted signal spectrum. Some CRB curves are plotted in Fig. 1.2. As it can be observed, the accuracy improves with the increase of the signal bandwidth. For this

reason, this technique is usually implemented with ultra wideband (UWB) systems [7].

Since the achievable accuracy under ideal condition is high, the clock synchronization between the two nodes becomes an important factor affecting the ToA estimation. It is worth noting that if there is no synchronization between the two nodes, but there is synchronization among reference nodes, then time difference of arrival (TDoA) technique can be employed [8].

This technique can be implemented in several ways. An optimal estimate can be obtained using a matched filter (or, equivalently, with a bank of correlators) [9]. Alternatively, an uncoherent energy detector receiver can be implemented [10, 11]. However, its performance strictly depends on the choice of a threshold [12, 13].

As for the RSS, ToA (and also TDoA) involves at least three BS nodes to perform the location estimation.

1.1.3 Direction of Arrival

The DoA estimation (also called angle of arrival (AoA) estimation) method usually involves multi-antenna BSs. It is attractive due to the fact that, differently to the other ranging techniques, does not need accurate synchronization among BSs and also it requires only two BSs to perform the location estimation. Now we present the basis of the DoA estimation problem.

Let us assume a single-input multiple-output (SIMO) system, where the MS is the transmitter node (a point source), while the BS is equipped with an M-element antenna array of known geometry. An example of this scenario is shown in Fig. 1.3, where a linearly equispaced (LES) antenna array geometry is represented. The source emits a radio frequency

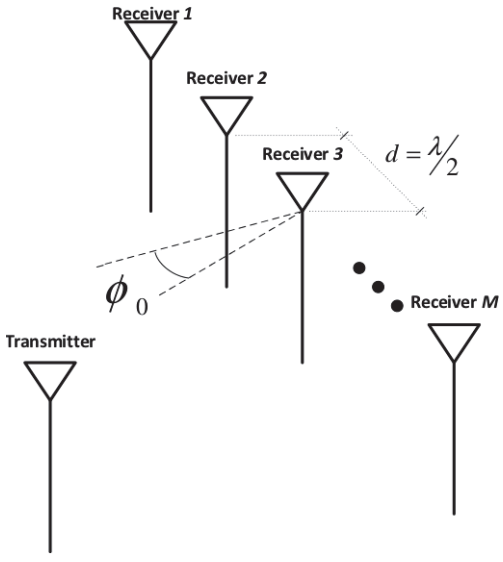

Figure 1.3: Single-input multiple-output scenario, with linearly equispaced antenna array with M elements spaced by $\lambda/2$.

(RF) signal $s_{RF}(t) = s(t)e^{j2\pi f_c t}$, where $s(t)$ is the transmitted baseband signal, and f_c is the

carrier frequency. Assuming a plane wave LOS propagation scenario, the incident signal at the i-th antenna element can be written as

$$x_{RF}^{(i)}(t) = \rho s(t-\tau_0)e^{j2\pi f_c(t-\tau_0-\Delta t^{(i)})} + w_{RF}^{(i)}(t), \tag{1.5}$$

where ρ is the channel attenuation (common to all elements under the hypothesis of closely spaced elements), τ_0 is the propagation delay between the MS and a BS reference point, e.g., the first antenna element, $w_{RF}^{(i)}(t)$ is the RF noise, while $\Delta t^{(i)}$ is the propagation delay between the BS reference point and the antenna i-th. Under the hypothesis of plane wave propagation, assuming that the antenna array geometry is LES, and taking the BS reference point as the first antenna element, the term $\Delta t^{(i)}$ can be expressed as

$$\Delta t^{(i)} = \frac{d}{c_0}\cos(\phi_0), \tag{1.6}$$

where d is the interelement distance, c_0 is the speed of light, while ϕ_0 is the DoA.

It is worth noting that we have implicitely assumed that the signal $s(t)$ is narrowband. In fact, the delay $\Delta t^{(i)}$ can be neglected in the signal $s(t-\tau_0)$ of (1.5) if $\frac{BW}{f_c} \ll \frac{1}{D}$, where BW is the signal bandwidth, while D is the array aperture in wavelength (in the case of a $\lambda/2$-spaced LES array, $D = \frac{M-1}{2}$). This condition is certainly fulfilled if the signal is narrowband.

After a downconversion stage, the baseband received signal can be written in matrix form as

$$\mathbf{x}(t) = \mathbf{a}(\phi_0)s(t-\tau_0) + \mathbf{w}(t), \tag{1.7}$$

where $\mathbf{x}(t)$ is the M-length column vector that contains the baseband received signal at the instant t, $\mathbf{w}(t)$ is the M-length vector of the complex baseband noise, while $\mathbf{a}(\phi_0)$ is called *array manifold* (or *steering vector*), and can be expressed as

$$\mathbf{a}(\phi_0) = [0, e^{-j\kappa d\cos(\phi_0)}, .., e^{-j\kappa d(M-1)\cos(\phi_0)}]^T \tag{1.8}$$

in the case of a LES array, with $\kappa = \frac{2\pi}{\lambda}$. It should be noted that we have neglected a common phase term, i.e., $e^{-j2\pi f_c\tau_0}$, that can be included into the signal $s(t-\tau_0)$.

In the case of N_t sources (a multiple-input multiple-output (MIMO) system), the system model in (1.7) becomes

$$\mathbf{x}(t) = \mathbf{A}(\phi)\mathbf{s}(t-\tau) + \mathbf{w}(t), \tag{1.9}$$

where $\mathbf{A}(\phi)$ is a $M \times N_t$ matrix whose columns are the steering vectors corresponding to the N_t-length DoA vector $\phi = [\phi_0, \phi_1, .., \phi_{N_t-1}]^T$, and $\mathbf{s}(t-\tau) = [s_0(t-\tau_0), s_1(t-\tau_1), .., s_{N_t-1}(t-\tau_{N_t-1})]^T$ is the N_t-length column vector whose entries are the N_t transmitted signals, each one with its own delay $\tau_m,\ m \in \{0, .., N_t-1\}$.

Therefore, the DoA estimation problem consists in the estimation of the parameter ϕ_0 (or

ϕ) from the signal in (1.7) (or in (1.9)). Many solutions to this problem have been presented over the last four decades. To this end, good overviews on the DoA estimation algorithms can be found in [14, 15]. Among the most cited, we can found the so-called super resolution or subspace-based method, such as *multiple signal classification* (MUSIC) [16], *estimation of signal parameters via rotational invariance* (ESPRIT) [17], and their variants [18,19]. These methods, although sub-optimal, provide very good performance, and are usually considered as the reference algorithms in this context.

For the sake of completeness, we report the CRB for a single source DoA estimation, as shown in [20], i.e.,

$$\mathrm{RMSE}_{\mathrm{DoA}}(\phi_0) \geq \frac{1}{\kappa d \cos(\phi_0)} \sqrt{\frac{6}{\mathrm{SNR} \cdot M(M^2-1)}}, \tag{1.10}$$

and some CRB curves in Fig. 1.4.

1.2 Thesis Objectives and Outline

As shown in the previous section, the DoA estimation problem is based on the knowledge of the array manifold shape, i.e., it is assumed that the model in (1.7) does not deviate significantly from the reality. Unfortunately, the ideal behaviour described by (1.7) is not fully realistic because of the presence of non idealities, among which:

- mutual coupling among antenna elements,
- manufacturing imperfections,
- impairments due to the analog front-ends,
- multipath signal.

Although the first two items are well investigated in the literature, to the best of our knowledge, analog front-end impairments (that in this work we call *hardware impairments*) are usually not considered. From this, the first objective of this thesis is to investigate the effects of hardware impairments in the DoA estimation.

For what the MP propagation is concerned, the first proposed solutions were based on the super resolution algorithms. However, although these methods present higher resolution capabilities, they suffer some drawbacks. Firstly, they can not resolve coherent waves directly, and this is a great limitation in the case of MP channels since the multipath components (MPCs) are coherent with the direct path. To overcome this difficulty, a preprocessing technique, called Spatial Smothing Pre-processing (SSP), and other variants have been proposed [21], [22]. Another problem of the super resolution algorithms is that the total number of signals impinging on the array must be less than the number of sensors. Moreover, the

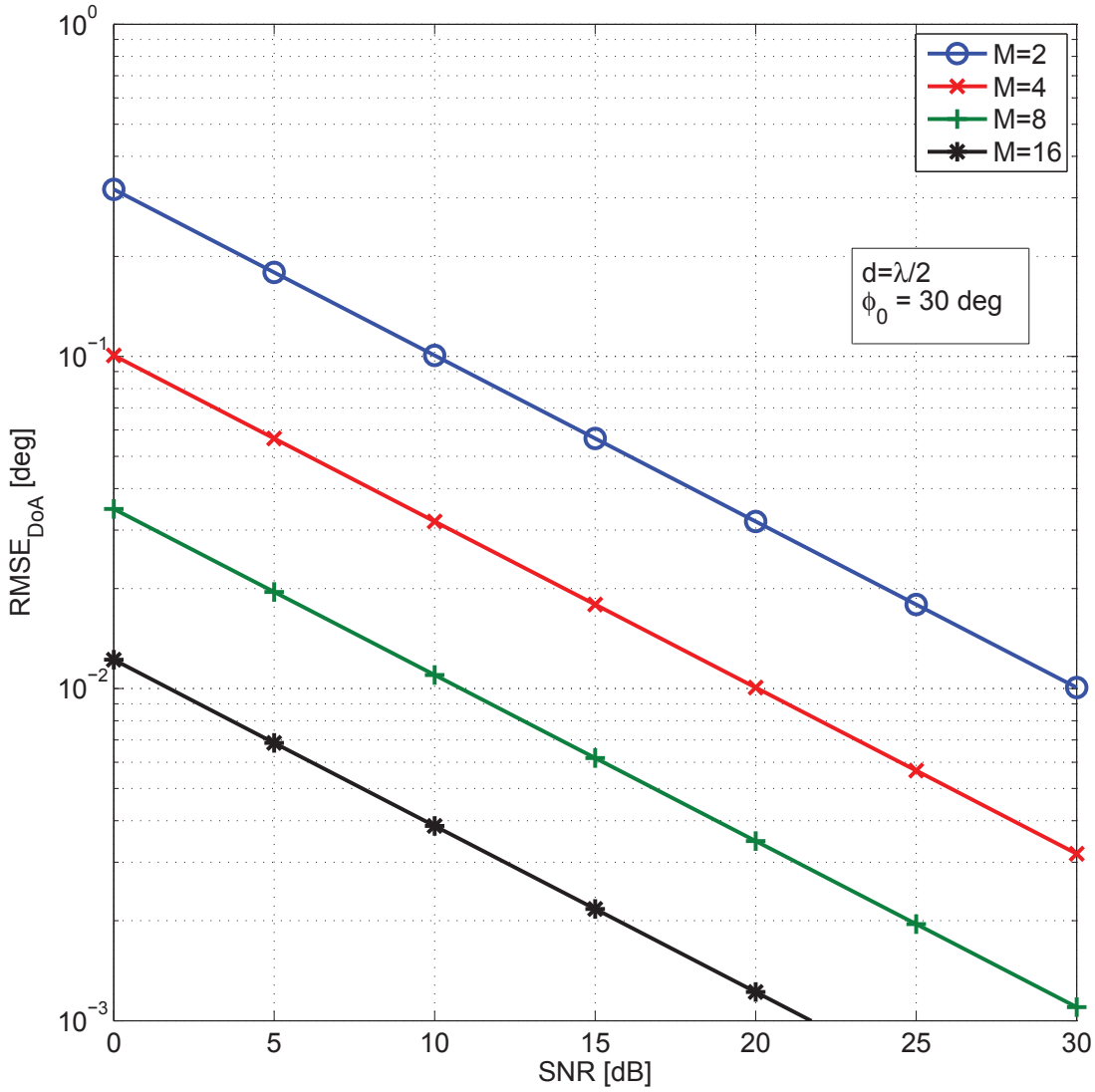

Figure 1.4: Cramer-Rao bound of the DoA technique as function of SNR and the number of antenna element M.

SSP decreases the effective array size, and this further limits the total number of signals that can be distinguished. In this respect, the Joint Angle and Delay Estimation (JADE) algorithm has been presented in [23]. This solution, that aims at the estimation of DoAs and delays of the MPCs using a collection of space-time channel estimates, can work in cases where the total number of impinging signals exceeds the number of antennas. However, like the traditional MUSIC and ESPRIT, it need to compute an eigendecomposition that is computationally costly. Other algorithms that do not rely on the eigendecomposition have been proposed to deal with the MP propagation, but they need a great computational effort [24], [25], [26].

Motivated by all these considerations, we found another objective of this thesis, i.e., to propose a novel DoA estimation algorithm that deals with MP propagation and that is not constrained by the number of MPCs or by the number of antenna elements.

An outline of the thesis follows.

1.2.1 DoA Estimation with Hardware Impairments

In order to properly investigate the effect of hardware impairments in the DoA estimation, it is important to characterize these non idealities to provide a system model that includes them. In Chapter 2, we describe a generic multiple antenna receiver architecture based on the integration of independent single receivers. We analyze in details this configuration with an experimental measurement campaign, in order to model the most detrimental hardware impairments. In Chapter 3, we present a low complexity DoA estimator for single source signal (for 2-D and 3-D cases), and we show its robustness to the considered non idealities. Chapter 4 describes a wireless testbed, called *WiPLi Lab Testbed*, that can be used to the validation of multiple antenna receiver algorithms, and also to test the performance of DoA estimation algorithms. We show several practical results of the proposed DoA estimator, obtained in an anechoic chamber.

In Chapter 5, we consider the problem of the array calibration. In fact, the algorithm presented in Chapter 3 compensates the phase offsets among the antenna elements estimating them from a known direction signal. However, this technique is not always practical. Herein, we present a novel array calibration solution, also performing an accurate performance analysis.

Finally, Chapter 6 presents an extensive comparison among multiple antenna receiver architectures. We show that each specific architecture has its own non idealities that have to be considered.

1.2.2 DoA Estimation in MP Channels

The second part of the thesis deals with MP propagation in the context of DoA estimation. More precisely, in Chapter 7 we describe a novel concept of DoA estimation in such a scenario, based on a first arrival path (FAP) identification. This method includes the following steps: a) a coarse synchronization that identifies the start of the transmitted frame; b) a channel estimation; c) a threshold based fine synchronization that accurately selects the FAP; d) a low complexity single source DoA estimation. In particular, the DoA estimator is the method described in Chapter 3. We analyze the performance of this techniques as a function of the channel parameters, showing several simulation results. Furthermore, we consider the case of overlapping LOS and NLOS paths, and, when the NLOS power is high, we propose to use our procedure with smooth-MUSIC [21], a well-known spatial smoothing pre-processing method.

1.3 Related Publications

The main results of this work have been the subject of the publications listed in the following.

Journal Papers

[J-1] D. Inserra, A. M. Tonello, "Multiple Antenna Receiver Architectures for Direction of Arrival Estimation", *to be submitted to IEEE Communications Magazine*, 2012.

[J-2] D. Inserra, A. M. Tonello, "A Wireless Testbed for the Validation of Multiple Antenna Receiver Algorithms", *submitted to Elsevier Computer and Electrical Engineering*, 2012.

[J-3] D. Inserra, A. M. Tonello, "A Frequency Domain Angle of Arrival Estimation Approach in Multipath Channels", *submitted to IEEE Transactions on Vehicular Technology*, 2012.

[J-4] D. Inserra, A. M. Tonello, "Performance analysis of a novel antenna array calibration approach for direction finding systems", *European Telecommunication Technologies*, Wiley, DOI 10.1002/ett.2576, 2012.

[J-5] D. Inserra, A. M. Tonello, "Characterization of Hardware Impairments in Multiple Antenna Systems for DoA Estimation", *Journal of Electrical and Computer Engineering*, Hindawi, vol. 2011, article ID 908234, 10 pages, DOI: 10.1155/2011/908234, 2011.

Conference Papers

[C-1] A. M. Tonello, D. Inserra, "Positioning Based on DoA Estimation: an Implementation Perspective" (invited paper), *submitted to IEEE International Conference on Communications, Workshop on Advances in Network Localization and Navigation*, Budapest, Hungary, 9-13 June 2013.

[C-2] D. Inserra, A. M. Tonello, "Training Symbol Exploitation in CP-OFDM System for DoA Estimation in Multipath Channels", *submitted to IEEE International Conference on Communications*, Budapest, Hungary, 9-13 June 2013.

[C-3] D. Inserra, A. M. Tonello, N. Moret "Positioning Based on 2-D Angle of Arrival Estimation", *proc. of IEEE 73rd Vehicular Technology Conference*, Budapest, Hungary, 15-18 May 2011.

[C-4] D. Inserra, A. M. Tonello, "DoA Estimation with Compensation of Hardware Impairments", *proc. of IEEE 72nd Vehicular Technology Conference*, Ottawa, Canada, 6-9 Sep. 2010.

Chapter 2

Characterization and Modeling of Hardware Impairments

As explained in Chapter 1, the direction of arrival (DoA) estimation can be impaired by the hardware non idealities. These non idealities depend on the receiver architecture, on the manufacturing accuracy, and on the quality of the used components. As a starting point, we have considered a state-of-the-art multiple antenna receiver for multiple-input multiple-output (MIMO) applications. We have characterized it with a measurement campaign that has revealed the presence of different carrier frequency offsets (CFOs), phase offsets (POs), and phase noises (PNs) among the receivers, and DC offsets. The results of the measurement campaign have been used to obtain a more general model for the hardware impairments that can be used to describe similar multiple antenna receiver architectures.

2.1 Introduction

In Chapter 1, we have presented the basis of the DoA estimation problem. However, the theoretical estimation accuracy can be strongly affected by the fact that the hardware does not behave as it is expected. Particularly, when the background noise is low, there are present second order effects that are not more negligible. This problem does not always arise from a practical engineering inability, but mainly from consideration of applicable economic constraints as well as management of issues such as size, weight, etc.

In this chapter we focus our analysis on a hardware support based on independent direct-conversion front-ends (FEs), an architecture which we will refer to as *full-parallel uncoherent* (FP) in the following. We firstly describe the features of this system, based on a Lyrtech platform. Then, we report the measurement campaign results and we describe the hardware impairment models.

2.2 Hardware Platform Description

The hardware support we consider herein is based on a Lyrtech platform [27]. It is composed by two main parts: an acquisition board, the Lyrtech VHS-ADC, and a quad dual-band radio frequency (RF) transceiver.

2.2.1 Lyrtech VHS-ADC

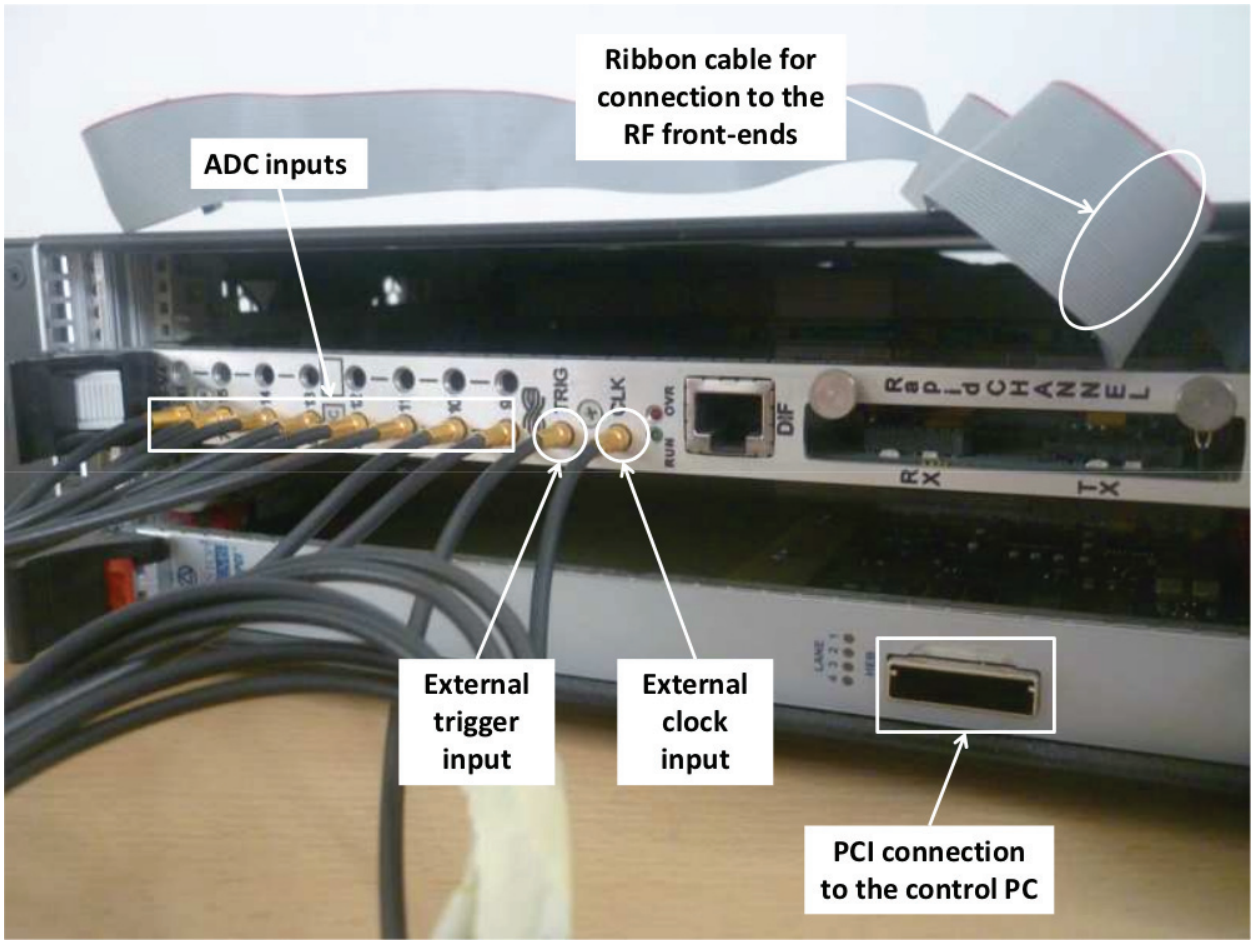

Figure 2.1: Lyrtech VHS-ADC acquisition board.

The acquisition board (Fig. 2.1) comprises eight channels, and it is equipped with a Xilinx Virtex-4 XC4VLX160 field-programmable gate array (FPGA) and two synchronous dynamic random access memory (SDRAM) banks each with 64 MB of memory. Their analog to digital converters (ADCs), AD6645 from Analog Devices [28], have 14-bit of resolution with sampling rate up to 104 MHz, 2.2 V_{pp} (peak-to-peak voltage) of dynamic, and they can be controlled by using an external clock and/or an external trigger. This allows the processing of four in-phase and in-quadrature (I&Q channels). Finally, a dedicated compact peripheral component interface (cPCI) bus is used to connect the board to a PC. A complete block scheme of the acquisition board is depicted in Fig. 2.2. As it can be observed, in Fig.

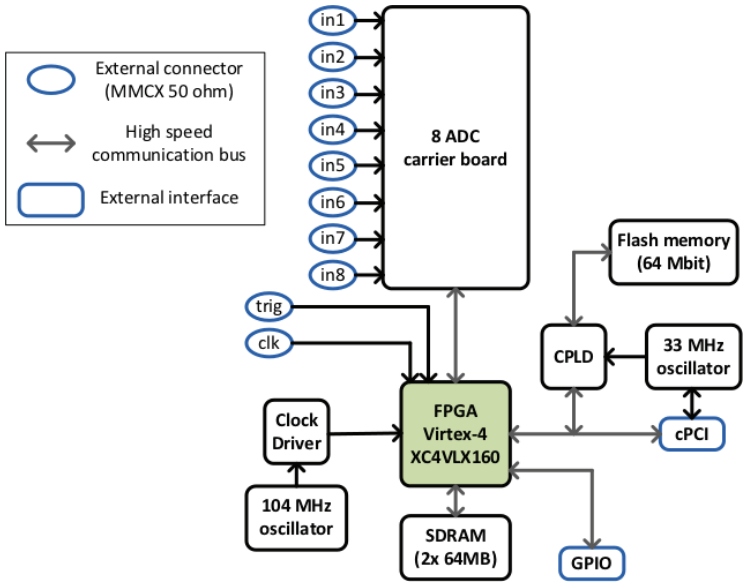

Figure 2.2: Block scheme of the Lyrtech VHS-ADC acquisition board.

2.2 are also highlighted a complex programmable logic device (CPLD) and a 33 MHz clock useful to program the FPGA, a 64 Mbit flash memory to store the bitstream, and a general purpose input/output (GPIO) connection bus to interface the FPGA to the quad dual-band RF transceiver described below. The external connectors, as it can be observed from Fig. 2.1, are 50 Ω micro-miniature coaxial (MMCX).

2.2.2 Quad dual-band RF transceiver

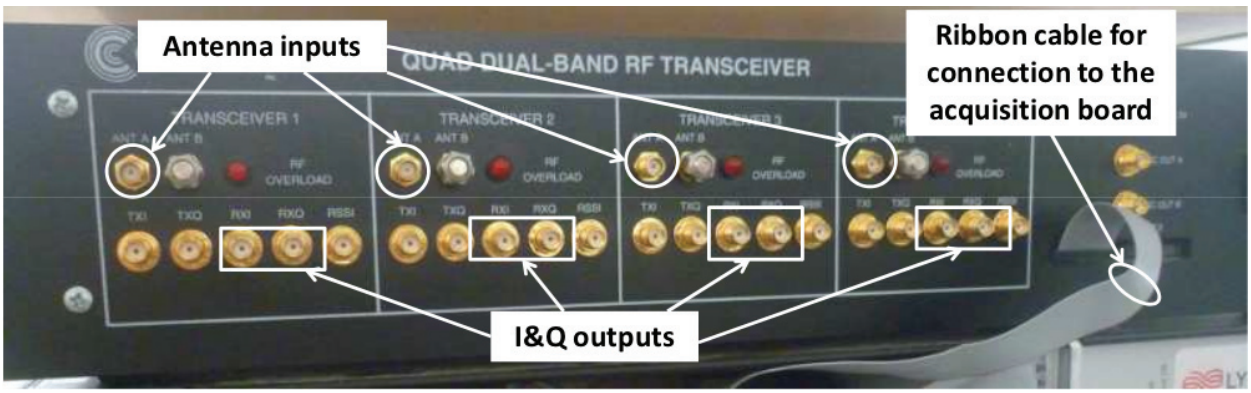

Figure 2.3: Quad dual-band RF transceiver.

In Fig. 2.3, the quad dual-band RF transceiver is shown. It deploys four independent RF direct conversion receivers [29] based on the integrated circuit (IC) MAX2829 [30] (that can operate either in the frequency ranges $2.4 - 2.5$ GHz or $4.9 - 5.875$ GHz). A block scheme of one transceiver of the quad RF FE is shown in Fig. 2.4. As it can be observed, a single-pole double-through (SPDT) switch (called *diversity switch*) can be used to select one of the two antennas that has to be connected to the analog FE ("ant A" and "ant B" in Fig.

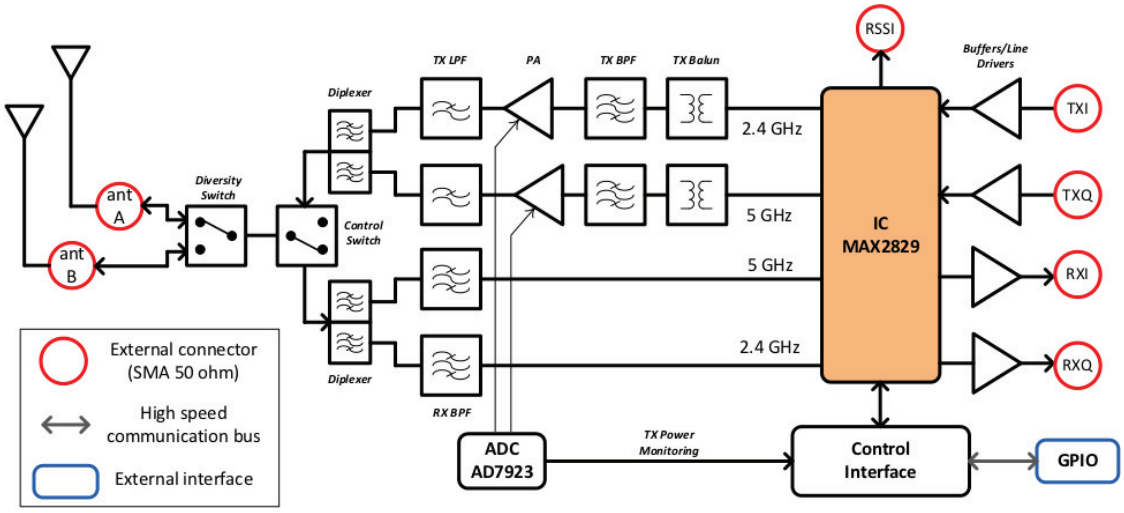

Figure 2.4: Block scheme of one transceiver of the quad RF front-end.

2.4). Another switch (called *control switch*), instead, allows the selection of the transceiver mode, i.e., transmission or reception. In this work, this system will be used only in the reception mode. The IC MAX2829 also gives an RSS measurement, the received signal strength indicator (RSSI), that can be acquired and processed to implement the ranging as described in Chapter 1. All the external connections are 50 Ω subminiature version A (SMA).

The IC is controlled via a GPIO bus by the FPGA of the Lyrtech board. Through this bus, the 13 registers that manage the FE parameters can be modified. More precisely, it is possible to:

- enable one or more transceiver,
- select the mode of each transceiver (transmission or reception),
- select the diversity switch position,
- select the local oscillator (LO) source (internal or external),
- modify the transceiver gain,
- select the channel frequency,
- select the bandwidth,
- enable a high-pass filter.

In Fig. 2.5, we depict the main blocks of the receiver architecture, i.e., direct conversion receiver, for an antenna path. As we can observe, the signal captured by the antenna is filtered with a band select filter (BSF), amplified with a low noise amplifier (LNA) and down-converted by two mixers fed by two 90°-delayed carriers. The down-converted signals

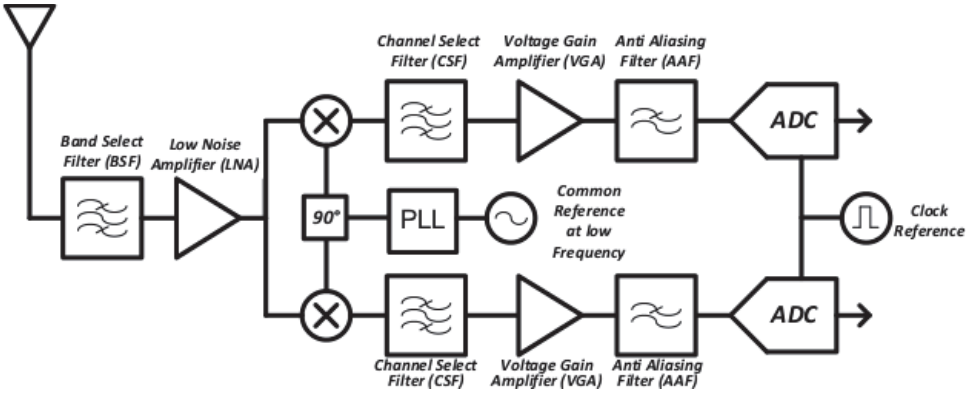

Figure 2.5: Direct conversion receiver architecture for each channel (antenna).

are filtered with a channel select filter (CSF) that attenuates the interferers and DC offset. Finally, we have a voltage gain amplifier (VGA) and an anti-aliasing filter (AAF) that renders the signals suitable for the acquisition through the ADCs. The carrier frequency is generated by a phase-locked loop (PLL) from a low frequency reference oscillator shared by all the receivers.

The direct-conversion architecture is attractive due to its simplicity and the reduced costs, but it is well known that it has some drawbacks, among which the presence of DC offsets and the I&Q mismatch [31]. Furthermore, the FP multiple antenna receiver architecture have independent and not co-phased LO signals generated by different PLL circuits; this introduces other non-idealities that can affect the DoA estimation (as we will see in the following), such as CFOs and phase offsets POs among the receivers, and also different PNs.

In the following sections, we report the results of the measurements from which we derive and propose a model for the major impairments. The model allows the derivation of digital compensation algorithms and performance analysis.

2.3 Measurement Results

In this section, we firstly show some measurement results of the main parameters of the receiver, such as gain and bandwidth. After that, we describe the measurement results of DC offset, CFO, and PN.

2.3.1 Main Parameters

Each block shown in Fig. 2.5 may influence the total receiver gain and the bandwidth. We have observed that gain and bandwidth are dominated by the analog FE, while the ADC contribution is negligible. Therefore, we report only the measurement results obtained from the RF part. The measurement setup for both gain and bandwidth can be found in Appendix 9.1.

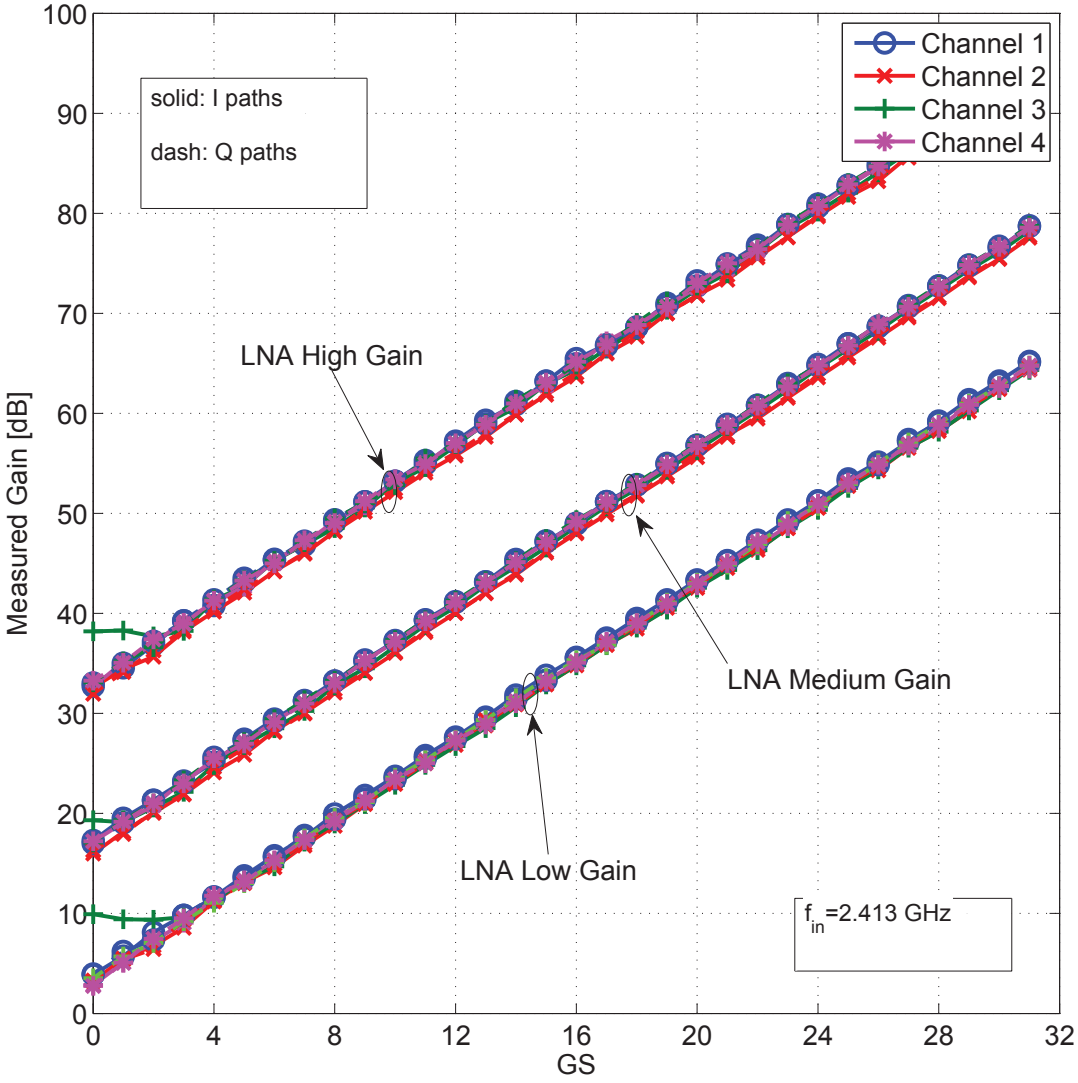

Figure 2.6: Front-end gain measurements as function of the gain setting and the LNA gain mode, measured with a single tone signal at 2.413 GHz.

Gain

In the datasheet of the IC MAX2829 [30] three LNA gain mode can be selected: low, medium, and high. Furthermore, the gain setting (GS) parameter controls the VGA amplification, with a step of 2 dB. In Fig. 2.6 we show the FE gain measurements as function of GS and the LNA gain mode.

It should be noted that the gain curves of the different channels practically overlap, as the gains of the I&Q paths for each channel, except for the channel 3 with low GS (this anomalous behaviour is due to high noise during the measurement process). With respect to the I&Q gain imbalance, we have found a maximum value of 0.5 dB. In Tab. 2.1 we report

LNA gain mode	Measured gain [dB]
low	3
medium	17
high	33

Table 2.1: Measured gain values with different LNA gain modes, when the gain setting is set to 0.

the measured gains with the different LNA gain mode, when GS is 0. From Fig. 2.6 we can also observe that each unitary GS step corresponds to a 2 dB of gain, as also reported in [30].

Bandwidth

In Fig. 2.7, we report the frequency response for the I path of the first channel, as function of the bandwidth setting [1]. There are two parameters to set the bandwidth: a coarse parameter, BW $\in \{7.5, 9.5, 14, 18\}$ MHz, and a fine adjustement that allows to increase or decrease the bandwidth from the 110% to the 90% of the BW value. We have observed good correspondence with the coarse bandwidth setting BW and the measured results. In the figure, we have also reported the frequency response of the FE when the bandwidth is set at the 90% and at the 110% (dash and dash-dot curves, respectively). Even in these cases we have found good agreement between the datasheet results [30] and the experimental ones.

2.3.2 Impairments

Now, we present the measurement results of the main hardware impairments, i.e., the background noise and the DC offset, CPOs, CFOs and PNs. We also show the characterization of the ADC non linearity, although it won't be considered in the rest of this work.

Noise and DC Offset

The background noise is due to both the RF and the acquisition parts. For what the RF FE is concerned, *noise figure* (NF) is the figure of merit usually considered to describe the amount of noise that the device adds to the useful signal [29]. This parameter is defined as the ratio between the signal to noise ratio (SNR) at the output of the device (in this case the analog FE) and the SNR at its input. In Fig. 2.8, we report the measurement results of the NF for each receiver channel as function of the gain parameters (LNA gain mode and GS). These results have been obtained using the measurement setup described in Appendix 9.2. We have verified that these values agree with the ones reported in [30].

As explained before, there is also a noise contribution due to the acquisition part. There exists a formula that can be used to compute the noise figure of a cascade of devices (the

[1] we have observed a similar behaviour for the Q path of the first channel, as well as for the I&Q paths of the other FEs

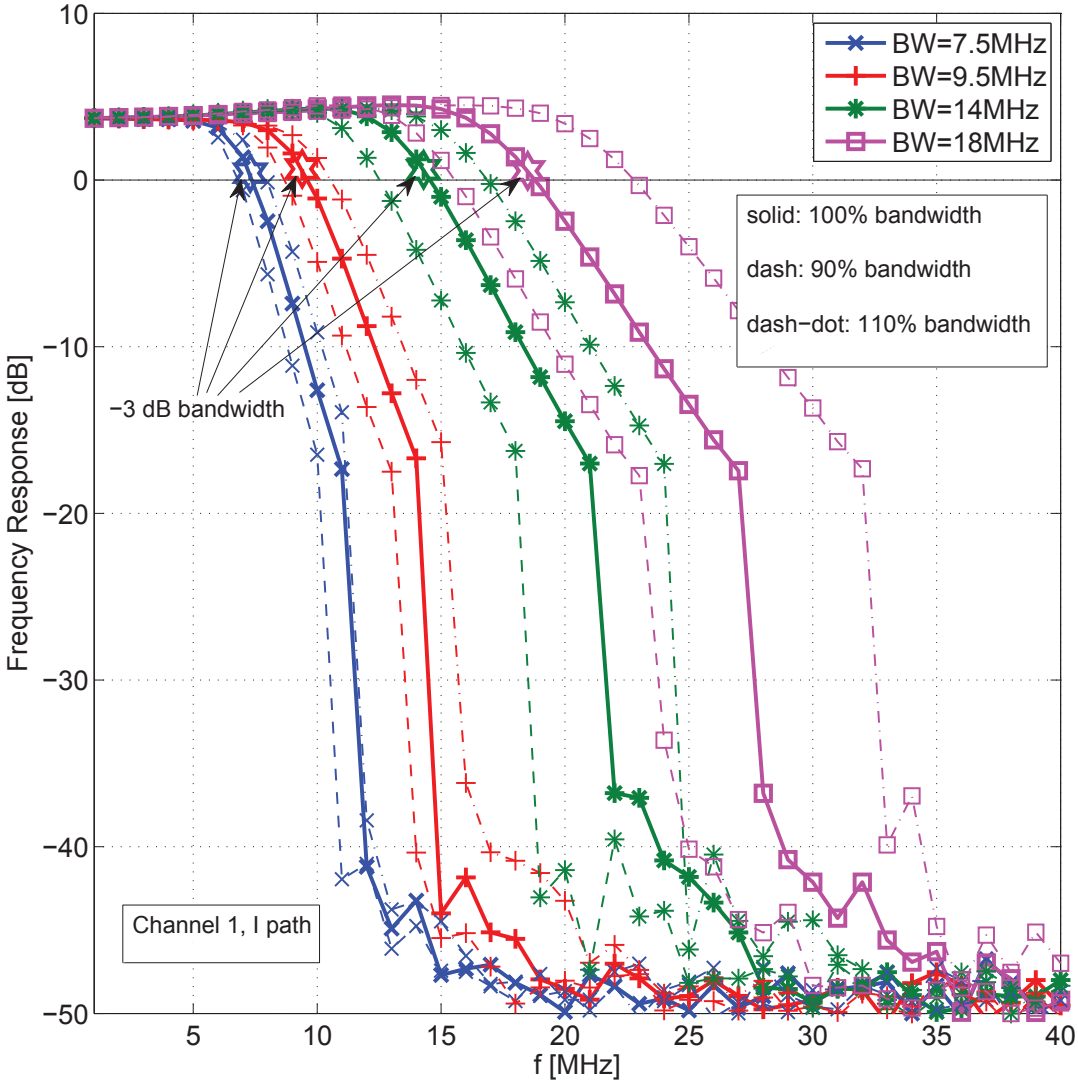

Figure 2.7: Frequency response measurement for the in-phase path of the first channel as function of the bandwidth setting, with low gain mode.

so called Friis formula [29]) that can be used to evaluate the total amount of noise after the ADC. However, although a noise figure could be assigned to the ADC, it is often easier to work with the ADC differently, since it is a "voltage" device. Nevertheless, in order to convert the noise power at the output of the analog FE into a noise voltage, it is necessary to circuitally know how the FE is connected to the ADC input. Unfortunately, this information is not available, and we cannot compute this conversion analytically. Alternatively, it is possible to directly measure the noise that includes both the RF part and the ADC. In Fig. 2.9, we have reported the root mean squared (RMS) noise voltage (in dBV) measured from the samples at the output of the ADCs, with BW = 7.5 MHz, as function of the gain parameters. From the noise measurements (obtained with the measurement setup reported in

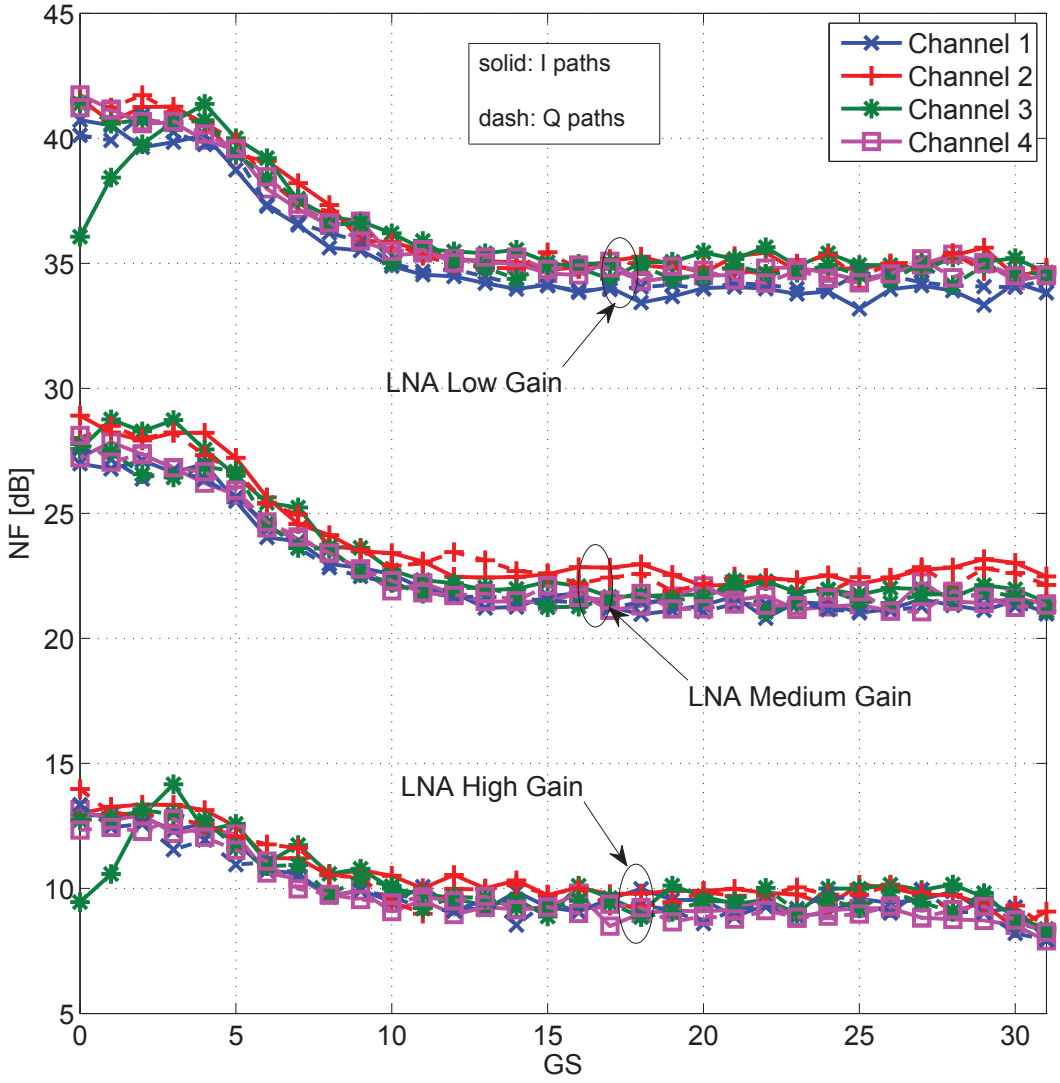

Figure 2.8: Noise figure measurements as function of the gain parameters.

Appendix 9.3), we can compute the maximum achievable SNR, i.e., the SNR that is obtained when each component (I&Q) of the useful signal completely spans the ADC dynamic, i.e., $x_{pp,max} = 2.2\ V_{pp}$, given by

$$\mathrm{SNR}_{max} = \frac{x_{pp,max}^2}{2 \cdot \mathrm{PAPR} \cdot M_w}, \tag{2.1}$$

where $M_w = E\{|w(nT)|^2\}$ is the measured noise power ($E\{.\}$ is the expectation operator), while

$$\mathrm{PAPR} = \frac{\max |x(nT)|^2}{M_x} \tag{2.2}$$

is the *peak-to-average power ratio* [32], a parameter that relates the signal power $M_x = E\{|x(nT)|^2\}$ to the maximum signal dynamic that, for a zero mean signal yields $\max |x(nT)|^2 =$

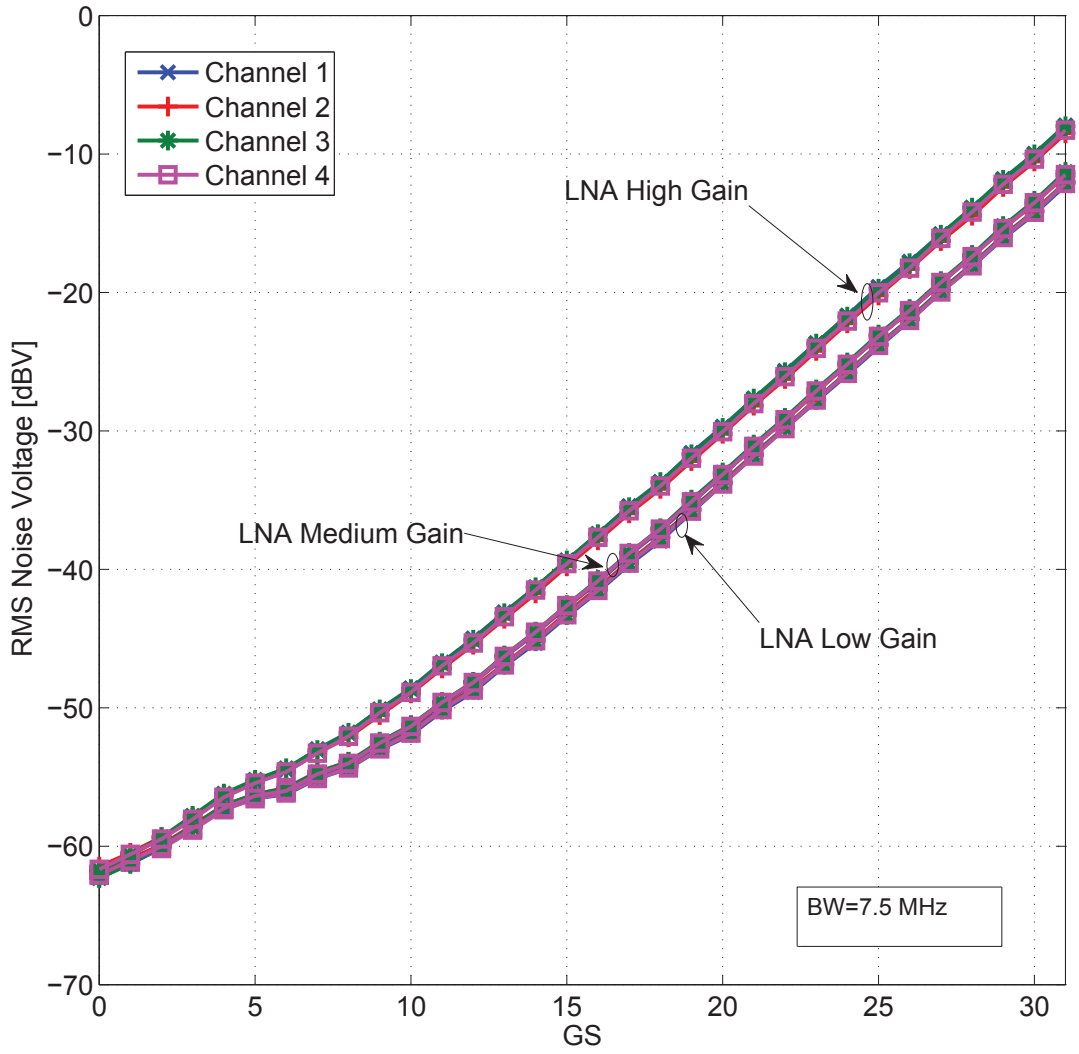

Figure 2.9: Noise voltage as function of the gain parameters.

$\frac{x_{pp}^2}{2}$. The maximum achievable SNR is shown in Fig. 2.10 for the first channel and BW= 7.5 MHz. We have reported three cases: a complex sinusoidal signal (PAPR= 3 dB), a single carrier 64 quadrature amplitude modulation (QAM) signal (PAPR= 3.7 dB), and an orthogonal frequency division multiplexing (OFDM) signal (PAPR≈ 12 dB). As it can be observed, the maximum achievable SNR decreases with the increase of GS due to the increase of the noise power. Thus, if the received power was too low, it would be necessary to amplify the received signal, i.e., to increase the gain, in order to reach the ADC dynamic range, with the consequence of a reduction of the maximum achievable SNR. However, opportunely setting the transmitted power, we can obtain SNR values up to approximately 60 dB.

The noise measurement activity has revealed the presence of a DC component (which we refer to as DC offset in the following). Both the analog FE and the acquisition board

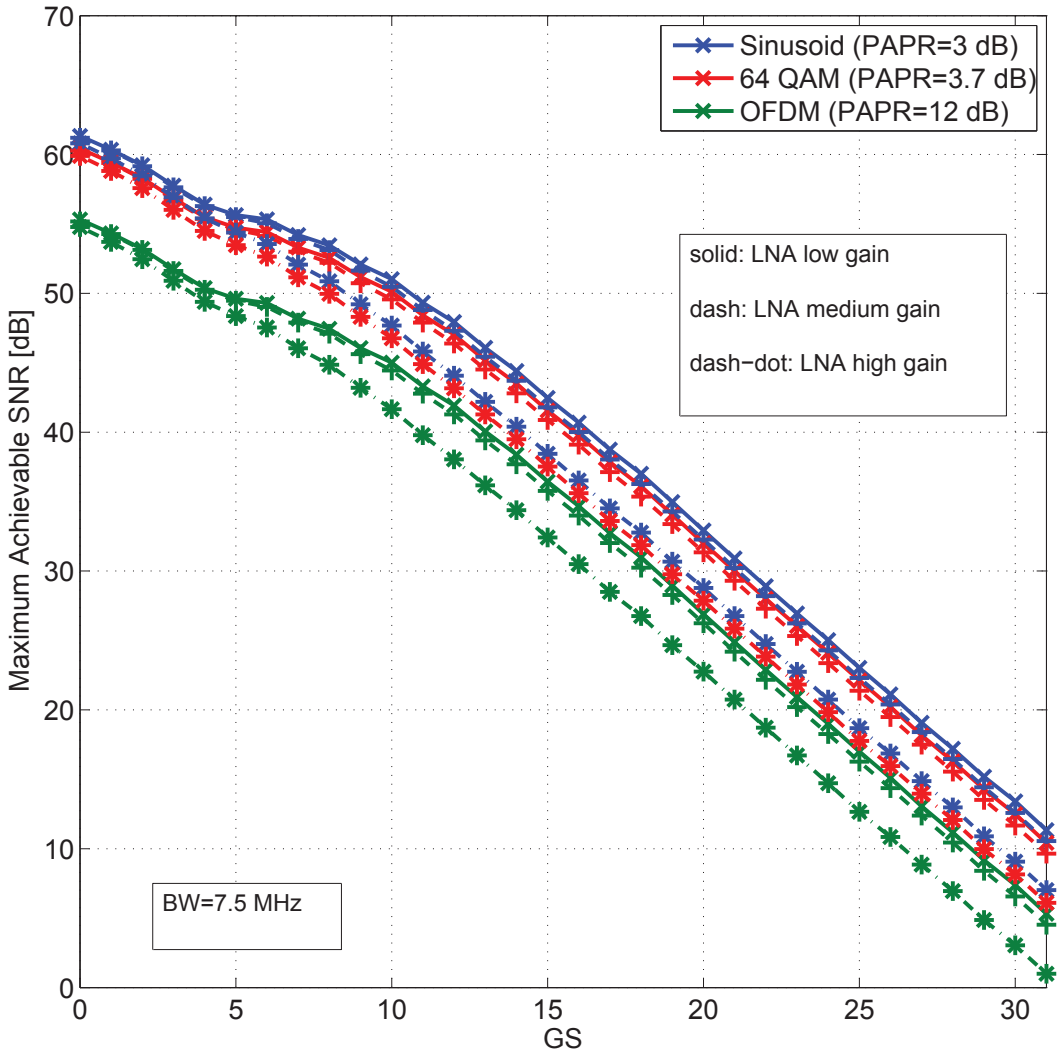

Figure 2.10: Maximum achievable SNR as function of the gain setting, with BW= 7.5 MHz.

imperfections contribute to the DC offset. This is due to static effects, e.g., signal leaking and self-mixing of the RF stage, transistor mismatches and other circuit imperfections, and dynamic effects, e.g., overload due to fading effects that cannot be compensated immediately by the automatic gain control (AGC) channel [31, 33].

In order to characterize the static DC offset we have performed several acquisitions for all eight digital channels of the hardware platform. We have found that in our specific case the DC offset is practically constant although it is different among the channels. As an example, the measured DC offsets for the eight channels when we inject a 50 mV sinusoidal tone are equal to -6.0 mV, -22.5 mV, -10.8 mV, -24.9 mV, 2.5 mV, -13.2 mV, 4.0 mV, and -16.3 mV.

While the static DC offset is independent of the input signal frequency, it depends on the

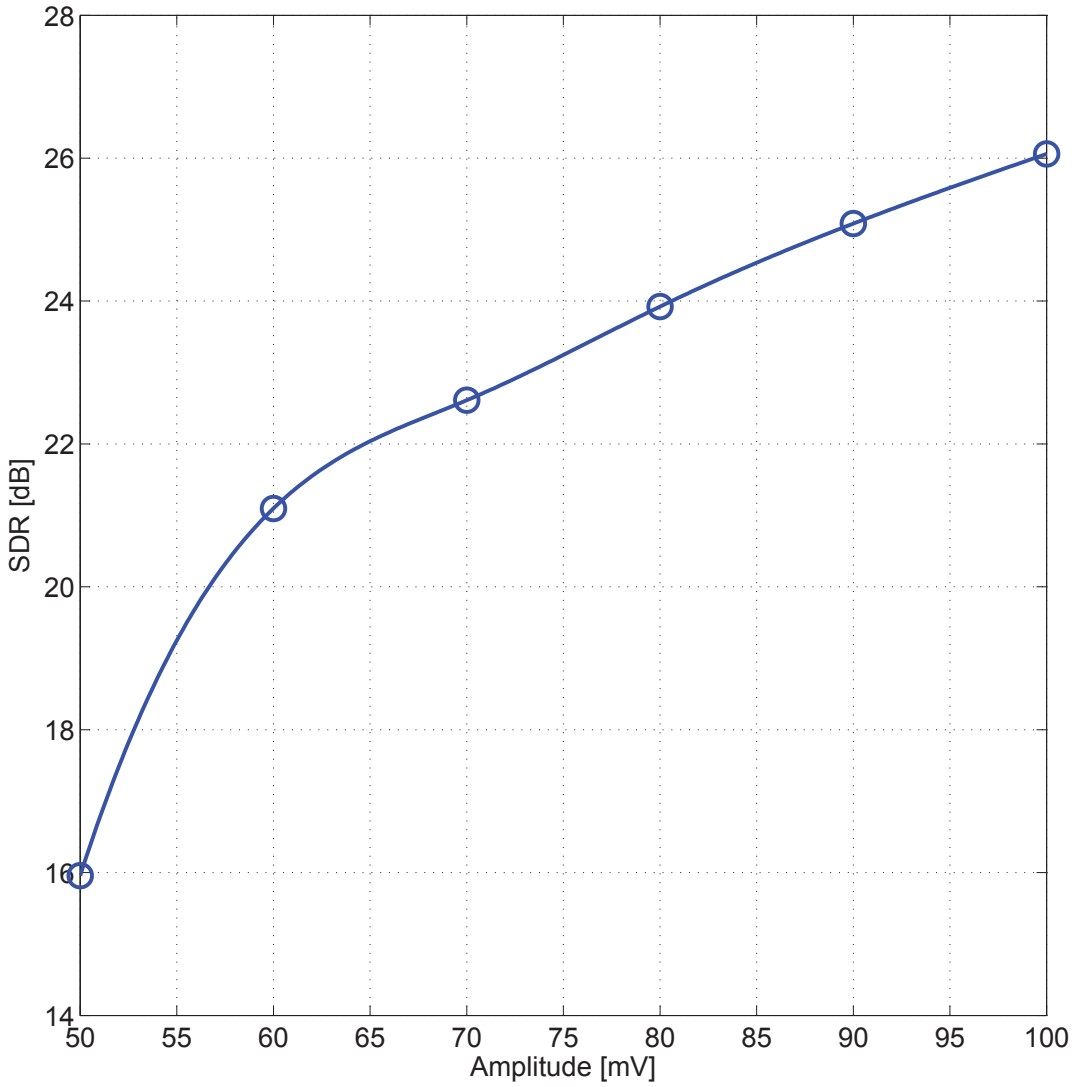

Figure 2.11: SDR as a function of the signal amplitude.

level of the input signal. This relation has been obtained via measurements (see Appendix 9.4) for the first channel and it is reported in Fig. 2.11 in terms of the ratio between the signal power S^2 at the output of the RF FE, and the DC offset power N_1,

$$\text{SDR} = \frac{S^2}{N_1}. \tag{2.3}$$

The figure shows that the considered platform exhibits an SDR ranging from 16 dB to 26 dB with input signal amplitudes from 50 mV to 100 mV.

Phase Noise, Carrier Frequency and Phase Offsets

The characterization of the PN as well as the CFOs and POs has been experimentally done by feeding each RF receiver with a single tone signal at the nominal carrier frequency. Then, the normalized received baseband output signal for the i-th channel sampled at rate $1/T$ can be written as

$$x^{(i)}(nT) = Se^{j(2\pi f^{(i)}nT+\varphi^{(i)}(nT)+\Phi^{(i)})} + w^{(i)}(nT) \tag{2.4}$$

where S is the signal amplitude, $f^{(i)}$ represents the CFO between the transmitted signal carrier and the carrier of the i-th receiver, while $\Phi^{(i)}$ is a constant PO. It should be noted that also PN can be present. It is herein denoted with $\varphi^{(i)}(nT)$ and it represents a time variant random component of the phase. Finally, $w^{(i)}(nT)$ is the background noise.

We have computed the argument of the acquired samples, and we have separated the three phase contributes. In particular, we have firstly estimated the CFO for each receiver, obtaining the following values: $f^{(1)} = 15.63$ kHz, $f^{(2)} = 15.44$ kHz, $f^{(3)} = 15.45$ kHz, $f^{(4)} = 15.46$ kHz. After that, we have identified a time variant contribution, the PN, $\varphi^{(i)}$, and a constant term, the PO $\Phi^{(i)}$. We have observed that the PO is different among the receivers, since the LO signal is generated separately by each IC. Moreover, as the DC offset, it changes every time the FE is powered up. It is worth noting that the signal amplitude S has been chosen such that the background noise $w^{(i)}(nT)$ does not influence significantly the estimation of the parameters described above.

In Fig. 2.12, we report the power spectrum, in dBc/Hz, of the PN $\varphi^{(i)}(nT)$ computed from the acquired samples of a given channel using the periodogram. For comparison, we also report the result of the measurement performed with a spectrum analyzer of the baseband signal at the output of the RF down-converter. As the figure shows, there is good consistency between the two power spectra. The measurement setup is described in Appendix 9.5.

We have found that the PN process is slowly time variant. In fact, as shown in Fig. 2.13, the correlation is larger than 0.55 after 25 samples (corresponding to 0.5 μs with sampling period $T = 20$ ns).

ADC Non Linearity

We have characterized the dynamic behaviour of the ADCs in terms of several specifications, such as total harmonic distortion (THD), spurious free dynamic range (SFDR), signal to noise ratio (SNR), signal to noise and distortion ratio (SINAD), and effective number of bits (ENOB). The measurement setup is reported in Appendix 9.6.

These parameters can be measured with a fast Fourier transform (FFT) analysis. In Fig. 2.14, we have shown the FFT samples calculated on a single tone signal at frequency $f_{in} = 1.26955$ MHz acquired by the first ADC of our baseband board (similar results have been found for the other ADCs). This frequency guarantees the minimum level of spectral leakage, i.e., if N is the number of acquired samples and F_s is the sampling frequency, then

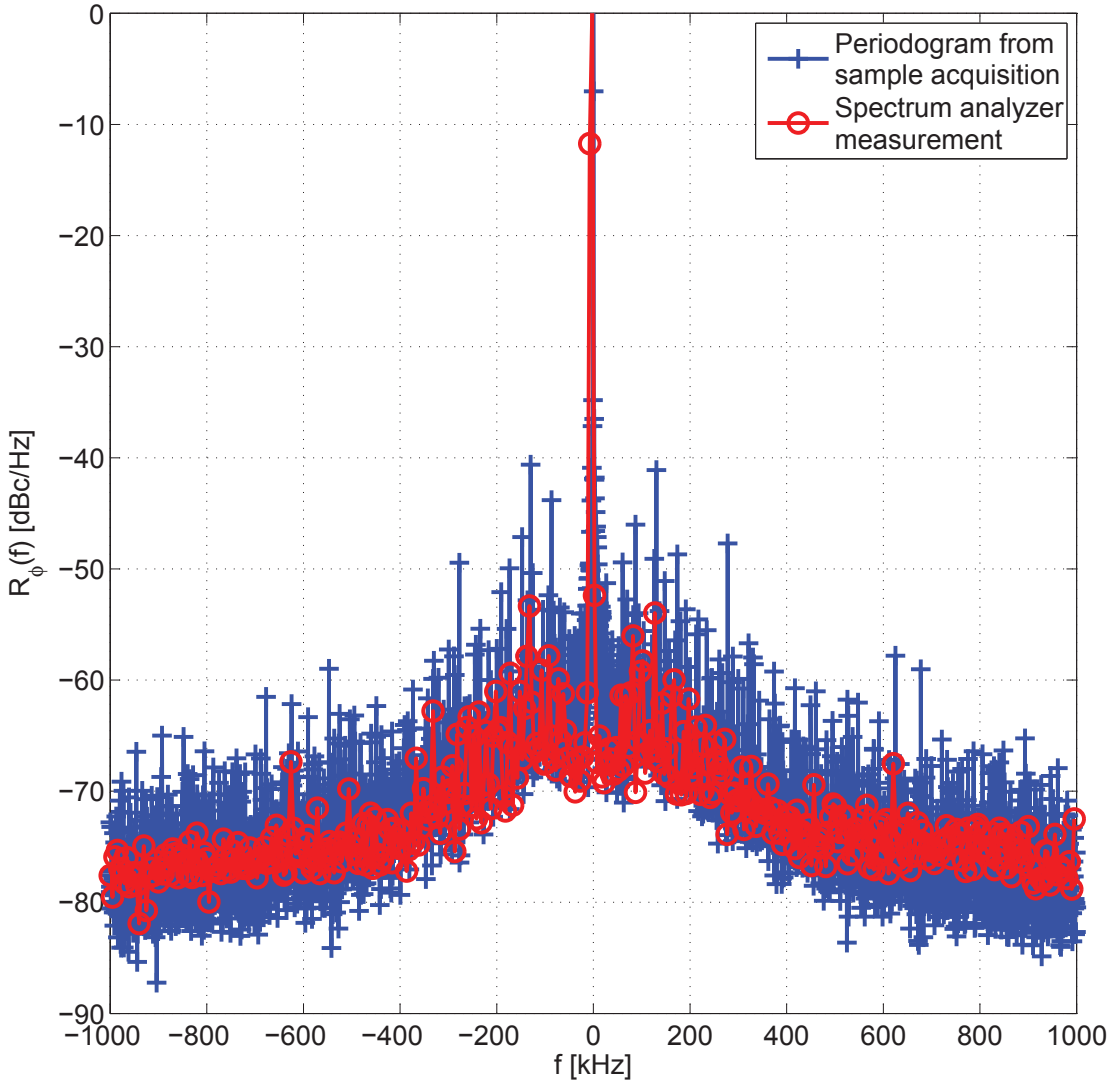

Figure 2.12: Measured phase noise spectrum.

$f_{in} = \frac{F_s}{N} \cdot k$, where k is an integer number. This number represents the number of complete waveform periods that have been acquired (in this example, $N = 1024$, $F_s = 26$ MHz, and $k = 50$). The tone amplitude A_{in} is -1 dBFS, where dBFS stands for dB *full scale*, i.e.,

$$A_{in}\ [\text{dBFS}] = 20 \log_{10} \left(\frac{A_{rms,in}}{A_{rms,max}} \right), \tag{2.5}$$

where $A_{rms,in}$ is the RMS amplitude of the applied signal, while $A_{rms,max}$ is the RMS amplitude of the maximum signal level, i.e., $\frac{x_{pp,max}}{2\sqrt{2}}$.

In Fig. 2.14, we have reported the unilateral version of the FFT spectrum, obtained by taking only half of the FFT points (in the example, $N_{fft} = 1024$), and multiplying the amplitudes by a factor of two. As it can be observed, we have also reported the FFT

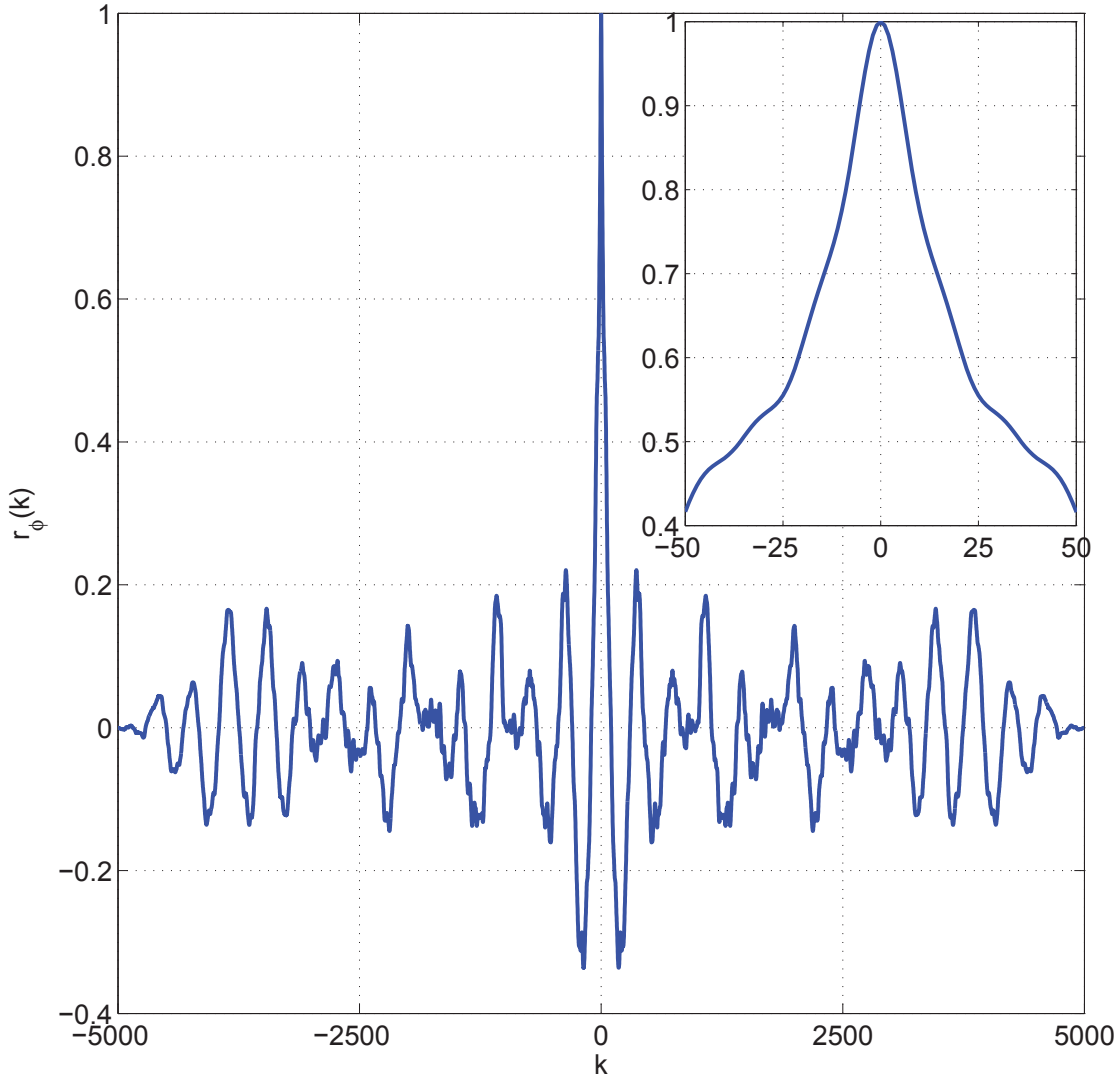

Figure 2.13: Phase noise temporal correlation evaluated over 10000 samples.

spectrum obtained when no signal is applied to the ADC (labeled "noise acquisition"). This trace is used to understand if the signal generator introduces a noise level larger than the ADC background noise. This does not occur in the example since the noise floors of the signal and noise acquisitions practically overlap.

If we denote with $A_{rms,n}$ the RMS amplitude of the n-th harmonic of the acquired signal, i.e., the RMS amplitude of the FFT spectrum at the frequency $n \cdot f_{in}$, $n = 2, 3, ..$, we can define the THD as the ratio between the root sum of the squared harmonics, and the RMS

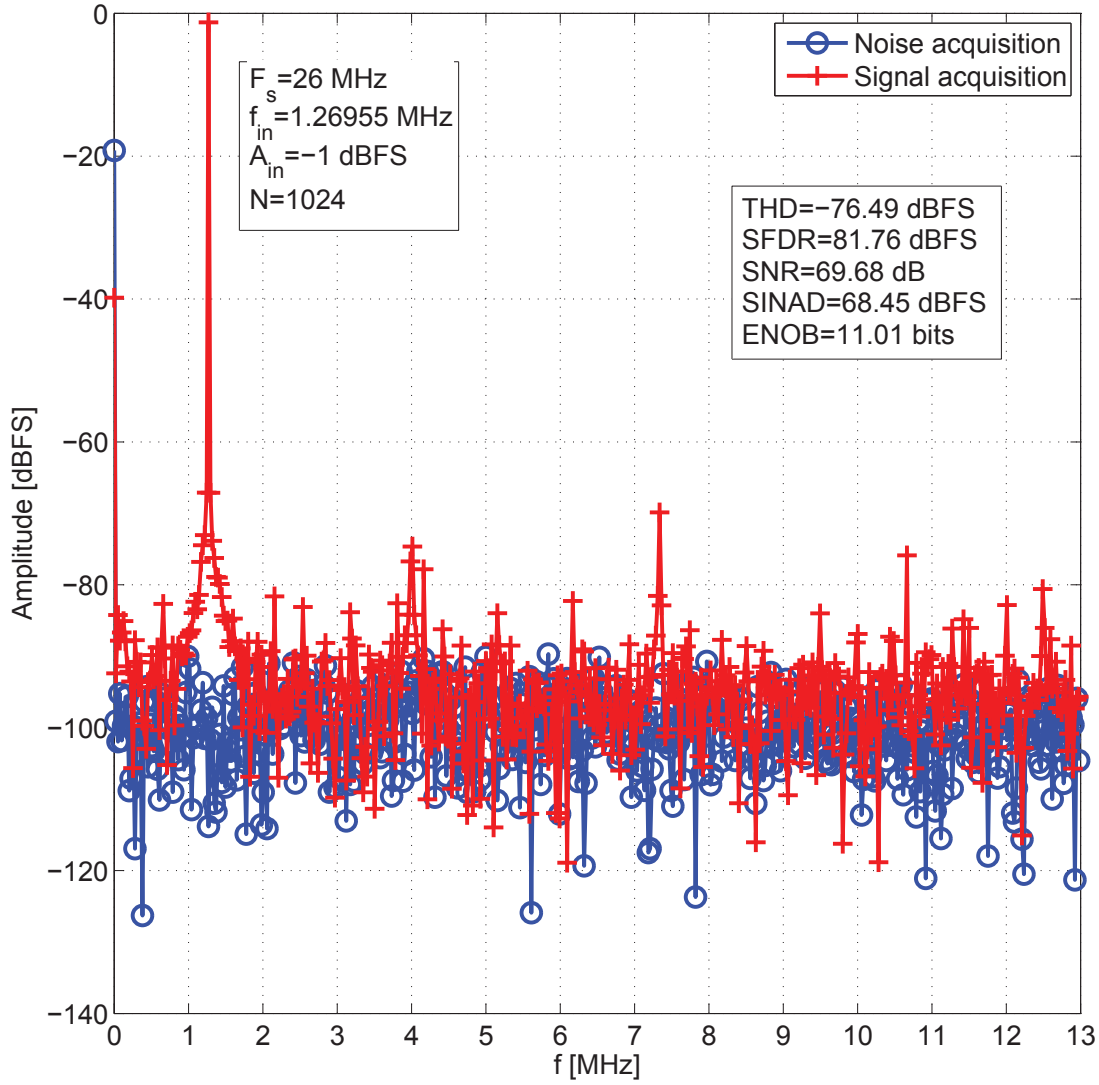

Figure 2.14: FFT output of a -1 dBFS single tone signal at 1.26955 MHz applied to the first ADC. $F_s = 26$ MHz, and $N = 1024$.

amplitude of the fundamental, i.e.,

$$\text{THD} = 20\log_{10}\left(\frac{\sqrt{\sum_{n=2}^{+\infty} A_{rms,n}^2}}{A_{rms,in}}\right). \tag{2.6}$$

In our example, THD= -76.49 dBFS.

Another important specification is the SFDR, defined as

$$\text{SFDR} = 20\log_{10}\left(\frac{A_{rms,max}}{\max_{n=2,3,..}\{A_{rms,n}\}}\right), \tag{2.7}$$

i.e., it is a measurement of the distance between the full scale level and the worst spur level. We have measured SFDR= 81.76 dBFS.

The SNR is instead defined as the ratio between the signal level and the noise floor, i.e., the FFT noise floor (in Fig. 2.14 is about -96 dBFS) plus $10\log_{10}\left(\frac{N_{fft}}{2}\right)$. We have found SNR= 69.68 dB that is a value very close to that provided by the manufacturer [28]. SINAD, instead, is a specification that includes both the noise floor and the distortion due to the harmonics. If N_0 denotes the noise floor in dBFS, the SINAD can be defined as

$$\text{SINAD} = 10\log_{10}\left(\frac{A_{rms,in}^2}{N_0 + \sum_{n=2}^{+\infty} A_{rms,n}^2}\right). \tag{2.8}$$

In our example, SINAD= -68.45 dBFS.

Finally, the ENOB is a measurement of the quality of the quantized signal. It specifies the number of bits in the digitized signals above the noise floor, and it can be defined as

$$\text{ENOB} = \frac{\text{SINAD} - 1.76 \text{ dB} + A_{in}}{6.02}, \tag{2.9}$$

where 1.76 dB is due to the quantization error of an ideal ADC, while 6.02 is the factor that converts decibels (a $\log_{10}$ representation) into bits (a $\log_2$ representation). Our ADC has ENOB= 11.01 bits.

These results highlight a good functioning of the ADC, and allow us to neglect these non linearities.

2.4 Hardware Impairments Modeling

In this section, we propose some statistical models derived from the results of the measurement campaign described above.

Noise and DC Offset

We have observed that the total noise, whose RMS values (in dBV) are shown in Fig. 2.9, is circularly symmetric complex Gaussian, with non zero mean (the DC offset), and statistical power N_0 equal to the values reported in Fig. 2.9. Usually, the performance of an algorithm is computed as function of the SNR at the receiver. From Fig. 2.10 we figure out that the considered hardware platform supports SNR up to approximately 65 dB.

To study the statistics of the DC offset, we would need a wide set of receivers, which is clearly not doable in our case. We infer a Gaussian distribution from the observation of the physical phenomena that determine it in a large number of hardware realizations. The Gaussian model was also proposed in [33]. Furthermore, we assume the DC offsets to be statistically independent among the receiver channels, with zero mean and a given

standard deviation. For example, the standard deviation of the measured DC offsets among the channels is equal to 10.6 mV.

Phase Noise, Carrier Frequency and Phase Offsets

In order to propose an analytical model for the phase noise, we use the parametric approach in [34] where the phase noise power spectrum is modeled as

$$R_{\phi}(f) = 10^{-c} + \begin{cases} 10^{-a} & ,|f| \leq f_1 \\ 10^{-|f-f_1|\frac{b}{f_2-f_1}-a} & ,|f| > f_1 \end{cases} \tag{2.10}$$

for certain parameters a, b, c, f_1, f_2. In particular, we have found that $a = 5.3$, $b = 3$, $c = 7.8$, $f_1 = 20$ kHz, and $f_2 = 500$ kHz provide a good fit between the analytical expression and the measured results, as shown in Fig. 2.15. Interestingly, as Fig. 2.16 shows, the PN in our hardware platform is significantly higher that the more benign PN model used in [34] where the parameters are $a = 6.5$, $b = 4$, $c = 10.5$, $f_1 = 1$ kHz, and $f_2 = 10$ kHz.

We also propose a statistical model for the observed PN process. As Fig. 2.17 shows, for a given receiver channel, it has a normal distribution with zero mean and standard deviation 1.57 deg. In the numerical analysis that we will present in this thesis, also a standard deviation of 1 deg will be considered. Similar values have been obtained for the other three channels. It has also been verified that the PN processes of distinct receivers are uncorrelated.

The PO $\Phi^{(i)}$ in (2.4), includes the POs among the transmit-receive RF oscillators, the contribution due to delays of the signals that propagate through different length cables connecting the array elements with the RF board, and the phase difference among not co-phased receiver LOs. These POs can be assumed uniformly distributed in the range $[0, 2\pi]$ and constant during the observation window.

The measurement of the CFOs has shown that it has small differences among the four receivers. The standard deviation of the values reported in Section 2.3 is approximately 100 Hz. Similarly to the DC offset case, to study the statistics of the CFOs we would need a wide set of receivers, which is not doable in our case. However, a Gaussian distribution can be inferred. Furthermore, we assume the frequency offset to be independent among the receivers, with identical mean $\mu_{CFO} = 15$ kHz and standard deviation $\sigma_{CFO} = 100$ Hz.

2.5 Main Findings

The measurements have revealed that the major impairments of our hardware platform are the DC offset, the CFOs, the PN and the different phases among the receiver signals that can be introduced by both the time delays of unequal cable connections between the array elements, and not co-phased LOs. We have found that the I&Q gain mismatch as well as

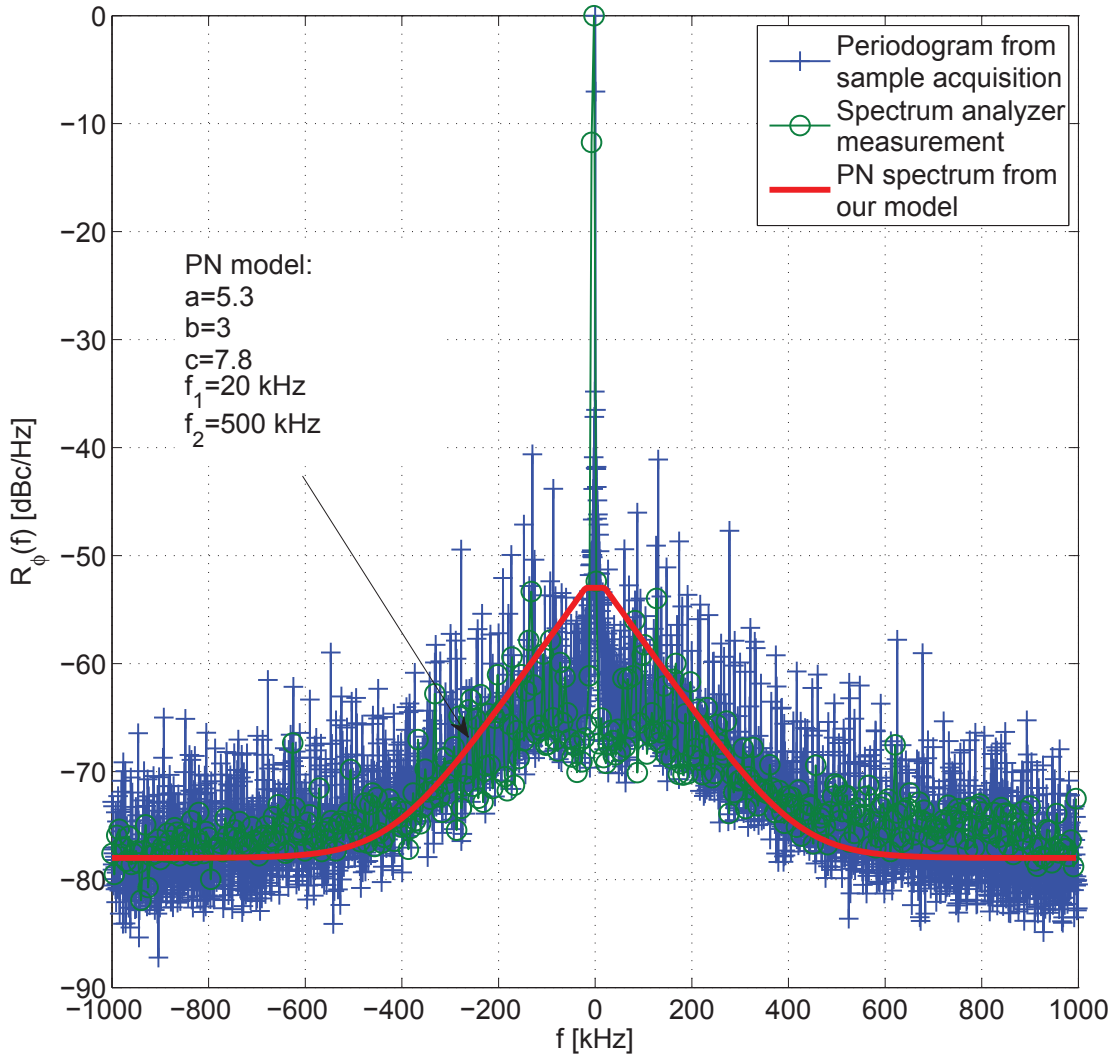

Figure 2.15: Measured phase noise spectrum and our model.

the sampling time offsets introduced by the ADCs are of negligible entity in our application context.

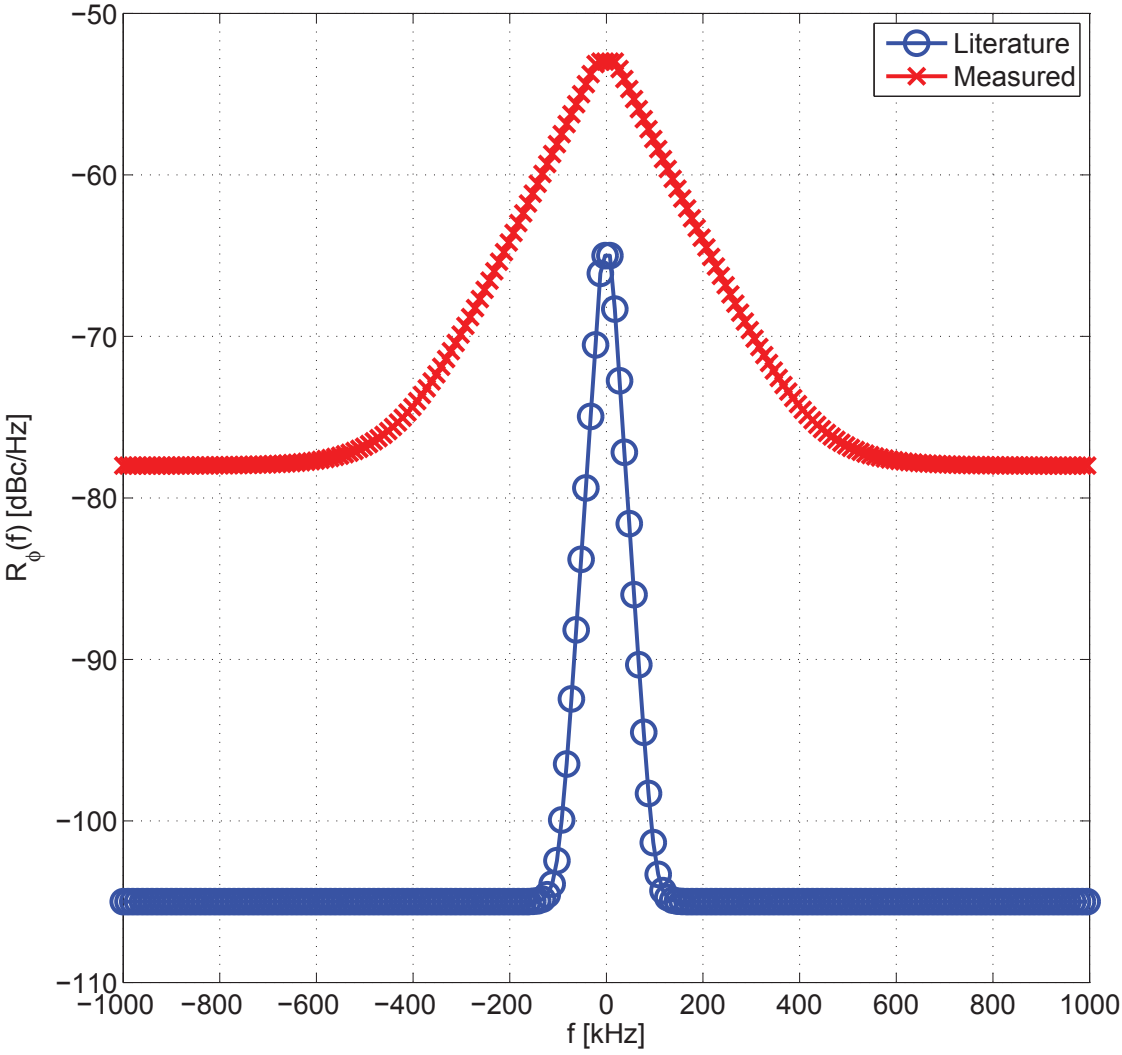

Figure 2.16: Phase noise spectrum models.

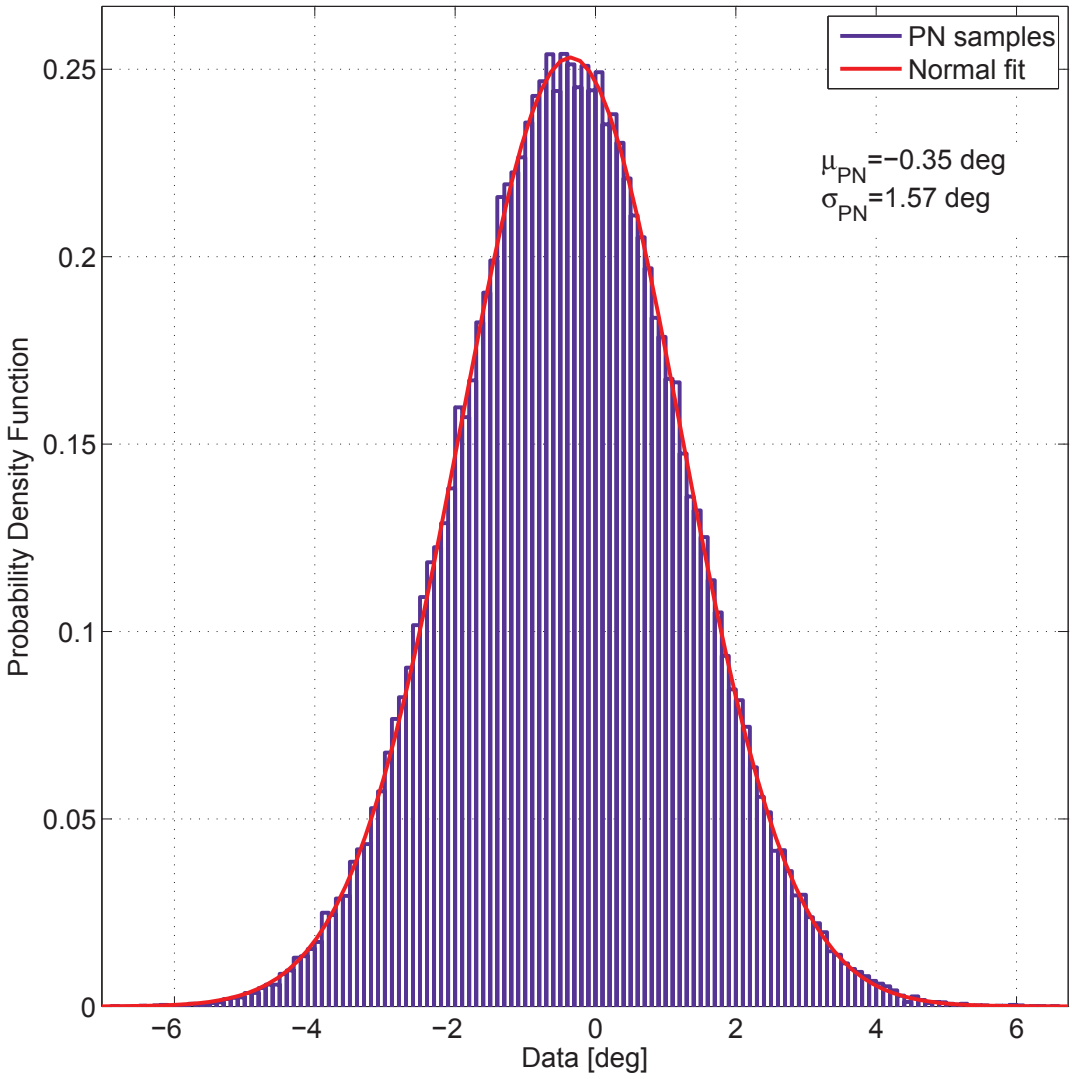

Figure 2.17: Probability density function of the measured phase noise.

Chapter 3

DoA Estimation in the Presence of Hardware Impairments

In Chapter 2 we have characterized and modeled several hardware impairments, such as DC offset, carrier frequency offset (CFO), phase offset (PO), and phase noise (PN), that can be found in a multiple antenna receiver with uncoherent local oscillators (LOs). In this chapter, we consider the DoA estimation problem. More precisely, we describe a low complexity DoA estimation algorithm, and we show how the above cited non idealities affect its performance. Furthermore, we highlight that the performance of our algorithm is comparable to the known root-MUSIC algorithm assuming that a single source is present.

3.1 Introduction

As described in Chapter 1, an important aspect in DoA estimation is the presence of non idealities that can severely affect the DoA estimation performance. The array uncalibration, i.e., the unperfect knowledge of the array manifold shape in (1.8), is among the most studied problems [35–37]. More precisely, phase and gain mismatches among antenna elements [35], mutual coupling [38], and some array manufacturing imperfections, e.g., an uncorrect displacement of single antenna elements [39], are usually addressed in the literature.

However, there are other impairments introduced by both the radio frequency (RF) and the acquisition (baseband) hardware stages that cannot be neglected. In Chapter 2 we have characterized different hardware impairments that, although they are usually considered in the context of data transmission systems, e.g., in [33, 40, 41], they are often neglected in the context of DoA estimation with antenna arrays. In particular, CFOs and POs can have a detrimental effect on the DoA estimation algorithm if they are not compensated for [42]. Furthermore, the presence of DC offsets and PN can also limit the performance of the estimator. Therefore, in this chapter we show the effect of such non idealities on the

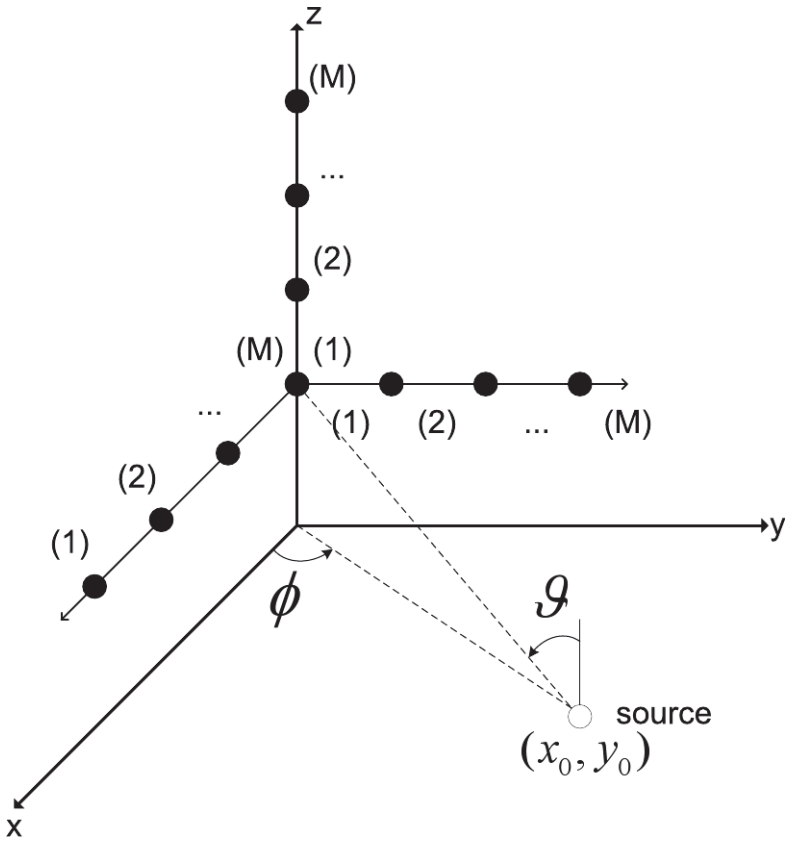

Figure 3.1: 3D L-shaped array configuration.

DoA estimation. Firstly, we propose a simple DoA estimation algorithm for 1D and/or 2D[1] DoA estimation that removes the DC offset and compensates the CFO among the receivers; secondly, it uses a time-multiplexed known direction source to perform the PO calibration and to increase the algorithm robustness to the PN.

We assume a single transmitting node in a plane waves line-of-sight (LOS) propagation scenario. Multiple node transmission can be accomplished by time or frequency multiplexing the node transmissions so that the single source model applies.

This chapter is organized as follows. In Section 3.2, the system model for DoA estimation with the hardware imperfections is presented. The proposed DoA estimation algorithm is described in Section 3.3. We study the mean-square-error performance of the estimator in Section 3.4. Finally, the main findings follow.

3.2 System Model for DoA Estimation

Using the impairment models derived in Chapter 2, we can obtain an overall system model. In particular, we consider a radio system with a receiver equipped with a 3D L-shaped antenna array [43], as shown in Fig. 3.1. The 3D L-shaped array has a total of $3M - 2$

[1]1D-DoA estimation denotes the estimation of the azimuth angle in the 2-D plane, while 2D-DoA estimation denotes the estimation of both azimuth and elevation in the 3-D space.

sensors, with three LES subarrays displaced along the x, y and z axes.

It is worth noting that the 2D-DoA estimation is a generalization of the 1D-DoA estimation. Now, we will describe the system model for the 2D-DoA case, but this model holds true also in the 1D-DoA case, where the antenna array is one of the LES subarrays used in the x or the y axes, and the elevation is assumed null.

Let us assume a source that emits a single tone signal $e^{j2\pi f_{0,RF}t}$ at radio frequency $f_{0,RF}$, a plane waves LOS propagation scenario, and that the plane wave impinges on the sensors of every subarray with azimuth ϕ and elevation angle ϑ. Thus, the incident complex signals at the a-th antenna subarray can be written as in (1.5), i.e.,

$$x_{RF}^{(a,i)}(t) = \rho e^{j2\pi f_{0,RF}(t-\tau^{(a)}-\Delta t^{(a,i)})} + w_{RF}^{(a,i)}(t), \tag{3.1}$$

where $\tau^{(a)}$ is the propagation delay between the emitter and the first sensor of each subarray, ρ is the propagation loss that we assume to be time invariant during the DoA estimation and identical for each antenna element, and $w_{RF}^{(a,i)}(t)$ is the additive noise. It should be noted that the index $i \in \{1, ..., M\}$, while the index $a \in \{x, y, z\}$. The differential propagation delay between the first sensor and the i-th sensor of a given subarray a can be expressed as

$$\Delta t^{(a,i)} = \begin{cases} \frac{d}{c_0}(i-1)\cos(\phi)\sin(\vartheta), & a = x \\ \frac{d}{c_0}(M-i)\sin(\phi)\sin(\vartheta), & a = y \\ \frac{d}{c_0}(i-1)\cos(\vartheta), & a = z \end{cases} \tag{3.2}$$

where d is the distance between the sensors, c_0 is the speed of light, and we assume $\phi \in [-\pi, \pi], \vartheta \in [0, \pi]$.

As described in Chapter 2, the received RF signals are down converted to low frequency f_0 using a direct conversion receiver architecture (depicted in Fig. 2.5) for the sensor of indices (a, i). The signal down conversion for each sensor is obtained with a LO with frequency $f_{LO}^{(a,i)} = f_{0,RF} - f_0 - f^{(a,i)}$, where $f^{(a,i)}$ represents the CFO. The desired low frequency f_0 is chosen larger than 0 to filter out the DC offset component at zero frequency as discussed in the next section.

Now, assuming to sample the signals with period T, the sequence of complex samples $x^{(a,i)}(nT)$ associated to the i-th sensor of the a-th subarray, can be written (according to the results in Chapter 2) as

$$x^{(a,i)}(nT) = Se^{j(\psi^{(a,i)}(nT)+\varphi^{(a,i)}(nT)-\Phi^{(a,i)})} + w^{(a,i)}(nT) + w_{DC}^{(a,i)}, \tag{3.3}$$

where

$$\psi^{(a,i)}(nT) = 2\pi(f_0 + f^{(a,i)})nT - 2\pi f_{0,RF}\tau^{(a)} - 2\pi f_{0,RF}\Delta t^{(a,i)}, \tag{3.4}$$

$\varphi^{(a,i)}(nT)$ represents the PN process and $\Phi^{(a,i)}$ is the PO for the sensor of indices (a, i).

Furthermore, $S = \rho g$ is the signal amplitude (assumed to be identical for each receiver) that includes the propagation loss ρ and the receiver gain g. We denote with $w^{(a,i)}(nT)$ the background noise contribution, while $w_{DC}^{(a,i)}$ is the constant DC offset component.

For the performance analysis, it is useful to define the signal to background noise ratio (SNR) as

$$\mathrm{SNR} = \frac{S^2}{N_0}, \tag{3.5}$$

where N_0 is the background noise variance.

Our goal is the estimation of the 2D-DoA, i.e., the estimation of the azimuth and elevation angles, by observing the signals (3.3). This can be done through the exploitation of the phase differences $2\pi f_{0,RF}\Delta t^{(a,i)}$ among the sensors that are due to different propagation delays of signals captured by the sensors. Unfortunately, the presence of hardware impairments, in particular the CFO $f^{(a,i)}$, the PO $\Phi^{(a,i)}$, and the PN $\varphi^{(a,i)}(nT)$ cause a phase uncertainty as shown in (3.3) and (3.4). Furthermore, we have to deal with the DC offset component $w_{DC}^{(a,i)}$. To compensate these hardware impairments we propose the algorithm described in the next section.

3.3 Impairment Compensation and DoA Estimation

The proposed algorithm for the estimation of the DoA in the presence of the hardware impairments comprises the following main steps:

- We filter the signals to mitigate the DC offset and we perform a pre-calibration procedure to estimate the POs among all the receiving antennas and compensate them.
- We correlate pairs of antenna element signals to remove the CFOs. In the following we refer to the correlation of signals, i.e., the product of a signal with the complex conjugate of another, as *differential operation*.
- We perform averaging in time and space and finally compute the angles of arrival (ϕ, θ).

3.3.1 DC Offset Compensation

To attenuate the DC offset we filter the acquired signal $x^{(a,i)}(nT)$ with a high pass filter choosing a f_0 larger than 0. In this way, we obtain SDR values larger than those in Fig. 2.11. In the remainder of this paper, wherever DC offset is mentioned, it means the uncompensated part of the DC offset due to the limited filter attenuation, or the dynamic DC offset contributions, as explained in Chapter 2.

3.3.2 Frequency and Phase Offset Compensation

We assume the CFOs to be identical on the same subarray, i.e., $f^{(a,i)} = f^{(a)},\ \forall i \in [1, M]$. This assumption is practically true from the results in Chapter 2. Nevertheless, the effect of non-identical CFOs as well as the effect of the PN (that we neglect in the algorithm derivation) will be considered later. Then, we perform a differential operation among pairs of signals from elements that belong to the same subarray. Now, the signal at the output of the differential combiner can be written as

$$\begin{aligned} z^{(a,i)}(nT) &= x^{(a,i)}(nT) \cdot x^{(a,i+1)^*}(nT) \\ &= S^2 e^{j(\hat{\psi}^{(a)} - \hat{\Phi}^{(a,i)})} + \hat{w}^{(a,i)}(nT),\ i \in \{1, .., M-1\}, \end{aligned} \tag{3.6}$$

where

$$\hat{\psi}^{(a)} = \begin{cases} 2\pi f_{0,RF} \frac{d}{c_0} \cos(\phi) \sin(\vartheta), & a = x \\ -2\pi f_{0,RF} \frac{d}{c_0} \sin(\phi) \sin(\vartheta), & a = y \\ 2\pi f_{0,RF} \frac{d}{c_0} \cos(\vartheta), & a = z. \end{cases} \tag{3.7}$$

As (3.6) reveals, the time variant phase ambiguity $2\pi(f_0 + f^{(a)})nT$ introduced by the CFO in (3.4) is removed, and we are left with: a) the phase $\hat{\psi}^{(a)}$ of interest that is a function of the angles of arrival (ϕ, θ), according to (3.7); b) the phase difference $\hat{\Phi}^{(a,i)} = \Phi^{(a,i)} - \Phi^{(a,i+1)},\ a \in \{x, y, z\},\ i \in \{1, .., M-1\}$ between the i-th and the $i+1$-th receiver of the a-th subarray.

Now, we consider the PO $\hat{\Phi}^{(a,i)}$ compensation. Assuming that the contribution to $\Phi^{(a,i)}$ is due to both not co-phased LOs and fabrication variations in the RF receiver stage, we can compensate $\hat{\Phi}^{(a,i)}$ by injecting a local reference signal on each input receiver as in [35]. In this way, the phases $\hat{\psi}^{(a)},\ a \in \{x, y, z\}$ in (3.6) become null, and we can estimate the PO $\hat{\Phi}^{(a,i)}$ from (3.6). Hence, we assume to perform the pre-calibration just before the DoA estimation, i.e., to time multiplex the acquisition of the reference signal and the acquisition of the unknown direction signals.

3.3.3 DoA Estimation

The 2D-DoA can be estimated from (3.6). The samples $z^{(a,i)}(nT)$ in (3.6) are averaged in time and in space to increase the immunity to noise after the compensation of the PO $\hat{\Phi}^{(a,i)}$ (estimated in the pre-calibration procedure) as follows

$$\begin{aligned} z^{(a)} &= \frac{1}{N(M-1)} \sum_{n=0}^{N-1} \sum_{i=1}^{M-1} z^{(a,i)}(nT) e^{j\hat{\Phi}^{(a,i)}} \\ &= S^2 e^{j\hat{\psi}^{(a)}} + W^{(a)}, \end{aligned} \tag{3.8}$$

where $W^{(a)}$ is the complex noise contribution.

Now, with the array configuration in Fig. 3.1 we can process the signals $z^{(x)}$, $z^{(y)}$ and

$z^{(z)}$ in (3.8) to estimate the angles of arrival as follows

$$\begin{aligned}\tilde{\phi} &= -\arctan2\left(\angle z^{(y)}, \angle z^{(x)}\right) \\ \tilde{\vartheta} &= \arctan2\left(\sqrt{(\angle z^{(x)})^2 + (\angle z^{(y)})^2}, \angle z^{(z)}\right),\end{aligned} \tag{3.9}$$

where $\arctan2\,(y, x)$ is defined as

$$\arctan2(y,x) = \begin{cases} \arctan\left(\frac{y}{x}\right), & x > 0 \\ \pi + \arctan\left(\frac{y}{x}\right), & y \geq 0, x < 0 \\ -\pi + \arctan\left(\frac{y}{x}\right), & y < 0, x < 0 \\ \frac{\pi}{2}, & y > 0, x = 0 \\ -\frac{\pi}{2}, & y < 0, x = 0 \end{cases} \tag{3.10}$$

(we have assumed that $\arctan2\,(0, 0) = 0$). It should be noted that in the case of 1D-DoA estimation, the DoA estimator becomes

$$\tilde{\phi} = \begin{cases} -\arccos\frac{\angle z^{(x)}}{\kappa}, & \text{with the } x \text{ subarray} \\ \arcsin\frac{\angle z^{(y)}}{\kappa}, & \text{with the } y \text{ subarray.} \end{cases} \tag{3.11}$$

3.4 Performance Analysis

In this section, we report the performance analysis of the proposed 2D-DoA estimation algorithm in terms of aggregate *root mean squared error* (RMSE) defined as

$$\text{RMSE} = \sqrt{E\{(\phi - \tilde{\phi})^2 + (\vartheta - \tilde{\vartheta})^2\}}, \tag{3.12}$$

where $E\{.\}$ is the expectation operator.

In the numerical examples (obtained via simulations), we have assumed $\frac{1}{T} = 50$ MHz, $f_{0,RF} = 2.413$ GHz, $f_0 = 1$ MHz, and antenna elements spaced by $d = \frac{\lambda_0}{2}$. Also, where not specified, we have considered $N = 1$. The number of elements of the array is $3M - 2 = 10$, in particular $M = 4$ antennas per subarray are used with the central element shared among the three subarrays. We have found, via simulation, that with this number of antennas we obtain sufficient performance in the DoA estimation. It should be noted that the required number of channels is larger than that of the hardware configuration that we have used in Chapter 2. However, the model we have derived is applicable to any number of antennas. CFO, DC offset, and PN have been modeled as described in Chapter 2. However, the standard deviation of the CFO have been considered as a simulation parameter, while the standard deviation of the PN has been taken as $\sigma_{PN} = 1$ deg.

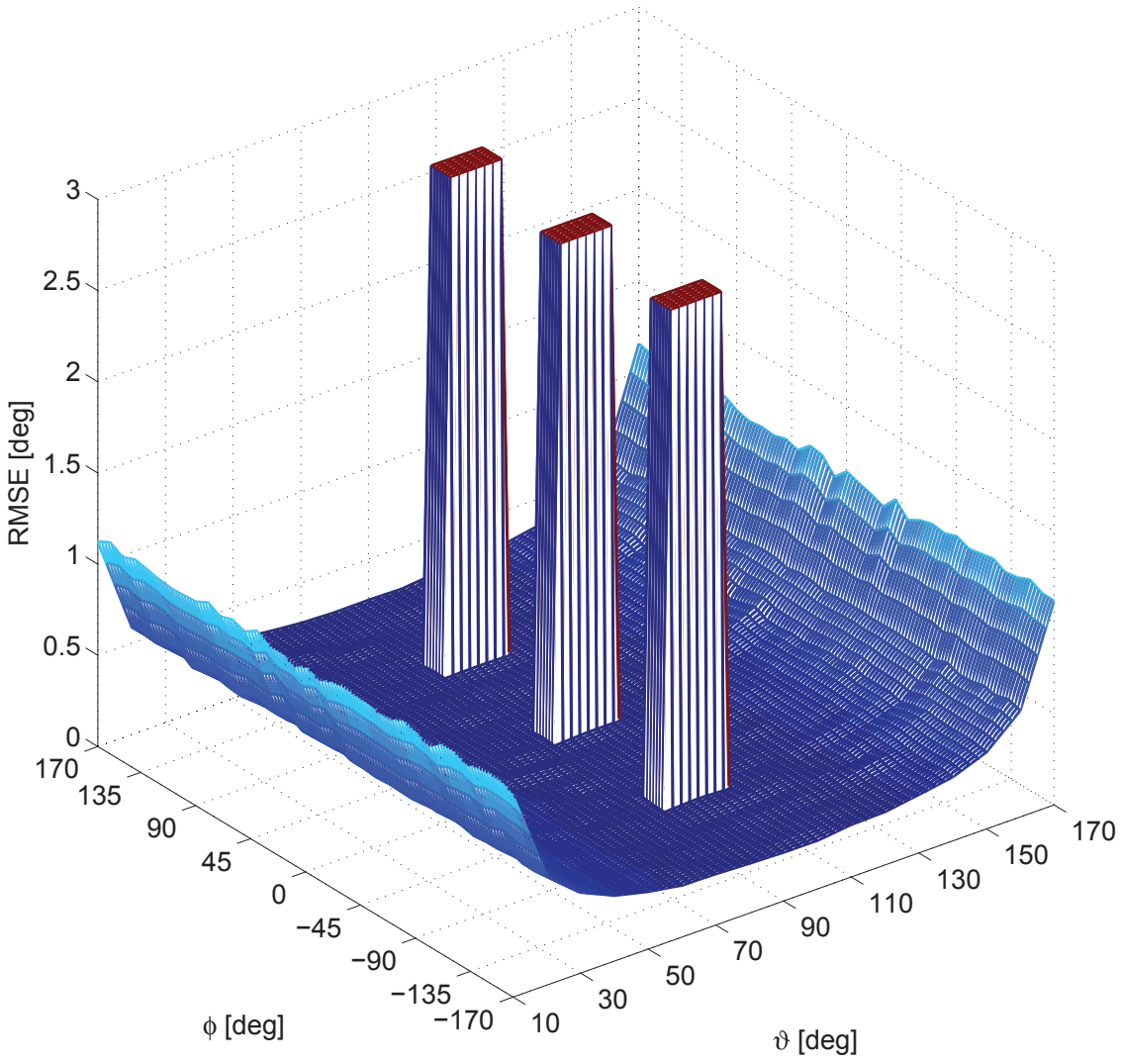

Figure 3.2: Aggregate RMSE as a function of azimuth and elevation angles.

3.4.1 Performance as a function of the Angles of Arrival

In Fig. 3.2, the aggregate RMSE is shown as a function of the azimuth and elevation angles, estimated when SNR= 30 dB in the absence of impairments. For the sake of graphical representation clarity, the RMSE has been drawn for angular values in the range $\phi = [-170°, 170°]$, $\vartheta = [10°, 170°]$, and it has been truncated when it exceeds the values of 3°. As we can see, the overall RMSE is always lower than 1.5°, except when $\vartheta = 90°$ and $\phi = -90°$, $\phi = 0°$ or $\phi = 90°$ where the RMSEs have been truncated. In these cases the estimator fails since the argument of the arctan2 function in (3.9) goes either to zero or to infinity but it has a wrong sign because of the presence of noise.

Now, we focus our analysis on the effects of the described hardware impairments con-

sidering $\phi = 30°$ and $\vartheta = 50°$. The results do not significally change for different values of ϕ and ϑ. To benchmark the performance, we have also considered the root-MUSIC [18] algorithm appropriately adapted to our case. The main steps are described below.

3.4.2 Root-MUSIC

We extend the root-MUSIC algorithm [18] to work with both azimuth and elevation, and to perform a pre-calibration as in our method. Firstly, we determine the estimated autocorrelation matrix

$$\boldsymbol{R}^{(a)} = \frac{1}{N}\sum_{n=0}^{N-1} \boldsymbol{x}^{(a)}(nT)\boldsymbol{x}^{(a)^H}(nT) \tag{3.13}$$

over N samples for each subarray, where $\boldsymbol{x}^{(a)}(nT) = [x^{(a,1)}(nT)x^{(a,2)}(nT)..x^{(a,M)}(nT)]^T$, $.^T$ is the transposition operator and $.^H$ is the complex conjugate of the transposition operator. This matrix has to be computed using both the reference signal samples (we denote it as $\boldsymbol{R}_c^{(a)}$) and the unknown direction signal (we denote it simply as $\boldsymbol{R}^{(a)}$). Now, the pre-calibration can be obtained by multiplying these matrices with a Hadamard product (denoted with the symbol $\circ$) to obtain the compensated autocorrelation matrix

$$\hat{\boldsymbol{R}}^{(a)} = \boldsymbol{R}^{(a)} \circ \boldsymbol{R}_c^{(a)^*}. \tag{3.14}$$

We find the eigendecomposition of $\hat{\boldsymbol{R}}^{(a)} = \boldsymbol{Q}^{(a)}\boldsymbol{\Lambda}^{(a)}\boldsymbol{Q}^{(a)^H}$, and we determine the partition $\boldsymbol{Q}_n^{(a)}$ of the eigenvector matrix $\boldsymbol{Q}^{(a)}$ associated to the smallest $M-1$ eigenvalues. The $\boldsymbol{Q}_n^{(a)}$ matrix is the eigenvector matrix that spans the noise subspace. From the matrix $\boldsymbol{C}^{(a)} = \boldsymbol{Q}_n^{(a)}\boldsymbol{Q}_n^{(a)^H}$, we obtain the coefficients $C_l^{(a)}$ by summing the elements of the l-th subdiagonal of $\boldsymbol{C}^{(a)}$. Now, we compute the $M-1$ roots of the polynomial with coefficients $C_l^{(a)},\ l \in \{0,..,M-1\}$. Finally, we pick the root closest to the unit circle, namely $z^{(a)}$. From the values $z^{(a)},\ a \in \{x,y,z\}$ we determine the angles of arrival as in (3.9).

We can observe that the CFO is partially compensated with the autocorrelation matrix derivation. In fact, we can interpret it as a sort of extended differential operation among all the possible pairs of antenna elements.

It is clear that the complexity of this algorithm is considerably higher than the proposed one.

3.4.3 Hardware Impairment Effects and Comparison with root-MUSIC

In Fig. 3.3, we can observe the aggregate RMSE as a function of SNR for some different values of SDR measured at the output of the DC offset compensation stage. As we can see an error floor in the RMSE curves is determined by the presence of the DC offset. The larger the DC offset power (the lower the SDR), the larger the RMSE is.

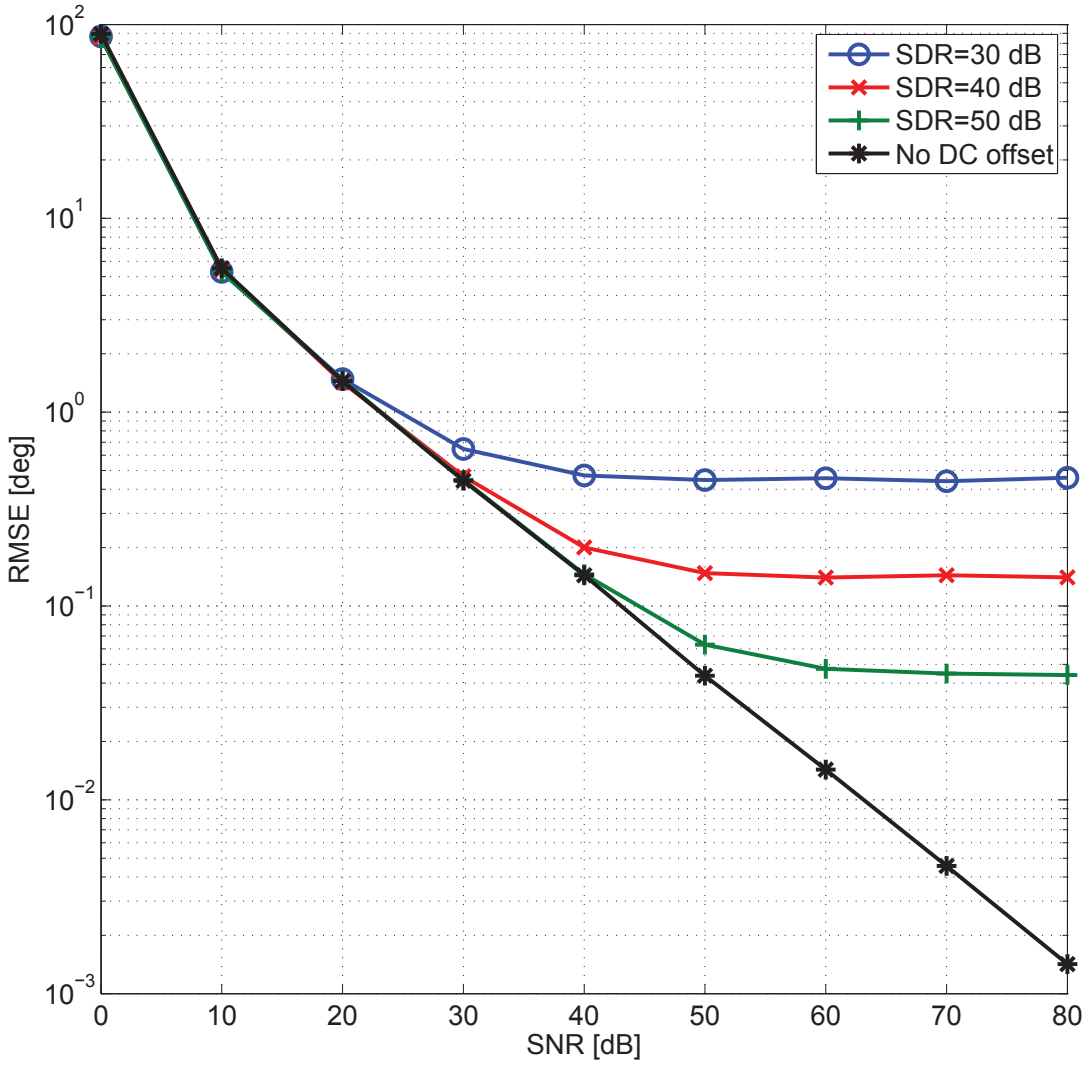

Figure 3.3: Aggregate RMSE obtained with our method as a function of both SNR and SDR.

A comparison between the algorithm in Section 3.3 and the root-MUSIC is shown in Fig. 3.4. This has been done for two different values of DC offset power, SDR= 30 dB and SDR= 50 dB. As it can be observed, the proposed estimator exhibits comparable performance than the root-MUSIC.

In Fig. 3.5, we consider the case of unequal frequency offsets among the channels. The aggregate RMSE curves are shown as a function of the CFO standard deviation σ_{CFO} and the number of snapshots N, with SNR= 30 dB. We have not considered the CFO mean value μ_{CFO} as a simulation parameter because it is perfectly compensated by the algorithm, so it is not a source of error. We can observe that the larger σ_{CFO}, the larger the RMSE is. Furthermore, for low values of σ_{CFO}, the increase of N is beneficial because the average reduces the noise. But, with the increase of σ_{CFO}, the increase of N is detrimental because

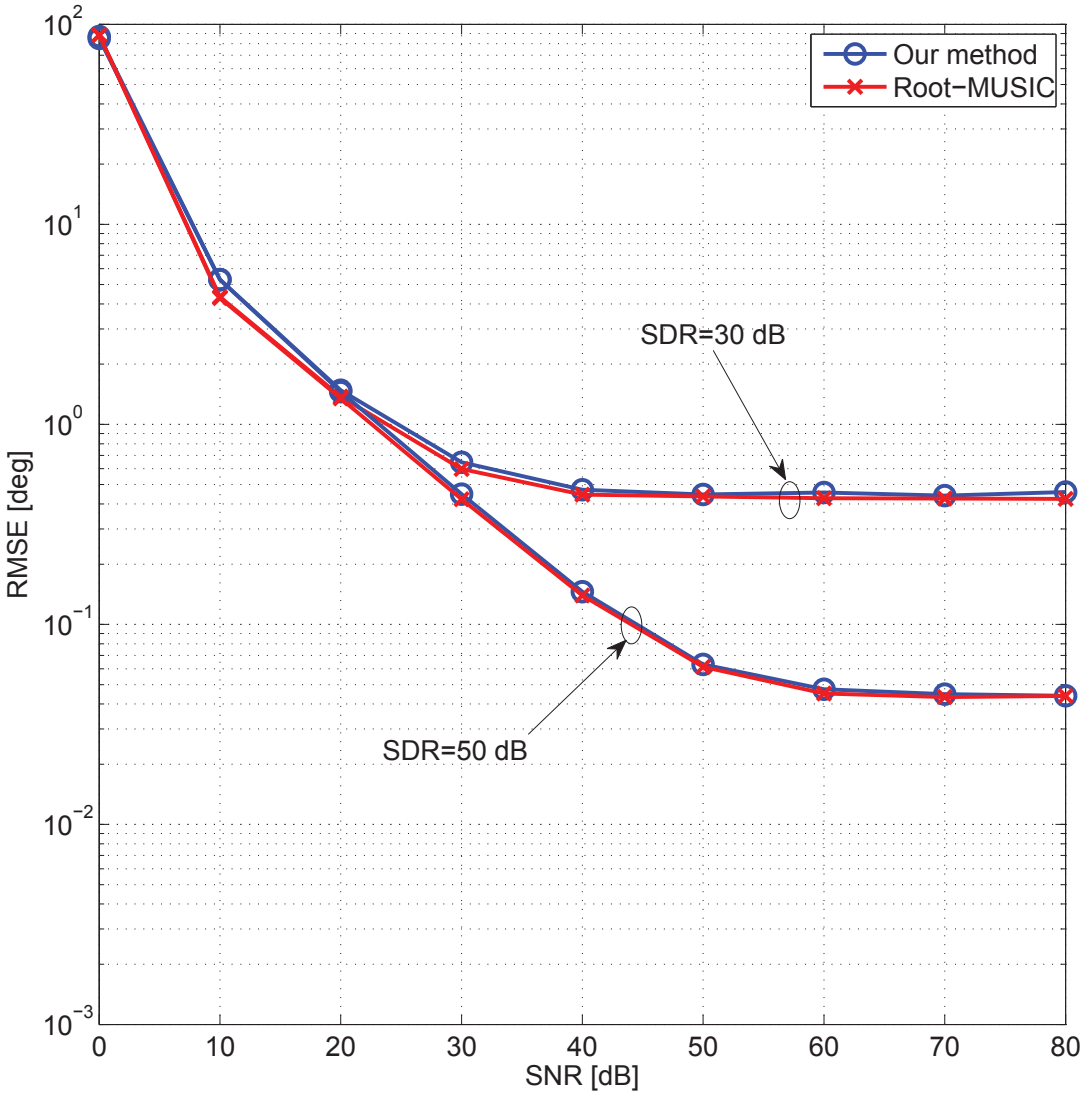

Figure 3.4: Aggregate RMSE with our method and root-MUSIC as a function of both SNR and SDR.

the phase error introduced by the non perfect compensation of the CFO is accumulated over N samples. In fact, if $f^{(a,i)} \neq f^{(a,i+1)},\ a \in \{x, y, z\},\ i \in \{1, .., M-1\}$, (3.8) becomes

$$z^{(a)} = \eta^{(a)} S^2 e^{j(\psi^{(a)}+\epsilon^{(a)})} + W^{(a)} \tag{3.15}$$

where

$$\eta^{(a)} e^{j\epsilon^{(a)}} = \frac{1}{N(M-1)} \sum_{n=0}^{N-1} \sum_{i=1}^{M-1} e^{j2\pi(f^{(a,i)}-f^{(a,i+1)})nT}. \tag{3.16}$$

For this reason, the value N has to be chosen so that a trade off is made between the increase of the signal to noise ratio and the increase of the phase error due to the CFO.

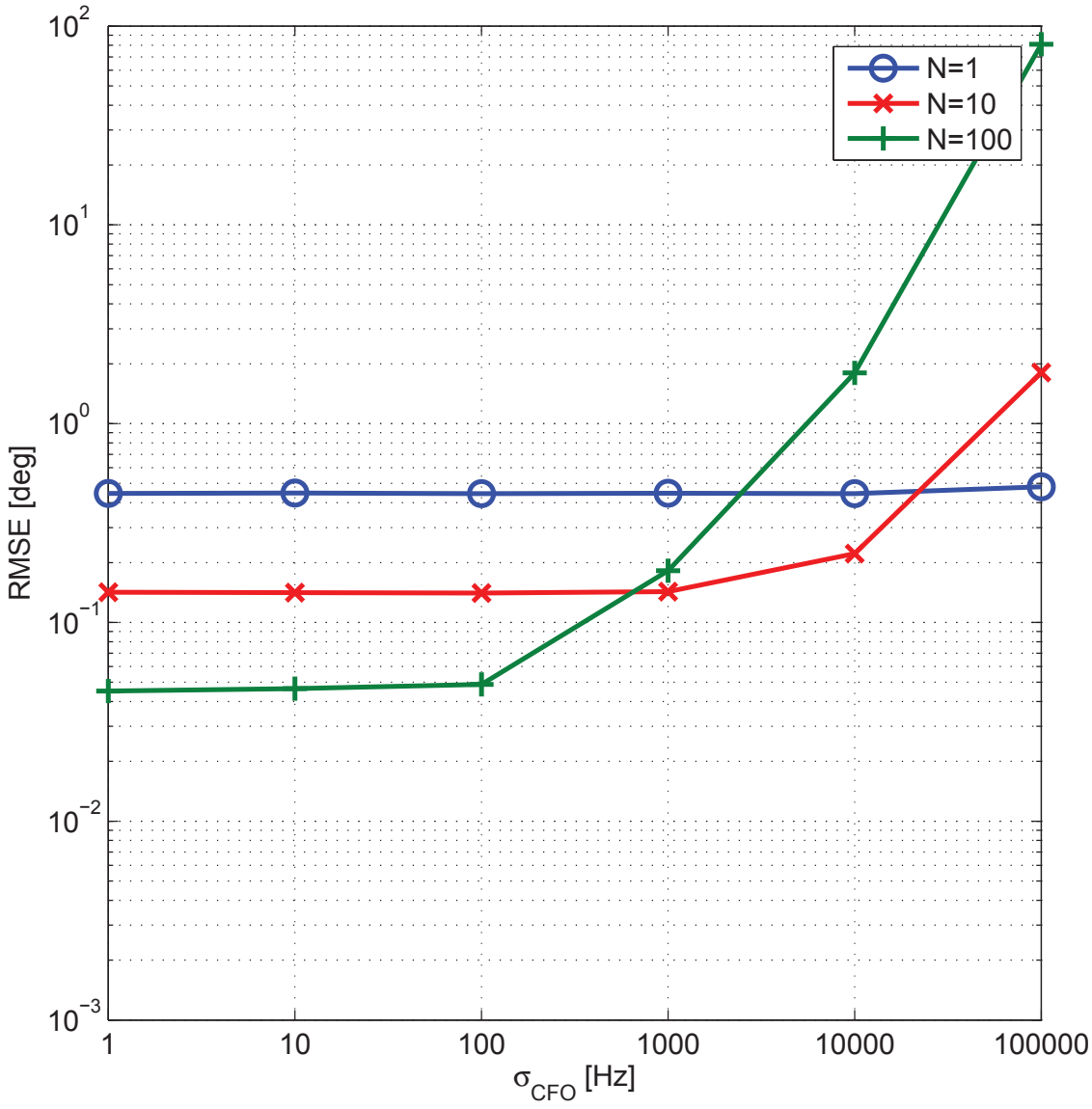

Figure 3.5: Aggregate RMSE obtained with our method as a function of σ_{CFO} and N.

In Fig. 3.6, we show a comparison with the root-MUSIC. We have considered the sensitivity to CFO for $N = 10$ and $N = 100$. Even here the root-MUSIC manifests a similar performance. In this figure, we also show the 90% confidence intervals for each point of the aggregate RMSE curves. As it can be seen, these intervals are very similar between the two methods. Therefore, the variation of the performance w.r.t. the mean value (the aggregate RMSE) is also similar between these two methods.

In Fig. 3.7, we have considered the RMSE curves as a function of the SNR, N, with or without simulated PN. Interestingly, we observe that the PN does not introduce any significant degradation of performance up to SNR= 50 dB for $N = 1$, and up to SNR= 30 dB for $N = 10$. This is because the PN is partly compensated by the PO pre-calibration

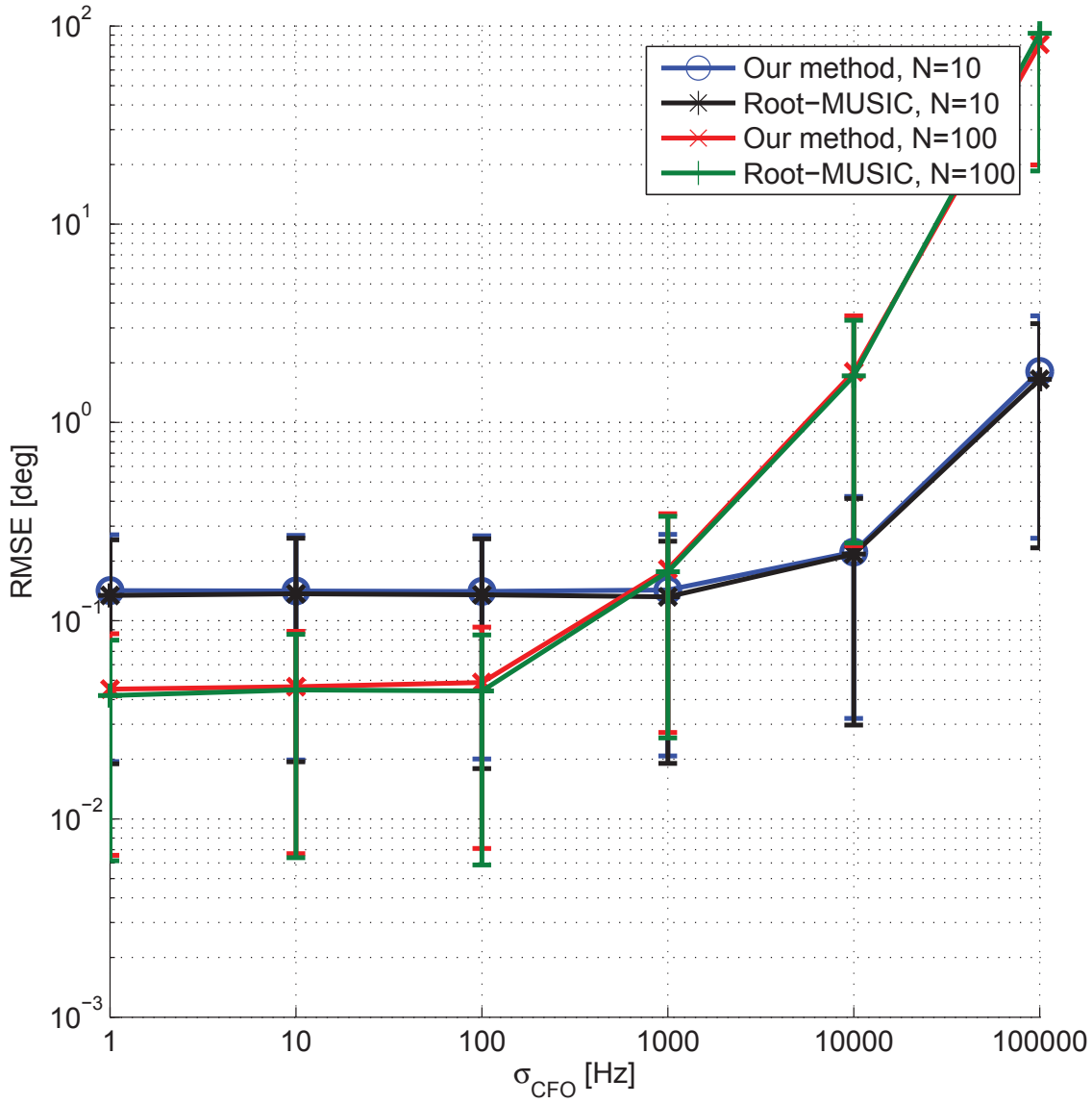

Figure 3.6: Aggregate RMSE (and 90% confidence intervals) with our method and root-MUSIC as a function of σ_{CFO} and N.

procedure. In fact, considering the PN contribution, (3.6) becomes

$$z^{(a,i)}(nT) = S^2 e^{j\{\hat{\psi}^{(a,i)} - \hat{\Phi}^{(a,i)} - \hat{\varphi}^{(a,i)}(nT)\}} + \hat{w}^{(a,i)}(nT) \tag{3.17}$$

where $\hat{\varphi}^{(a,i)}(nT) = \varphi^{(a,i)}(nT) - \varphi^{(a,i+1)}(nT)$ is the resulting PN contribution. When the pre-calibration step is performed, we estimate the total phase as the sum of the contributions of the PO $\hat{\Phi}^{(a,i)}$ and the PN $\hat{\varphi}^{(a,i)}(nT)$. Since the PN is slowly time variant in the estimation window as shown in Chapter 2, the pre-calibration procedure that we do just before the DoA estimation compensates well the PN contribution. To confirm this, in Fig. 3.8 we

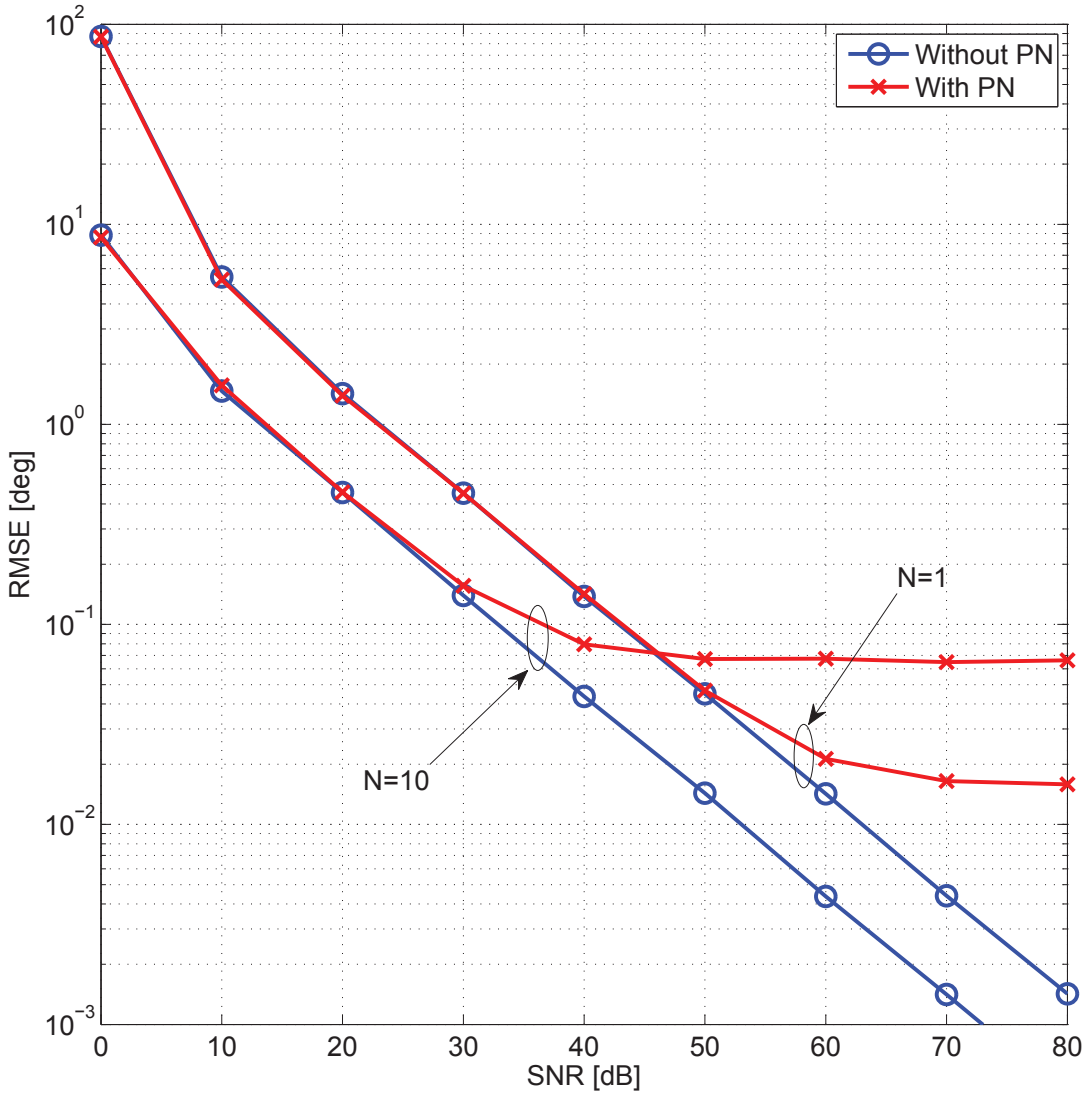

Figure 3.7: Aggregate RMSE with our method as a function of SNR, N, and the presence or not of phase noise.

show the performance of our method with the measured temporally correlated PN, and with temporally uncorrelated PN. As it can be observed, the performance of our method in the case of temporally correlated PN overcomes the method with temporally uncorrelated PN. Nonetheless, while in the case of temporally correlated PN the number of samples increases is not beneficial, Fig. 3.8 shows that in the other case the PN effect is mitigated by the averaging operation of (3.8).

Finally, in Fig. 3.9, we make a comparison with the root-MUSIC and, as the other cases, our estimator manifests similar performance to this method.

It should be noted that the proposed method has been compared with root-MUSIC only via simulations and not analytically. This is due to the difficulty to evaluate the RMSE

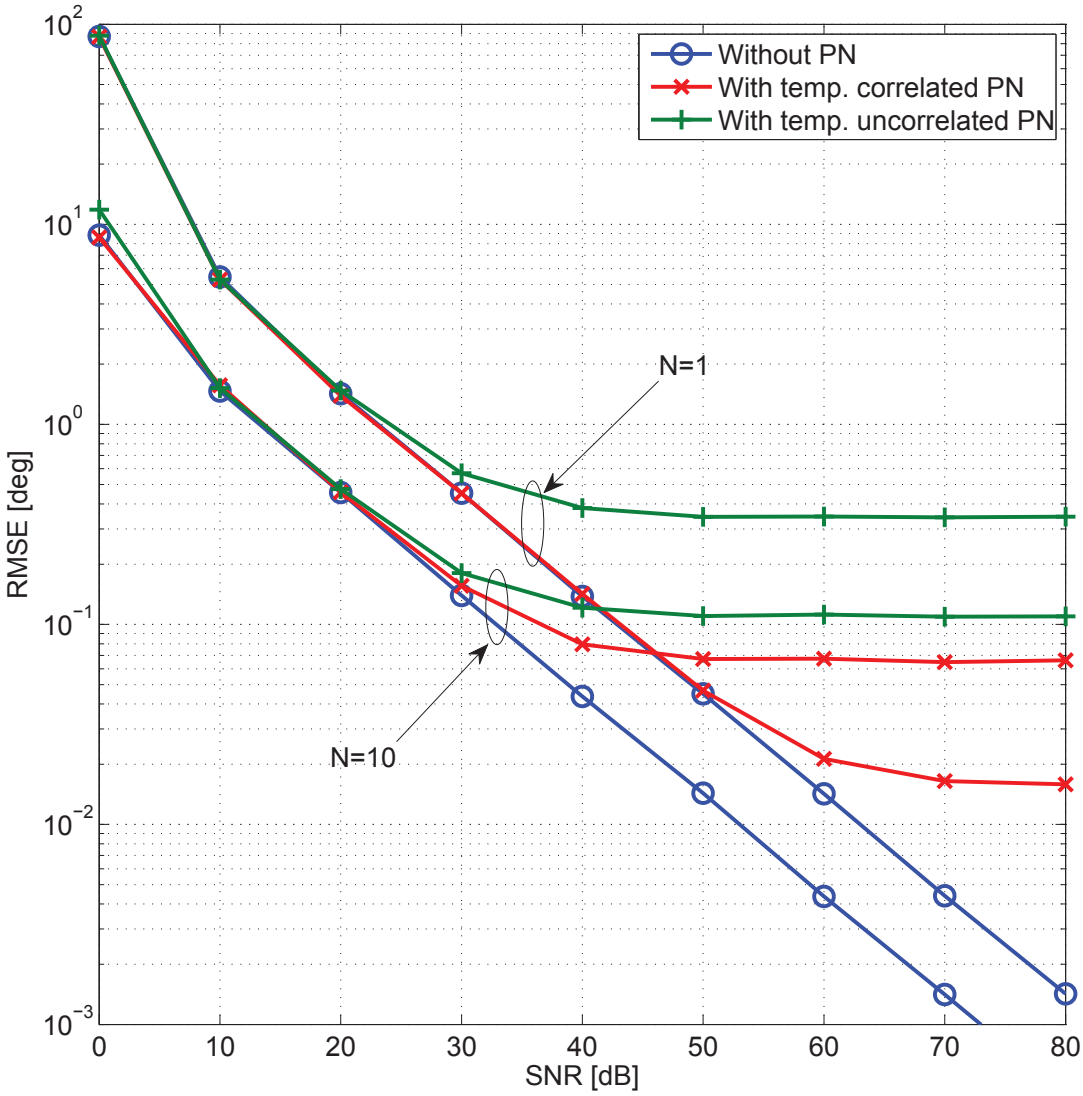

Figure 3.8: Aggregate RMSE with our method as a function of SNR, N, and the presence or absence of both temporally correlated and temporally uncorrelated phase noise.

when the arctan operator is involved, not only for the proposed method but also for the root-MUSIC. In fact, in the literature, the performance of DoA estimators are usually expressed through a bound, e.g., the Cramer-Rao bound as shown in the introduction, that describes the best attainable performance achieved with a maximum likelihood estimator. However, this bound is identical for both the compared methods since the considered system models are identical. Therefore, in order to understand the effective behaviour of these DoA estimators, a simulation comparison is necessary.

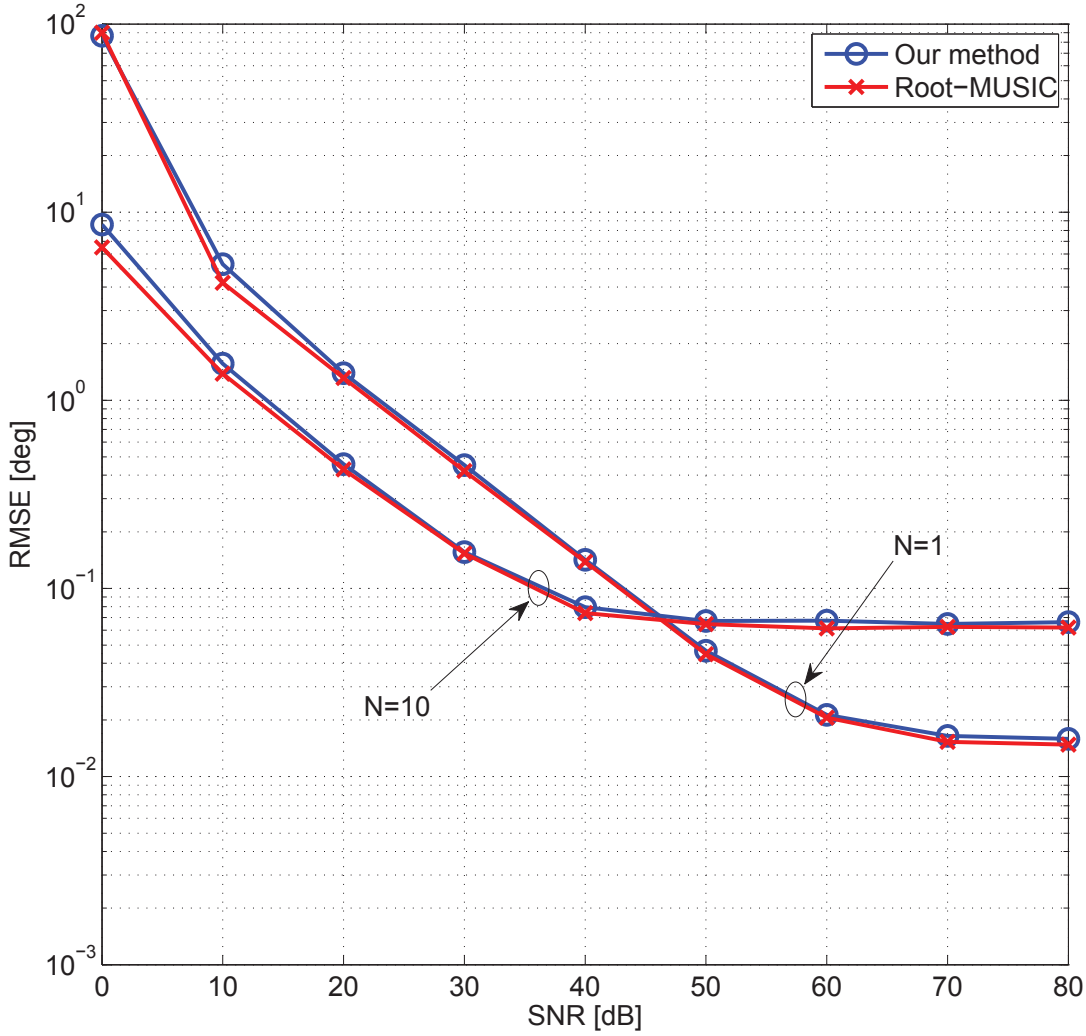

Figure 3.9: Aggregate RMSE with our method and root-MUSIC as a function of SNR, N, and in the presence of phase noise.

3.5 Main Findings

We have presented an algorithm for 2D-DoA estimation with 3D L-shaped arrays, considering a system model that comprises the hardware impairments described in Chapter 2. The proposed estimation algorithm is simple and compensates the CFOs via differential signal combining. The performance of the algorithm has been studied via simulations for several system configurations and parameter setups. Furthermore, a comparison with the well-known root-MUSIC algorithm is performed. The results show that the estimator is robust for a wide range of angles and SNRs, and it performs as well as root-MUSIC in the case of single source. The higher complexity of the root-MUSIC is due to its capability to identify more than one source. More precisely, it can be solved up to $M-1$ uncorrelated sources, where M is the number of antenna elements. When more than one source is present, the

proposed method fails. However, when a single source case is considered, the proposed method is preferable due to its lower complexity than the root-MUSIC.

Spatial and temporal averaging increases the noise immunity of the proposed algorithm. However, while spatial averaging is always beneficial, the temporal averaging window length has to be selected according to the operating SNR in the presence of distinct CFOs between the RF receivers of distinct antenna elements.

The effects of DC offset and PN are also considered. It is shown that DC offset determines an error floor in the RMSE curves. Finally, it is shown that a PO calibration can be done using a local reference signal. It is beneficial to compensate the phase differences of the LOs that comprise a contribution due to the slowly time variant PN process.

Chapter 4

WiPLi Lab Complete Testbed and Practical DoA Estimation Results

In this chapter, a wireless testbed with a multiple antenna receiver is presented. It is composed by a single transmitter, a rotating four antenna array connected to the quad radio frequency (RF) front-end (FE) described in Chapter 2, as well as the eight channel acquisition board, and a control PC that manages all the devices. The algorithms can be implemented directly on the field programmable gate array (FPGA), but they can also be tested in a simulation environment, e.g., *Matlab*, since the acquired data can be transfered from the board memory to the PC. Moreover, the algorithm implementation on the FPGA can be done by exploiting the *System Generator for DSP* Xilinx tool that allows the algorithm synthesis from a *Simulink* block diagram. All these features make the testbed a useful tool for rapid prototyping and testing. In particular, the presence of the rotating antenna array allows the experimental analysis of the direction of arrival (DoA) estimation techniques. In this respect, several experimental measurements have been done, and we show that the results obtained with the algorithm presented in Chapter 3 for the 1D-DoA estimation case, are in good agreement with the simulations, also when the effect of non isotropic antenna gains and/or different temporally correlated phase noises (PNs) of not co-phased RF FEs becomes considerable.

4.1 Introduction

As already described in Chapter 1, the presence of an antenna array at the receiver can be used to exploit the directionality properties of the channel in order to provide spatial diversity, beamforming capabilities, and/or to implement angle of arrival (AoA) estimation based positioning systems [44]. All these possibilities have been investigated theoretically and via simulations in the past, showing their benefits under ideal conditions. However, hardware platforms do not always exhibit such behaviour. In fact, there are many implementation

non idealities that can affect the system performance. To this end, hardware platforms and testbeds are essential in validating algorithms.

Wireless testbeds and prototyping play an important role in both academia and industry. As explained above, they give greater insight into wireless system design, and they provide hands-on experiences to students and faculty [45]. Furthermore, it is important to have reliable information about future designs and developments, especially in a very competitive market such as the telecommunications [46].

As explained in [47], hardware implementations can be divided into three groups: *demonstrators*, that serve to show an existing technology to customers; *testbeds*, that are generally used for research; *prototypes*, that are the initial realization of a research idea. In this paper we concentrate in testbeds. According to the definition in [47], a testbed allows real-time experiment, even if the signal processing may be performed off-line.

Various testbeds have been constructed for testing new wireless technologies, in particular for multiple-input multiple-output (MIMO) systems [48]. They are complete out-of-the box testbeds, e.g., available from Lyrtech [27], Signalion [49] or others, or assembled commercial off-the-shelf components. Several classifications have been suggested, according to different selection criteria. One of these can be the final purpose, i.e., if the testbed is developed to study a specific standard [50] or for general purpose [51]. Another classification criteria may be the used technology, e.g., software-defined [52], DSP-based [53], FPGA-based [54], etc. Alternatively, flexibility, development time consumption, throughput or cost, and the educational possibilities are other possible classification criteria.

4.1.1 Previous Works

We now describe some testbed examples that can be found in the literature. In [50], a 4×4 FPGA-based wireless testbed for long term evolution (LTE) applications was assembled by using two off-the-shelf main boards. They are equipped with Altera Stratix II FPGA. These main boards are capable of controlling up to 4 RF FEs each one. The RF FEs are based on the integrated circuit (IC) MAX2829 from Maxim that is herein set up in the frequency range from 2.4 to 2.5 GHz and allows for using up to 40 MHz of bandwidth. Furthermore, this testbed can store up to 15.7 ms using 12 bit in-phase and in-quadrature (I&Q) data, so it is adequate for testing short burst transmission.

An example of a testbed designed for general purpose can instead be found in [51]. It was developed to examine MIMO algorithms and channel models, in a maximum of 20 MHz bandwidth around the 2.45 GHz frequency. A particular feature of this testbed is the possibility to variate the antenna distances, allowing for studying the channel capacity as a function of the spatial correlation [55]. To the best of our knowledge, DoA experiments have not been conducted with this testbed.

A low cost 4×4 software-defined system testbed was presented in [56]. Herein, the

MAX2829 evaluation kit from Maxim is incorporated in the testbed design. The digital back-end consists of the ICS-660B digital-to-analog converter (DAC) and the ICS-645B analog-to-digital converter (ADC). They are installed in the *peripheral component interconnect* (PCI) slots of a control PC and exploit this bus to transfer data into the Matlab environment for the off-line signal processing. Since the RF FE is the same as in [50], this testbed has the same bandwidth and frequency constraints. Differently to the other platforms, in [56] the testbed was used to conduct DoA experiments. In this respect, a two element uniform linear array (ULA) of patch antennas was used, and few indoor measurements were conducted. In this case, the calibration of the phase offsets (POs) between the receivers was addressed by using an RF switch board that injects a common RF signal to both the receivers. This is one of the simplest calibration technique, as explained in [35]. Nonetheless, the lack of a rotating support yields these kind of experiments cumbersome and non systematic. Other examples of MIMO wireless testbed can be found in [57, 58].

4.1.2 Contributions

Motivated by these considerations, we have assembled our own testbed, called *WiPLi Lab Wireless Testbed*, that we describe in this chapter. It resembles the abovementioned examples, and in particular [51] and [56] where a Matlab interface improves flexibility and allows a multitude of experiments with different constraints. We extend the antenna capabilities of the testbed in [56] by increasing the number of antennas to 4 at the expense of a bandwidth reduction. This testbed has been used to compare simulation and experimental DoA estimation results. In particular, we have considered the 1D-DoA estimator described in Chapter 3, and we have shown that numerical results are in good agreement with measurements, especially when the effect of non isotropic antenna gains, and/or different temporally correlated PNs of not co-phased RF FEs becomes considerable.

This chapter is organized as follows. In Section 4.2, the testbed description is provided, giving particular emphasis to bandwidth constraints and rapid prorotyping capabilities. In Section 4.3, the DoA estimation experimental results are reported and commented. Finally, main finding follow.

4.2 Testbed Description

A block diagram of the WiPLi Lab wireless testbed is depicted in Fig. 4.1. As it can be observed, it is composed by several main blocks, listed as follows.

- A vector signal generator, Agilent $E8267D$, used as transmitter;
- a rotating board with a four antenna array;
- four direct-conversion RF FEs;

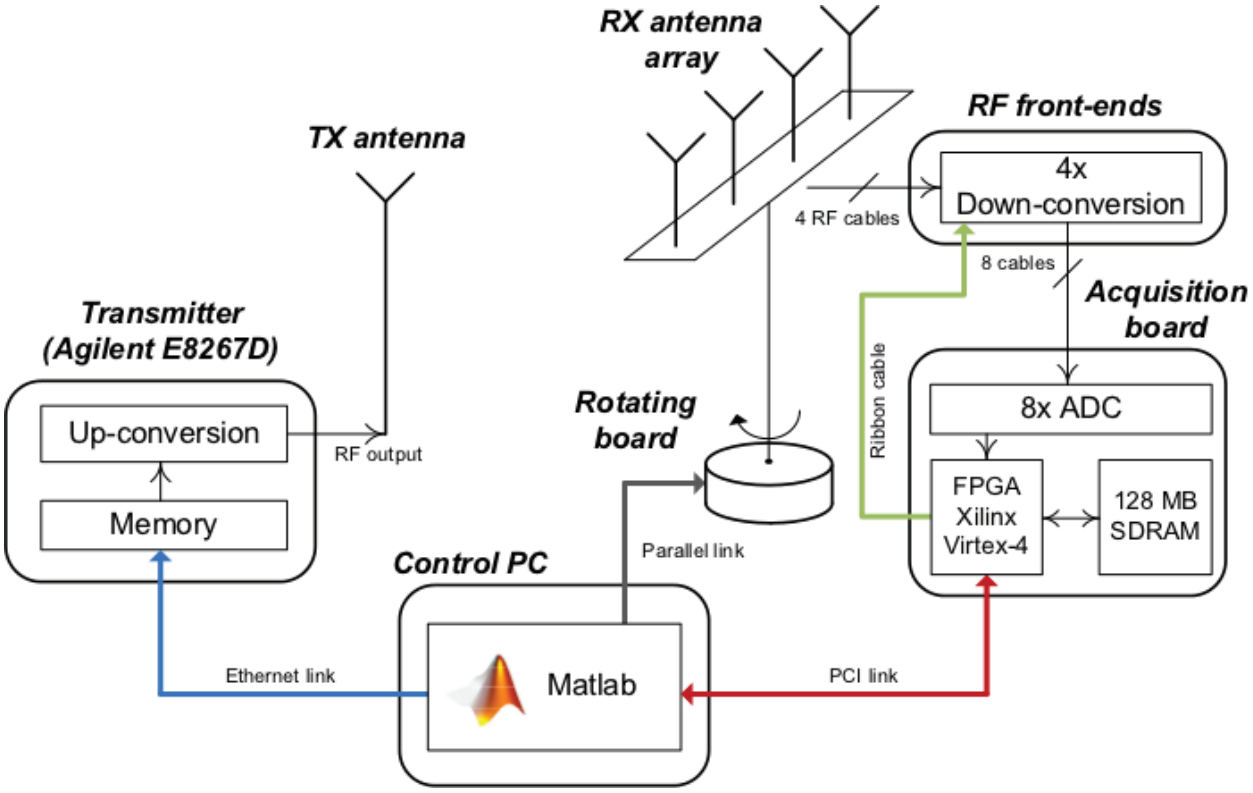

Figure 4.1: WiPLi Lab wireless testbed.

- an eight channel acquisition board provided with a Xilinx Virtex 4 FPGA and a 128 Mega byte (MB) of memory;
- a control PC for the devices management and the post-processing.

All these devices will be separately analyzed in order to highlight the main features.

4.2.1 Transmitter

The Agilent E8267D is a vector signal generator [59] that can work in the frequency range from 250 kHz to 20 GHz. It is able to generate a wide range of modulated signals, both analog - amplitude, frequency, and phase modulations (AM, FM, PM) - and digital - amplitude, frequency, phase shift keying modulations (ASK, FSK, PSK), and quadrature amplitude modulation (QAM). Furthermore, it can be used to create multi-tone signals and also to generate arbitrary waveforms. All these signals are generated with an internal baseband generator that has a maximum bandwidth of 40 MHz. After, these signals can be up-converted and amplified up to about 16 dBm of power.

In the WiPLi Lab testbed, this device is used as transmitter. It is connected via Ethernet link to the control PC, from which it can be properly set up from the Matlab environment through the *application programming interface* (API) functions provided by Agilent. Moreover, a specific waveform can be uploaded, if needed. The memory of the instrument accepts

waveforms that occupy up to a maximum of 8 Mega samples (MS), that correspond to approximately 200 ms. Finally, an external clock input and an external trigger input are available.

The RF output of the signal generator is connected to a dual band microstrip antenna tuned to both the 2.4 GHz and the 5.8 GHz bands.

4.2.2 Rotating Antenna Array and RF Front-Ends

The receiver is firstly composed by a four antenna array, mounted on a rotating board. This can be controlled via the parallel port of the control PC, and has a 2.5 deg of angular resolution.

The antenna array is a linearly equispaced (LES) array with interelement distance $d = 6.2$ cm, i.e., $d = \frac{\lambda}{2}$ when the carrier frequency is 2.412 GHz.

The antennas of the array are connected to the inputs of the RF multiple antenna FE, shown in Fig. 2.3 and characterized in Chapter 2. The receivers can be used both in the 2.4 and 5.8 GHz bands. However, for what the DoA estimation experiments concern, they are used only in the 2.4 GHz band since the antenna array is $\frac{\lambda}{2}$-spaced at this frequency.

All the FE parameters are controlled through API functions, in particular the gain and the bandwidth.

4.2.3 Acquisition Board

The acquisition board is the Lyrtech VHS-ADC shown in Fig. 2.1.

Maximum Write Speed Constraint

This board, as explained in Chapter 2, is equipped with a Xilinx Virtex-4 FPGA, and two SDRAM banks each with 64 MB of memory. Data are stored with 16 bit precision, allowing the capacity of the memory for recording up to 64 MS. The limited write speed of the memory introduces a constraint in the acquisition rate. In fact, in order to correctly record the data samples, the maximum write rate of the memory, R_{mem} that corresponds to 225 MS/s, must be larger than the total data rate, $R_{data} = F_s \times N_{ch}$, where F_s is the sampling frequency, and N_{ch} is the number of channels. This allows for a maximum sampling frequency of 26 MHz when the whole antenna array is used. Obviously, this limits the FE bandwidth in turn.

It should be noted that the API function that allows for acquiring the data samples, provided by Lyrtech, uses a fixed clock at 104 MHz. Hence, if we want to modify the data rate we have to downsample the data, even if this limits the sampling frequency to values obtained by dividing to two, i.e., 52 MHz, 26 MHz, etc. Alternatively, if a different sampling frequency is required, an external clock can be used.

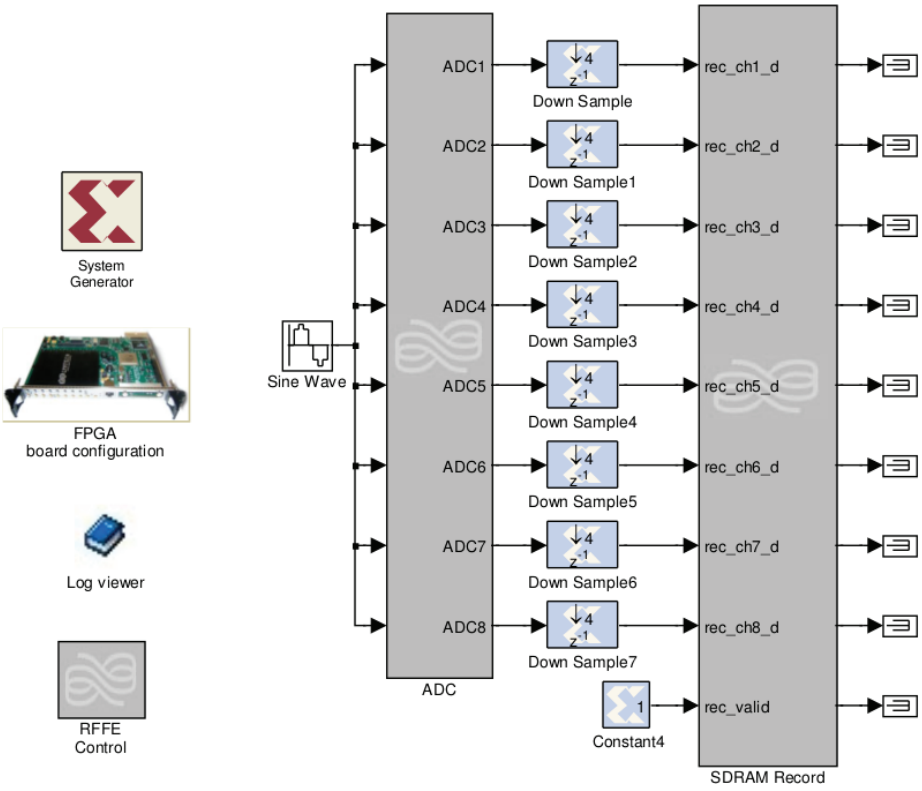

Figure 4.2: System Generator for DSP/simulink design for the off-line processing.

After having stored the data samples, a PCI bus is used to transfer them to the control PC. This yields the data available for the post-processing into the Matlab environment.

Rapid Prototyping with System Generator for DSP

Since data must be written into the acquisition board memory before being available for the off-line post-processing, a minimum *very high-level design language* (VHDL) project has to be preliminary developed in order to instantiate at least the ADC and the memory interfaces. This bitstream can be developed directly in VHDL code. Alternatively, it can also be synthesized by using a Xilinx tool, the System Generator for DSP, that allows for developing a project in the Simulink environment. In this way, it is possible to develop a specific application at a system block level by using the block libraries provided by Xilinx. In fact, portions of VHDL code are synthesized when a specific block, e.g., the ADC interface, or a complex multiplier, etc., is included into the project.

It should be noted that, if we develop the complete receiver algorithm into the FPGA, this is executed real-time. However, even if the System Generator for DSP is a useful tool for rapid prorotyping, the development of an application takes a long time. As explained before, we can use the acquisition board only to record the ADC samples and to transfer them into the Matlab environment. To do so, a minimum System Generator for DSP project has to be developed, and it is shown in Fig. 4.2.

As it can be observed, this design includes an eight channel ADC block, 8 downsample

blocks, and a memory block. The sampled data are acquired at the maximum sampling rate, i.e., 104 MHz, but they are downsampled with a factor 4. Finally they are recorded into the memory. It should be noted that the effective total data rate is $R_{data} = 208$ MS/s, so the memory write constraint is respected.

On the left hand side of Fig. 4.2, there are other blocks that are used to set the FPGA parameters (FPGA model, clock frequency, etc.). Particularly, the *RFFE Control* block instantiates the interfaces that allow us to change the RF FE parameters.

4.2.4 Control PC

The control PC manages all the system devices through the Matlab environment. Furthermore, we can prepare off-line data that have to be transmitted, and then process the received samples.

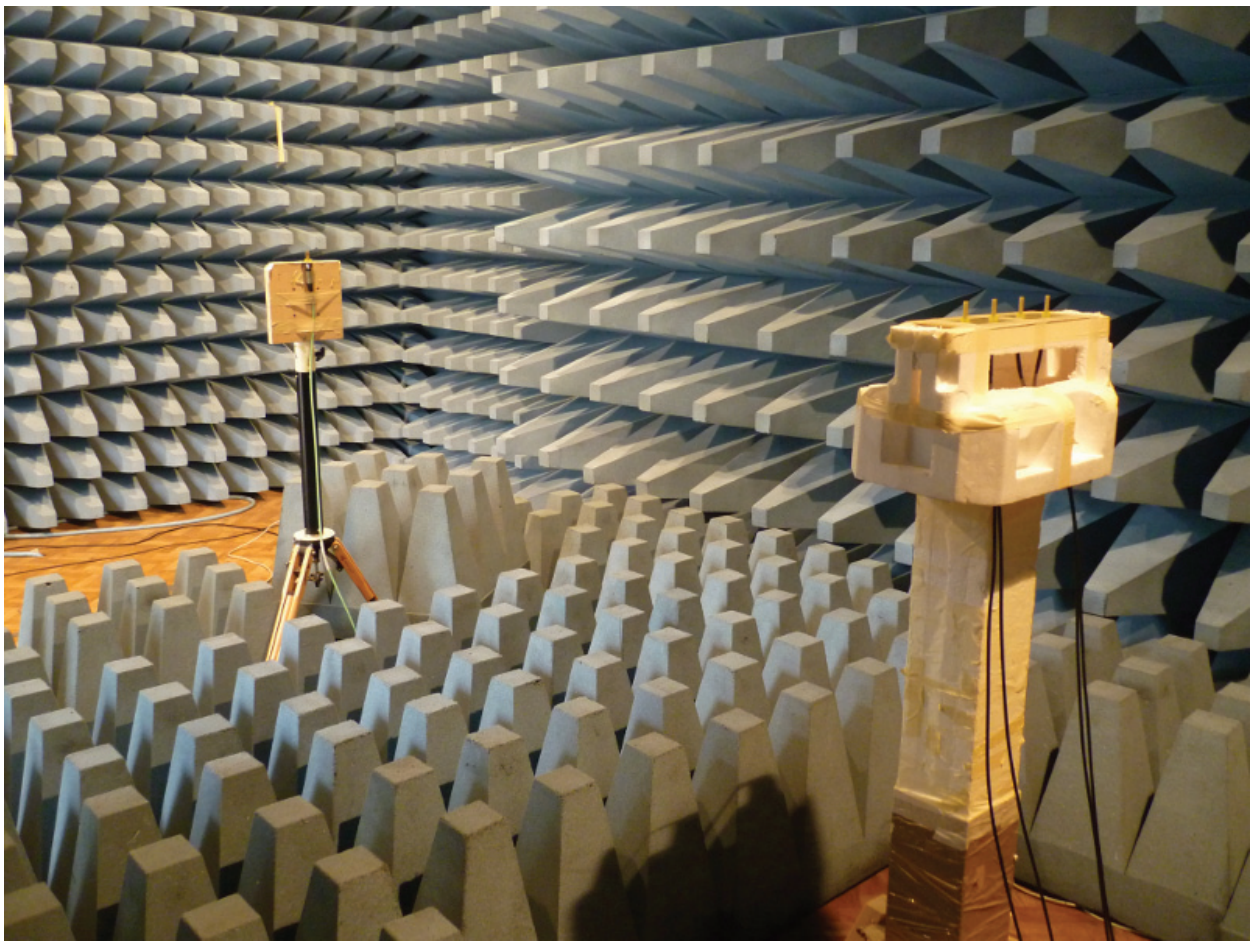

Figure 4.3: Transmitter antenna and receiver antenna array into the anechoic chamber.

4.3 DoA Estimation

In this section we present several DoA estimation results obtained by using the WiPLi Lab testbed in an anechoic chamber (Fig. 4.3). The considered testbed parameters are: BW= 7.5 MHz, high gain mode with gain setting (GS) 17 (corresponds to a gain of 67 dB), transmitted power from -37.5 to -2.5 dBm that give SNRs from -7 to 28 dB, transmitter-receiver distance of about 1.5 m.

4.3.1 Experimental Results

We have conducted two experiments in order to show the performance first as function of the AoA ϕ_0, and then as function of the SNR. However, w.r.t. the first experiment, the accuracy of the rotating board is 2.5 deg, so the performance can be compromised by this factor giving a bias in the error. Hence, in order to study this kind of performance, we show the standard deviation of the error that can be approximated as

$$\sigma_e \approx \sqrt{\frac{1}{N_{it}} \sum_{k=1}^{N_{it}} (e_k - \mu_e)^2}, \tag{4.1}$$

where $e_k = \phi_0 - \hat{\phi}_{0,k}$, while $\mu_e = \frac{1}{N_{it}} \sum_{k=1}^{N_{it}} e_k$ represents the approximated mean value of the error.

Performance as a function of the AoA

In Fig. 4.4 and 4.5 we show the performance results of the considered estimator in terms of standard deviation of the error as function of the AoA ϕ_0 and the number of samples N, with SNR= 3 dB and SNR=13 dB, respectively. We can observe that the measurement results are in good agreement with the simulation results, at least in the angle range $-45, 45$ deg. The deviation of the experimental results from the simulated results when the DoA is out of this angle range can be simply justified by the fact that the antenna array elements have not the same gain as function of the DoA, as it can be observed from Fig. 4.6. When the DoA exceeds ± 45 deg, the antenna gain for each element decreases, so the effective SNR decreases in turn and, consequently, the performance degrades.

Performance as a function of the SNR

In the second experiment we consider the performance of the algorithm in terms of RMSE as function of the SNR. In order to avoid the problems due to the rotating board accuracy, we have considered only two test DoAs, $\phi_0 = \{0, 30\}$ deg, that have been obtained by orientating the receiver antenna array manually. The performance result is show in Fig. 4.7 for $\phi_0 = 0$ deg, and in Fig. 4.8 for $\phi_0 = 30$ deg. Particularly, simulation results are obtained in an ideal

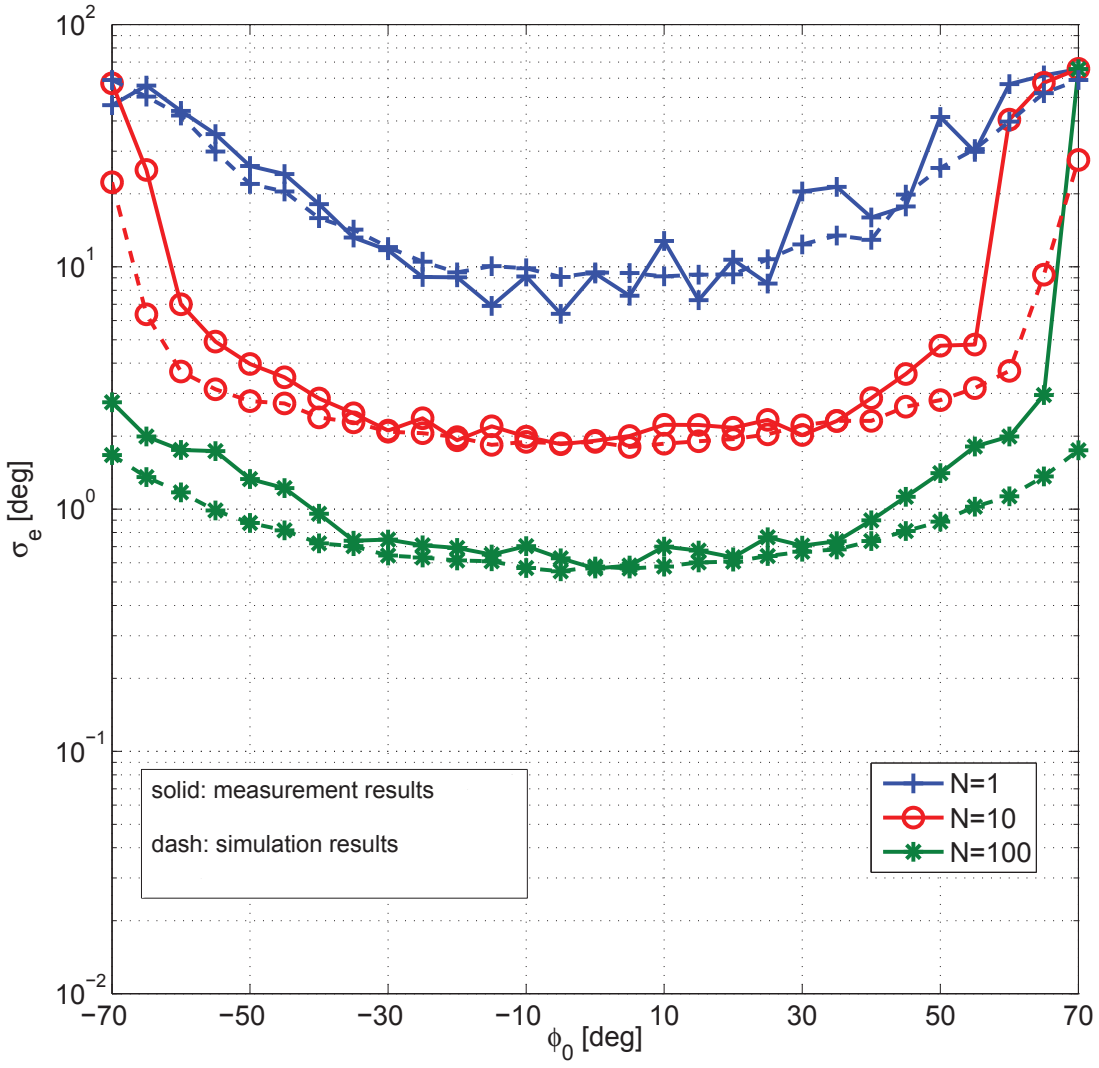

Figure 4.4: Standard deviation of the error as function of the AoA ϕ_0, with SNR= 3 dB.

case, i.e., without hardware impairments, and with the hardware impairments described in Chapter 2, even if we have generated the PN with the temporal correlation in Fig. 2.13 sampled by a factor of two since here the sampling time is two times the sampling time used to conduct the measurements campaign. Even in this case, good agreement between simulation and experimental results can be seen. In particular, we can observe the presence of an error floor due to the correlated PN that is not compensated. Nevertheless, this error floor ensures 0.1 deg of RMSE.

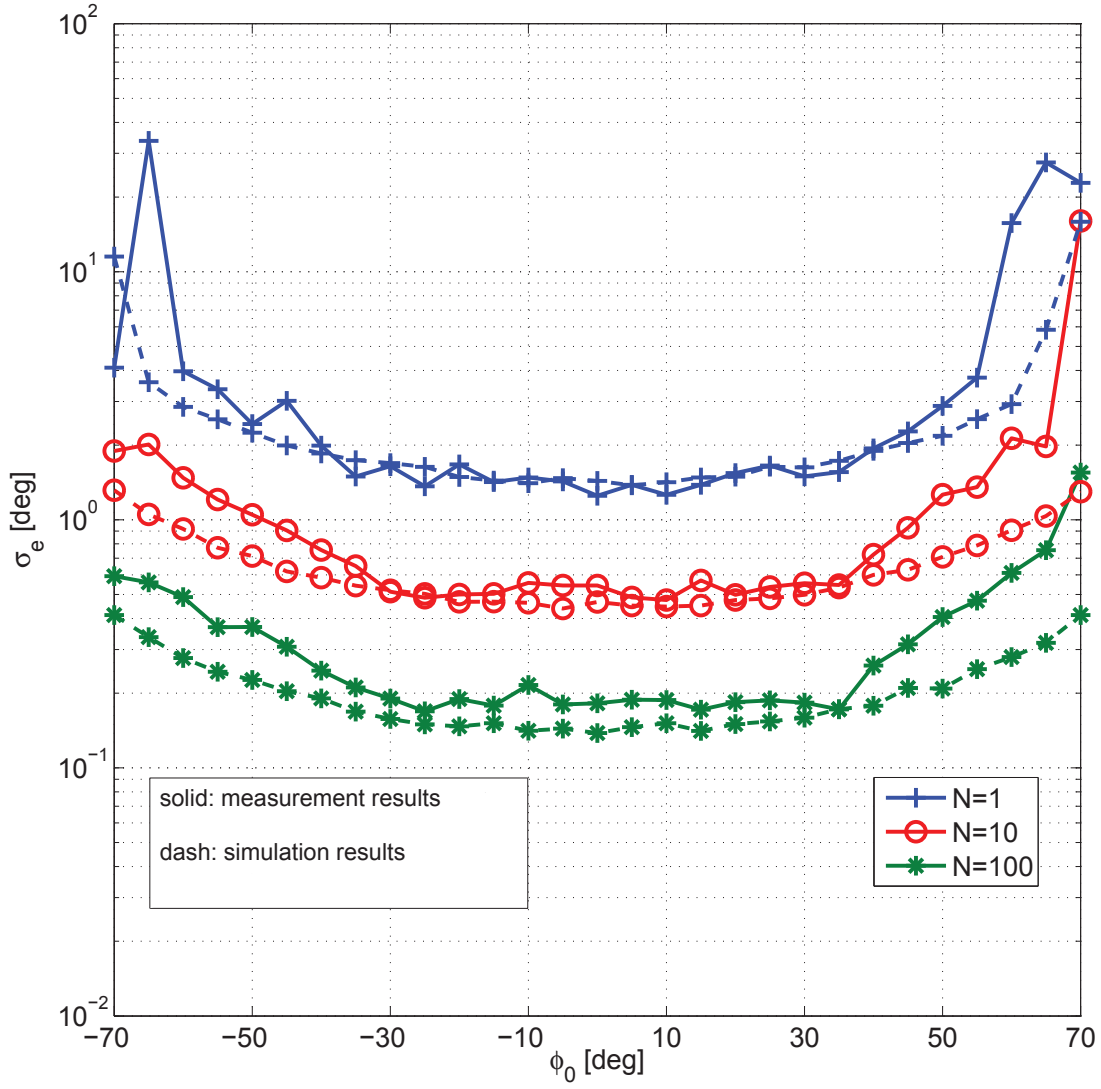

Figure 4.5: Standard deviation of the error as function of the AoA ϕ_0, with SNR= 13 dB.

4.4 Main Findings

We have described the WiPLi Lab wireless testbed assembled with commercial off-the-shelf components. In particular, it comprises a single transmitter, a rotating four antenna array connected to a quad RF FE, an eight channel acquisition board (to process four pairs of I&Q signals) provided with an FPGA, and a control PC that manages all the devices. We have described each component of the testbed. Furthermore, we have highlighted how the limited write rate of the memory constraints the maximum sampling rate, and the RF bandwidth in turn. Moreover, we have illustrated the basic System Generator for DSP design that can be used to record data into the memory, and to process them off-line. Finally, we have presented the experimental results of DoA estimation test that show good agreement with

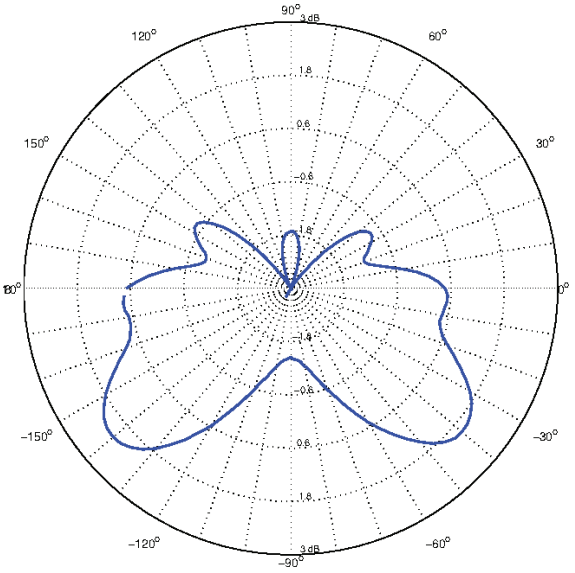

(a) Radiation diagram of Antenna 1.

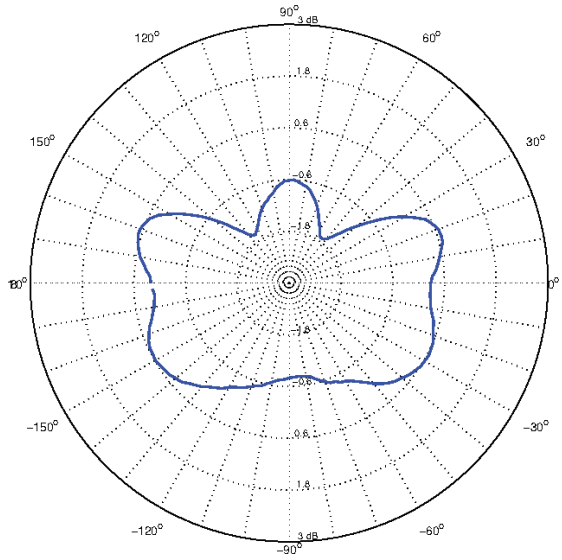

(b) Radiation diagram of Antenna 2.

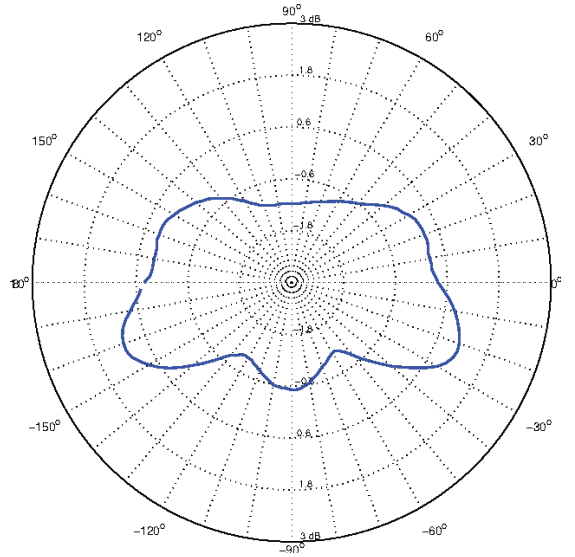

(c) Radiation diagram of Antenna 3.

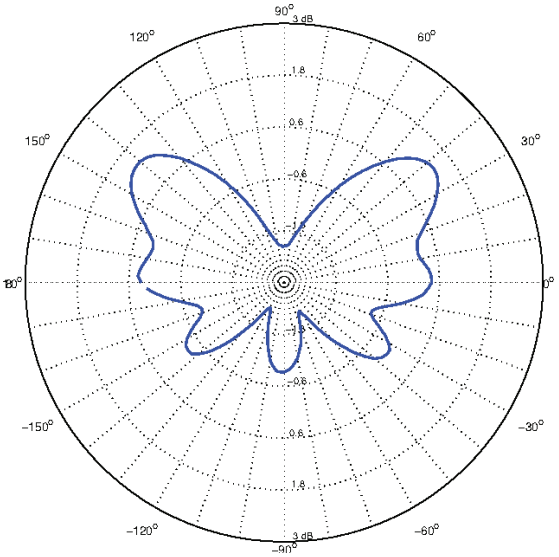

(d) Radiation diagram of Antenna 4.

Figure 4.6: Radiation patterns of the array elements.

simulations. These results have shown both the effect of the non isotropic antenna gain, and different temporally correlated PN of not co-phased RF FEs.

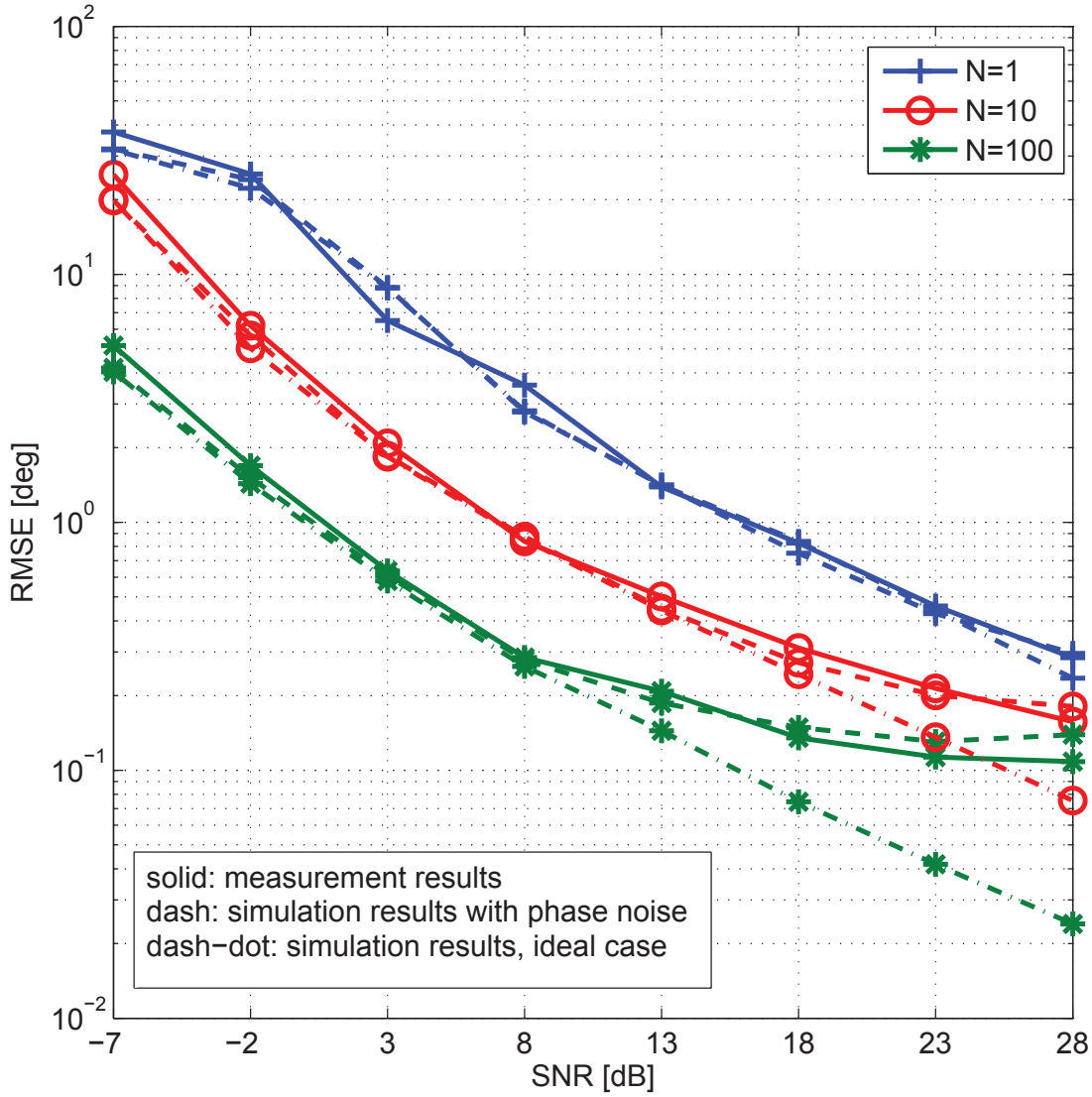

Figure 4.7: RMSE as function of the SNR, with $\phi_0 = 0$ deg.

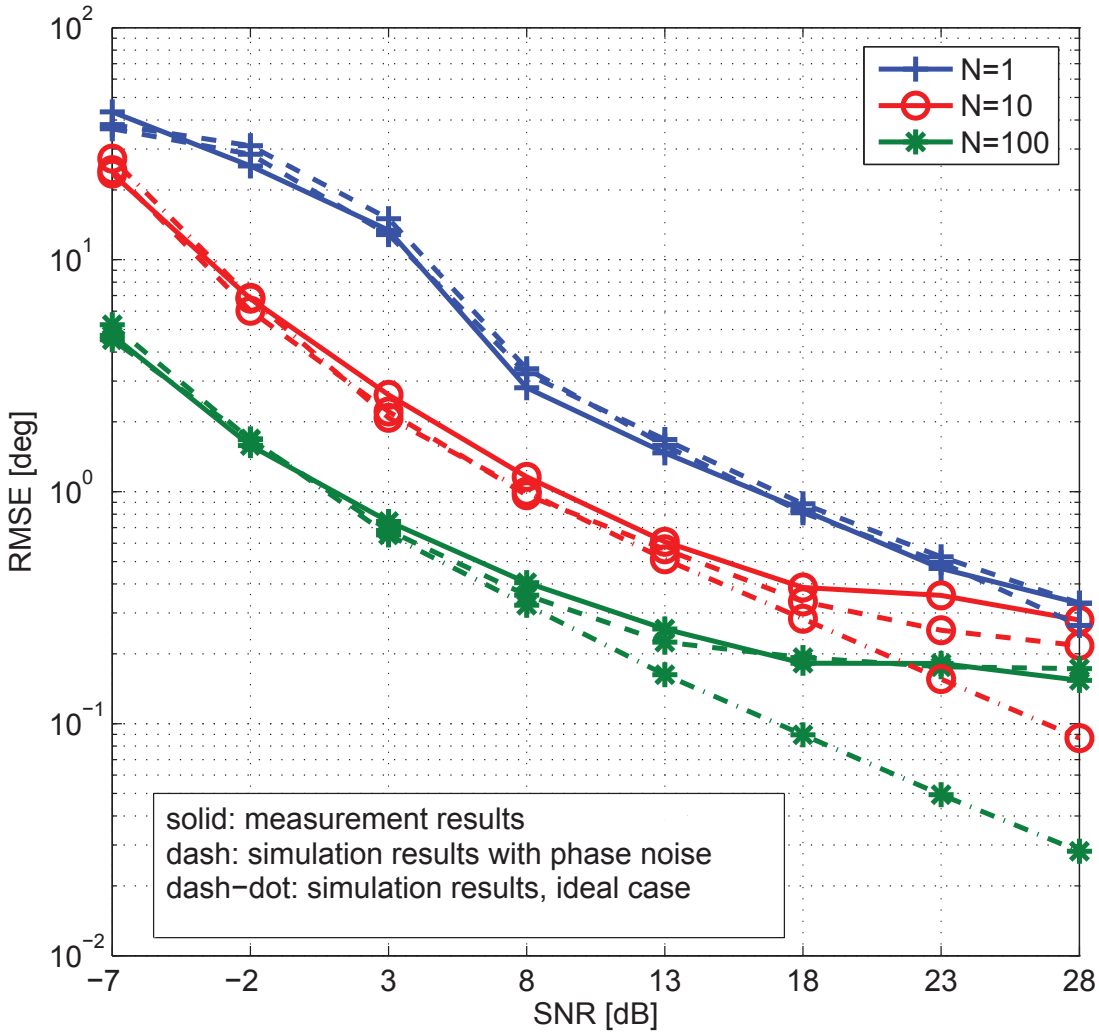

Figure 4.8: RMSE as function of the SNR, with $\phi_0 = 30$ deg

Chapter 5

Phase Offsets Calibration in DoA Estimation

In the previous chapters, the effect of the hardware impairments on direction of arrival (DoA) estimation has been shown. The algorithm that has been derived relies on a reference signal (from known direction, or locally generated) to perform a pre-calibration of the different phase offsets (POs). This chapter addresses the problem of the compensation of different POs, that we call *array calibration*. In particular, we propose a novel method that consists in the use of a particular antenna array which comprises the elements for the DoA estimation and a common antenna which is shared with a splitter among the receivers. The signal that impinges on the common antenna is acquired by every receiver and allows the estimation of the phase ambiguity. After the calibration step is performed, analog switches select the array elements for the DoA estimation. A method which enables the phase ambiguity estimation is presented, and several simulated performance results are illustrated. Furthermore, we show the effect on calibration due to the presence of different carrier frequency offsets (CFOs) among the receivers, and we propose an approach for their compensation. The presence of phase noise (PN) is also considered, and its effect is analyzed.

5.1 Introduction

An important aspect in DoA estimation is the array calibration, as already highlighted in Chapter 3. In fact, phase mismatches among the sensors introduce ambiguities in the array manifold which may result in poor DoA estimation. These mismatches are caused by the fact that each receiver consists of a different integrated circuit (IC) that manifests, for instance, its own PO (since the radio frequency (RF) local oscillator (LO) is internally implemented). The compensation of these impairments is typically done with the aid of an auxiliary reference signal. The array pre-calibration in [35] and [60] is done with the injection (directly to the receiver inputs and by using couplers, respectively) of a local reference signal, which requires an additional RF oscillator. In [61] and [62], instead, the presence of a reference signal from a known direction is exploited. In particular, in [61] three calibration methods are

proposed and compared, while in [62], the signal energy knowledge is used to estimate the amplitude and phase errors directly from the signal covariance matrix, without implementing an eigen-decomposition.

Other approaches that do not require any auxiliary sources can also be found in the literature. The method in [36] realizes array phase calibration under the assumption of a large number of sensors, which is not always realistic. The signal correlation matrix structure is exploited in [37] to compensate the gain and phase differences among sensors. However, the correlation matrix estimation and its several elaborations imply high complexity. A particular application of the signal subspace method, combined with a QR-based Gauss-Newton algorithm, works well only for small phase, gain, and sensor locations perturbations, as shown in [63]. Even in this case the computational complexity is high. A genetic approach is exploited instead in [64] for array gain and phase calibration. More recently, the instrumental sensors method (ISM) has been derived in [65], while the approach based on the combination of ISM and the estimation signal parameter via a rotational invariant technique (ESPRIT) has been proposed in [66]. The latter requires the use of two well calibrated receiver paths, i.e., from the antenna to the baseband output, in order to estimate the phase and gain uncertainties through eigendecomposition. In [67], a blind calibration algorithm based on the independent component analysis (ICA) is presented. The ICA technique is used to resolve the presence of multiple sources in order to produce a set of reference data that can be exploited to iteratively obtain the calibration matrix. Hovewer, the ICA needs the received signals to be independent and non-Gaussian. The method involves an eigendecomposition which increases complexity.

In this chapter, we consider the problem of array calibration when frequency and phase mismatches occur. In particular, we propose a novel calibration technique which relies on a particular array configuration. Furthermore, we derive a simple method for the phase difference estimation (based on a signal correlation) that can be used with the DoA estimator described in Chapter 3. We show how CFOs can degrade the phase estimation. A compensation algorithm is proposed in order to mitigate this degradation. Finally, we analyze the performance of the proposed method in the presence of PN. As it will be shown, the calibration procedure does not depend on the specific transmitted signal and it works for a dispersive channel as well.

Our method requires the use of only one additional antenna element that is shared with a splitter among the receivers. This yields a simpler architecture compared to the approach in [66] that requires two well calibrated receiver paths, or to the method in [35] that requires an auxiliary RF LO. As it will be explained in the following, calibration is achieved via a signal correlation operation and not via any eigenvalue decomposition which is more complex. In this way, the CFO contributions are well compensated since their differences are limited, as measured in Chapter 2.

This chapter is organized as follows. In Section 5.2, we describe the DoA estimation

system model. In Section 5.3, the proposed calibration procedure is explained, as well as the derivation of the methods which allow the phase and frequency ambiguities estimation and compensation. Some practical considerations are discussed in Section 5.4. We study the mean-square-error performance of the parameter estimation in Section 5.5.

5.2 DoA Estimation System Model

Let us assume a radio system as described in Chapter 1, and we extend it to the case of a generic single-input-multiple-output (SIMO) propagation channel whose baseband impulse response can be expressed as [68]

$$h^{(i)}(t) = \sum_{l=0}^{L-1} \alpha_l \delta(t-\tau_l) e^{-j\left(\psi_l^{(i)} + 2\pi f_{0,RF}\tau_l\right)}, \tag{5.1}$$

where $i \in \{1,..,M\}$ is the antenna index, α_l represents the complex amplitude of the l-th ray, τ_l is its delay, and $\psi_l^{(i)}$ is a phase contribution due to the 1D-DoA. We also consider a direct conversion receiver architecture as described in Chapter 2. If we sample the baseband signals with period T, the sequence of complex samples $x^{(i)}(nT)$ associated to the i-th sensor can be written as

$$\begin{aligned} x^{(i)}(nT) = &\sum_{l=0}^{L-1} \alpha_l s(nT-\tau_l) e^{-j2\pi f_{0,RF}\tau_l} \\ &\times e^{j\left(\beta^{(i)}(nT) - \psi_l^{(i)}\right)} + w^{(i)}(nT), \end{aligned} \tag{5.2}$$

where $\beta^{(i)}(nT)$ includes the phase uncertaintes due to the CFO $f^{(i)}$, the PN process $\varphi^{(i)}(nT)$, and the PO $\Phi^{(i)}$. For the sensor i, it is expressed as

$$\beta^{(i)}(nT) = 2\pi f^{(i)} nT + \varphi^{(i)}(nT) + \Phi^{(i)}. \tag{5.3}$$

We assume that the complex gain α_l is due to the propagation loss. Finally, $w^{(i)}(nT)$ is the background noise contribution.

As widely explained in Chapter 3, the presence of the phase term $\beta^{(i)}(nT)$ makes the DoA estimation challenging. In fact, without loss of generality, if a linearly equispaced (LES) antenna array is considered and a channel model with a single line-of-sight (LOS) path, i.e., $L = 1$ and $\alpha_1 = 1$ is assumed, we can write (3.3) in matrix form as in (1.7), where the array manifold includes the non idealities and, at the instant nT, reads

$$\begin{aligned} \mathbf{a}(\phi) = [&e^{j\beta^{(1)}(nT)}, e^{j2\pi\frac{d}{\lambda_0}\cos(\phi)+j\beta^{(2)}(nT)}, .. \\ &.., e^{j2\pi\frac{d}{\lambda_0}(M-1)\cos(\phi)+j\beta^{(M)}(nT)}]^T. \end{aligned} \tag{5.4}$$

This representation does not have the familiar Vandermonde structure due to the presence of the phase ambiguity $\beta^{(i)}(nT),\ i \in \{1,..,M\}$. Therefore, the term $\beta^{(i)}(nT)$ has to be estimated and compensated to calibrate the array manifold. This procedure is not feasible from (3.3) since neither the channel nor the DoA is known.

The array calibration method that we propose is based on a particular array configuration that requires the use of an additional antenna element that is shared by all the receivers and it acts as a reference. In this way, the DoA is forced to be $\phi = 0$ and the array manifold reads

$$\mathbf{a}(0) = [e^{j\beta^{(1)}(nT)}, e^{j\beta^{(2)}(nT)}, .., e^{j\beta^{(M)}(nT)}]^T. \tag{5.5}$$

Thus, we are able to estimate the array manifold non idealities at least within an arbitrary rotation factor, also when multipath (MP) propagation occurs. This is because the shape of the reference signal is not important to obtain the phase $\phi = 0$ but it is only important that the same signal is aquired by all the receivers. Although in this chapter we develop a low complexity compensator for the uncertainties $\beta^{(i)}(nT) - \beta^{(i+1)}(nT),\ i \in \{1,..,M-1\}$ so that it can be used by the DoA estimator presented in Chapter 3, and eventually the proposed array configuration can be used together with other DoA algorithms and other array geometries.

5.3 Calibration Method Description

The calibration technique that we now describe does not rely on the knowledge of the transmitted signal and is also independent of the channel and the DoA. It requires the use of a particular antenna array as shown in Fig. 5.1. Each receiver is connected to an analog switch that can alternatively select the sensor for the DoA estimation or the common sensor that is shared with a splitter among the receivers. It follows that the calibration step and the DoA estimaton step are time multiplexed.

In this way, the resulting channel impulse response (CIR) when the switches select the common antenna becomes

$$h_C(t) = \sum_{l=0}^{L-1} \hat{\alpha}_l \delta(t - \hat{\tau}_l) e^{-j2\pi f_{0,RF}\hat{\tau}_l}, \tag{5.6}$$

where $\hat{\alpha}_l$ and $\hat{\tau}_l$ are the complex amplitude and the propagation delay, respectively, for the l-th tap of the channel from the transmitter to the common antenna. The i-th acquired calibration signal reads

$$\begin{aligned} x_C^{(i)}(nT) = A(nT)e^{j\left(2\pi f^{(i)}nT + \varphi^{(i)}(nT) + \Phi^{(i)}\right)} \\ + w^{(i)}(nT),\ i \in \{1,..,M\}, \end{aligned} \tag{5.7}$$

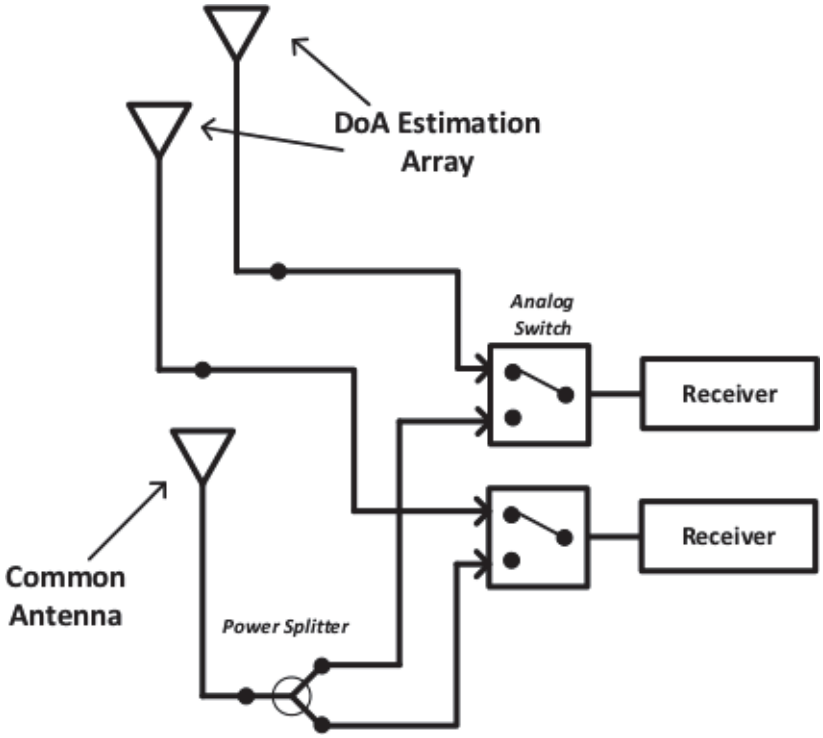

Figure 5.1: Example of a two element antenna array which can be used to implement our calibration method.

where

$$A(nT) = \sum_{l=0}^{L-1} \hat{\alpha}_l s(nT - \hat{\tau}_l) e^{j2\pi f_{0,RF} \hat{\tau}_l}. \tag{5.8}$$

As it can be observed, the calibration signal $x_C^{(i)}(nT)$ does not depend on the DoA.

5.3.1 Frequency and Phase Offset Calibration

From (5.7), we can not directly estimate the PO $\Phi^{(i)}$ because of the presence of both the complex channel contribution $A(nT)$ and the CFO. To proceed, we propose to correlate the antenna signals as follows

$$\begin{aligned} \Lambda^{(i)}(nT) &= x_C^{(i)}(nT) \cdot x_C^{(i+1)^*}(nT) \\ &= |A(nT)|^2 e^{j\left(2\pi\Delta f^{(i)} nT + \Delta\varphi^{(i)}(nT) + \Delta\Phi^{(i)}\right)} \\ &+ W^{(i)}(nT), \ i \in \{1, .., M-1\}, \end{aligned} \tag{5.9}$$

where $W^{(i)}(nT)$ is the resultant noise term, $\Delta f^{(i)} = f^{(i)} - f^{(i+1)}$, $\Delta\varphi^{(i)}(nT) = \varphi^{(i)}(nT) - \varphi^{(i+1)}(nT)$, and $\Delta\Phi^{(i)} = \Phi^{(i)} - \Phi^{(i+1)}$. It can be observed that the channel contribution appears as a real gain factor without contributing in the argument of the exponential. Furthermore, the PO term now appears as the difference of two absolute POs. This fact, however, does not affect the final DoA estimation since the DoA estimator that we herein implement uses the same correlation operation in (5.9) as it will be shown below. Thus, it

is also impaired by $\Delta\Phi^{(i)}$.

Now, the residual CFO $\Delta f^{(i)}$ is Gaussian with zero mean and standard deviation $\sqrt{2}\sigma_{CFO}$. Depending on whether the residual CFO $\Delta f^{(i)}$ is negligible or not, we propose two different estimators of $\Delta\Phi^{(i)}$.

Different Carrier Frequency Offset

The difference of the CFO $\Delta f^{(i)}$ among the antenna elements can be estimated as

$$\begin{aligned}&\Delta\hat{f}^{(i)}\\&= \frac{1}{2\pi N_{CFO}T}\sum_{n=0}^{N_{CFO}-1}\angle\left\{\Lambda^{(i)}\left(nT+T\right)\Lambda^{(i)^*}\left(nT\right)\right\},\\&i\in\{1,..,M-1\},\end{aligned} \tag{5.10}$$

where we have used N_{CFO} samples of the calibration signals in (5.7). It should be noted that since subsequent PN samples are highly correlated, we have that $\Delta\varphi^{(i)}(nT) \approx \Delta\varphi^{(i)}((n+1)T)$, so that the CFO estimate is not affected by the PN.

The CFO is compensated using (5.10). It follows that the instantaneous difference of the POs between the element pairs can be estimated as

$$\begin{aligned}\hat{\Delta\Phi}^{(i)} = \frac{1}{N_{AVG}}\sum_{n=0}^{N_{AVG}-1}\angle\left\{\Lambda^{(i)}(nT)e^{-j2\pi\Delta\hat{f}^{(i)}nT}\right\},\\i\in\{1,..,M-1\},\end{aligned} \tag{5.11}$$

where we have used N_{AVG} snapshots of the signal $\Lambda^{(i)}$. It should be noted that the PN affects the estimation of $\Delta\Phi^{(i)}(nT)$ through the term $\Delta\varphi^{(i)}(nT)$. If $N_{AVG}+N_{DOA}$ is not too large we have that $\Delta\varphi^{(i)}(nT) \approx \Delta\varphi^{(i)}((n+N_{AVG}+N_{DOA})T)$. In such a case the PN does not affect the estimation of $\Delta\Phi^{(i)}(nT)$.

In the following, we refer to $\hat{\Delta\Phi}^{(i)}$ simply as PO.

Equal Carrier Frequency Offset

If we can assume that the differences of the CFOs among the antennas are negligible, i.e., $\Delta f^{(i)} \approx 0,\ \forall i \in \{1,..,M-1\}$, the signal in (5.9) reads

$$\begin{aligned}\Lambda^{(i)}(nT) = |A(nT)|^2 e^{j\left(\Delta\varphi^{(i)}(nT)+\Delta\Phi^{(i)}\right)} + W^{(i)}(nT),\\i\in\{1,..,M-1\}.\end{aligned} \tag{5.12}$$

We can now estimate the POs between the element pairs simply as

$$\hat{\Delta\Phi}^{(i)} = \frac{1}{N_{AVG}} \sum_{n=0}^{N_{AVG}-1} \angle\{\Lambda^{(i)}(nT)\}, \quad i \in \{1, .., M-1\}, \tag{5.13}$$

without performing the CFO compensation as it is differently done in (5.11).

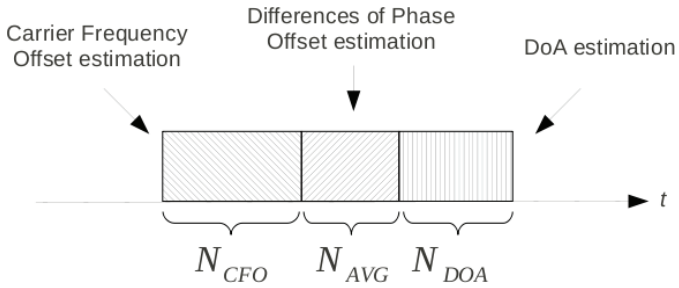

Figure 5.2: Temporal order of the calibration algorithm operations.

In summary, the calibration algorithm consists of the following steps (as also shown in Fig. 5.2):

- If we need to compensate the CFO, we acquire N_{CFO} samples of $x_C^{(i)}(nT)$ to firstly compute $\Lambda^{(i)}(nT)$ in (5.9) and then to estimate the CFO by using (5.10).
- We acquire N_{AVG} samples to estimate the PO $\Delta\Phi^{(i)}(nT)$. This procedure can be done with (5.13) if the CFO is negligible. Otherwise, the PO estimation is done with (5.11) which takes into account the compensation of the CFO.
- After the PO $\Delta\Phi^{(i)}(nT)$ compensation, we can estimate the DoA.

In Section 5.5, we compare the performance of the estimator (5.13) that does not compensate the CFO (in the following we denote it as method NOCOMP) with the performance of the estimator (5.11) that compensates the CFO (we denote it as method COMP).

5.4 Implementation Issues

The particular configuration of the array for the calibration requires further attention, particularly in reference to its practical implementation. In fact, as explained in Section 5.3, we have to connect the common antenna to every receiver's input (in particular to one input of the analog switch as in Fig. 5.1). This connection cannot be simply done with a short circuit because of the introduction of impedance mismatches into the signal path. Hence, it is necessary to use a multiport microwave power divider [69] which equally splits the input signal among the receivers and which must not introduce phase differences among the outputs.

It should be noted that since the signal that passes through the multiport power divider channels is the same, i.e., the RF signal at frequency $f_{0,RF}$, having paths with equal lengths guarantees the phase equalization among the multiport splitter paths. In this way, the calibration signal model in (5.7) holds true. Off the shelf devices are available for this purpose. Alternatively, a multiport splitter can be realized by using two output ports dividers and applying other dividers to those ports as shown in Fig. 5.3.

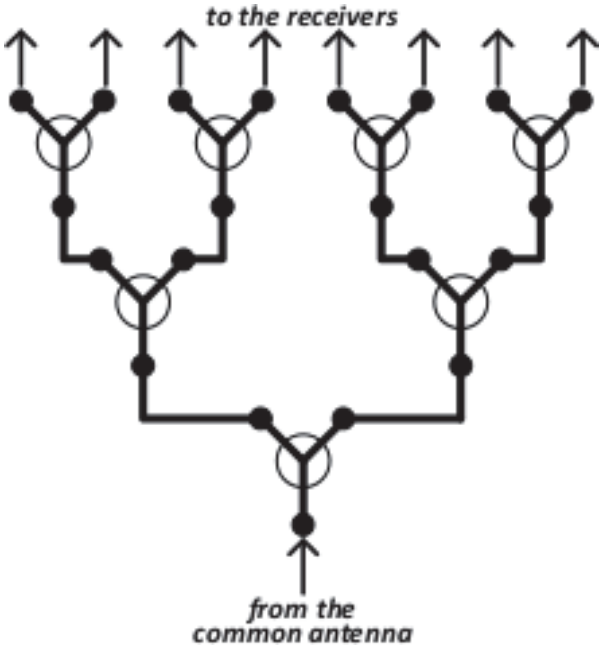

Figure 5.3: Example on how to realize a multiport splitter.

The proposed multiport splitter can be used with any number of array elements M. In fact, even if it has a total number of outputs which is a power of two, applying a 50Ω load into the unused port, the correct operation of the device is not affected.

Another important practical aspect concerns the length of the cables that connect the antennas of the DoA estimation array with the RF front-end (FE) inputs. In fact, the PO $\Phi^{(i)}$ in (5.3) does not include the phase differences among the channels due to different path/cable lengths. If the connection cables have different length, then the signal in (3.3) becomes

$$\begin{aligned} x^{(i)}(nT) = &\sum_{l=0}^{L-1} \alpha_l s(nT-\tau_l) e^{-j2\pi f_{0,RF}\tau_l} \\ &\times e^{j\left(\beta^{(i)}(nT)+\zeta^{(i)}-\psi_l^{(i)}\right)} + w^{(i)}(nT), \end{aligned} \tag{5.14}$$

where $\zeta^{(i)} = 2\pi f_{0,RF}\frac{\Delta^{(i)}}{c_0}$ is the phase contribution due to the propagation in the cable of length $\Delta^{(i)}$ (it should be noted that we have assumed $s(t-\tau_l-\frac{\Delta^{(i)}}{c_0}) \approx x(t-\tau_l)$ since the signal $s(t)$ is narrowband). Since the phase differences due to this impairment are time invariant, it is reasonable to assume an offline pre-calibration procedure that estimates $\zeta^{(i)}$.

Alternatively, an accurate path/cable length design that results in $\zeta^{(i)} = \zeta,\ \forall i \in \{1, .., M\}$ can also be done.

5.5 Performance Analysis

This section reports the performance analysis of the proposed calibration method. In particular, we analyze the *root mean-squared error* (RMSE) in the estimation of the PO $\Delta\Phi^{(i)}$ in (5.13) or in (5.11) defined as

$$\text{RMSE} = \sqrt{E\left\{\left|\frac{1}{M-1}\sum_{i=1}^{M-1}\Delta\Phi^{(i)} - \hat{\Delta\Phi}^{(i)}\right|^2\right\}}, \tag{5.15}$$

and the aggregate RMSE of the DoA estimation, defined as

$$\text{RMSE}_{\text{DoA}} = \sqrt{E\left\{\left(\phi - \hat{\phi}\right)^2 + \left(\vartheta - \hat{\vartheta}\right)^2\right\}}, \tag{5.16}$$

where ϕ and $\hat{\phi}$ are the azimuth and its estimate, respectively, while ϑ and $\hat{\vartheta}$ are the elevation and its estimate, respectively (in the simulation we have used $\phi = 30°$ and $\vartheta = 50°$). The parameters of the DoA estimator used in the numerical examples are $f_{0,RF} = 5.8$ GHz, and $d = \frac{\lambda_0}{2}$. The total number of elements becomes $3M - 2 = 4$, where $M = 2$ is the number of elements per subarray. Finally, we assume $\frac{1}{T} = 50$ MHz.

As far as the channel model is concerned, we have considered two models: the first is a single tap LOS channel ($L = 1$) with deterministic amplitude, while the second model is a two rays channel ($L = 2$) with the second ray that exhibits temporally and spatially uncorrelated Rayleigh faded amplitude and uniform phase. We define the factor γ as the ratio between the power of the LOS tap, M_{LOS}, and the power of the second tap. Furthermore, we define the signal to noise ratio SNR as

$$\text{SNR} = \frac{M_{LOS}}{N_0}, \tag{5.17}$$

where we have considered a transmitted signal with unitary power, while N_0 is the variance of the background noise $w^{(i)}(nT)$ that we have considered equal for all receivers.

We have set the parameters of the CFO model according to Chapter 2. The CFO estimation with (5.10) has been done assuming $N_{CFO} = 1000$. Finally, the standard deviation of the PN is assumed $\sigma_{PN} = 1$ deg.

5.5.1 Theoretical Considerations

Carrier Frequency Offset Effects

When we consider the NOCOMP method but the frequency offset differences among the antennas are not negligible, (5.13) can be written as (neglecting the PN)

$$\begin{aligned}\hat{\Delta\Phi}^{(i)} &= \frac{1}{N_{AVG}} \sum_{n=0}^{N_{AVG}-1} \angle\Big\{|A(nT)|^2 e^{j\Delta\Phi^{(i)}} \\ &\times e^{j2\pi\Delta f^{(i)}nT} + W^{(i)}(nT)\Big\} \\ &\approx \Delta\Phi^{(i)} + \varepsilon_1^{(i)} + W_\Phi^{(i)},\ i \in \{1,..,M-1\},\end{aligned} \tag{5.18}$$

where $W_\Phi^{(i)}$ is the noise that affects the estimation, and

$$\begin{aligned}\varepsilon_1^{(i)} &= \frac{1}{N_{AVG}} \sum_{n=0}^{N_{AVG}-1} 2\pi\Delta f^{(i)}nT, \\ &= \pi\Delta f^{(i)}(N_{AVG}-1)T\end{aligned} \tag{5.19}$$

is the rotation factor due to the CFO. From (5.19), and since $\Delta f^{(i)} = f^{(i)} - f^{(i+1)},\ i \in \{1,..,M-1\}$ has zero mean and standard deviation $\sqrt{2}\sigma_{CFO}$, we obtain the standard deviation of $\varepsilon_1^{(i)}$ as

$$\sigma_{\varepsilon_1} = \sqrt{2}\pi\sigma_{CFO}(N_{AVG}-1)T. \tag{5.20}$$

In Fig. 5.4, we report σ_{ε_1}.

As it can be deduced from (5.18), the rotation factor $\varepsilon_1^{(i)},\ i \in \{1,..,M-1\}$ limits the performance of the estimator introducing a phase error which is proportional to the number of samples N_{AVG} used in the averaging operation. We will also observe in the simulation results that the values of σ_{ε_1} in Fig. 5.4 are the values of the error floor exhibited by the RMSE curves evaluated as in (5.15).

To compensate this effect we have proposed the method COMP that comprises a CFO calibration. By applying this calibration, (5.11) can be rewritten as (5.18), where the rotation factor (that now we denote with $\varepsilon_2^{(i)}$) can be expressed as

$$\varepsilon_2^{(i)} = \pi(\Delta f^{(i)} - \hat{\Delta f}^{(i)})(N_{AVG}-1)T. \tag{5.21}$$

The standard deviation of the rotation factor $\varepsilon_2^{(i)}$ is

$$\sigma_{\varepsilon_2} = \pi\sigma_{\hat{\Delta f}}(N_{AVG}-1)T, \tag{5.22}$$

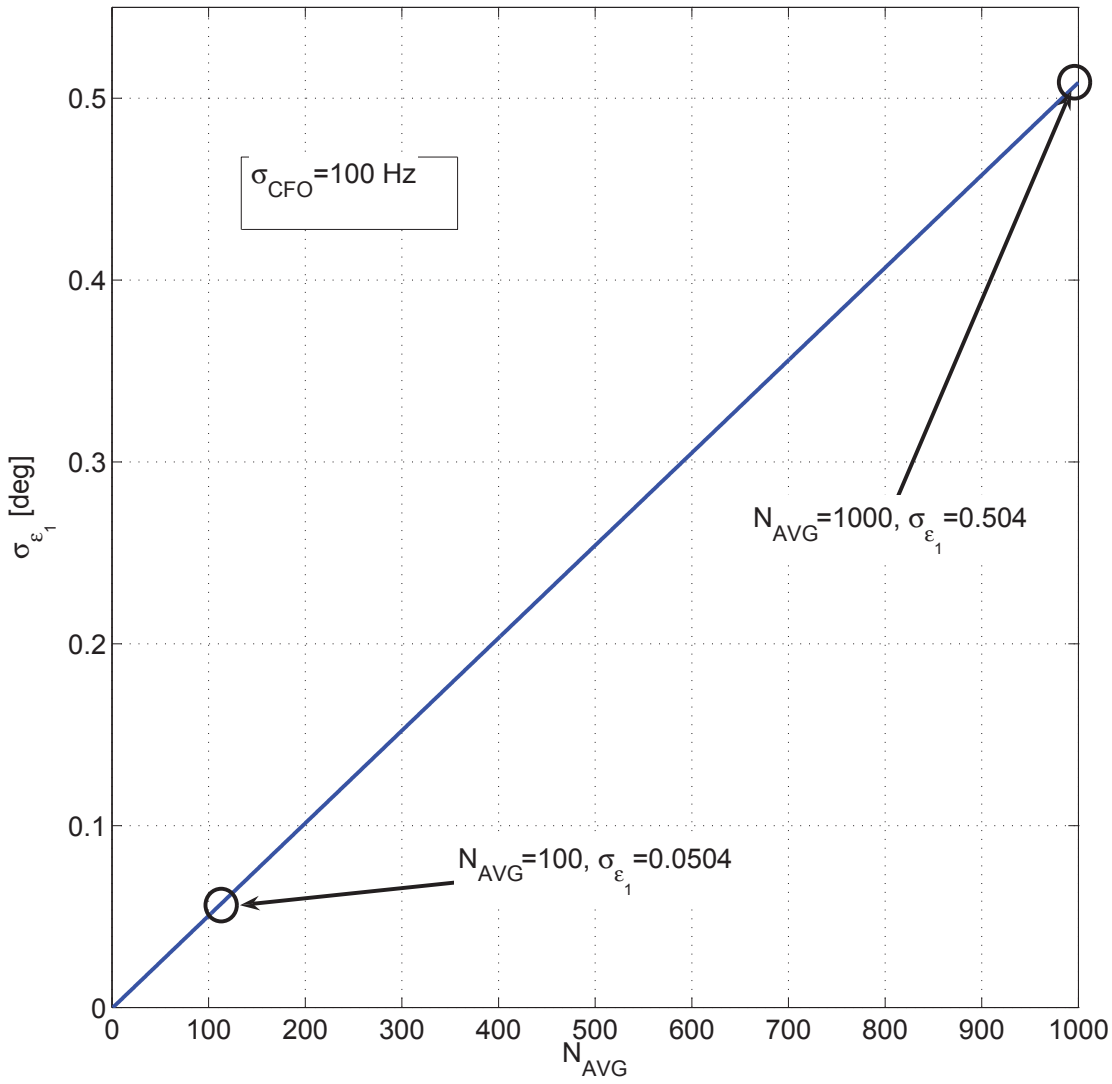

Figure 5.4: Standard deviation of ε_1 as a function of N_{AVG}.

where $\sigma_{\hat{\Delta f}}$ is the RMSE of the CFO estimator which is defined as

$$\sigma_{\hat{\Delta f}} = \sqrt{E\left\{\left|\Delta f^{(i)} - \hat{\Delta f}^{(i)}\right|^2\right\}}. \tag{5.23}$$

Hence, comparing (5.20) with (5.22), we can assert that the method COMP works better than the NOCOMP method if $\sigma_{\hat{\Delta f}} < \sqrt{2}\sigma_{CFO}$.

In order to determine a lower bound for the CFO estimator performance, we have evaluated the root of the Cramer-Rao Bound (RCRB) for the estimation of the CFO from (5.9).

Its derivation is reported in Appendix 9.7. It reads

$$\sigma_{\hat{\Delta f}} \geq \sqrt{\frac{3}{(2\pi T)^2 \gamma_\Lambda N_{CFO}(N_{CFO}-1)(2N_{CFO}-1)}}, \tag{5.24}$$

where γ_Λ is the signal-to-noise ratio obtained from the signal in (5.9). It is easy to prove that γ_Λ is 3 dB less than the SNR in (5.17).

In Fig. 5.5 we report the RMSE for the CFO estimator in (5.10) as a function of SNR, using $N_{CFO} = 1000$. It should be noted that the CFO estimation in (5.10) yields a RMSE

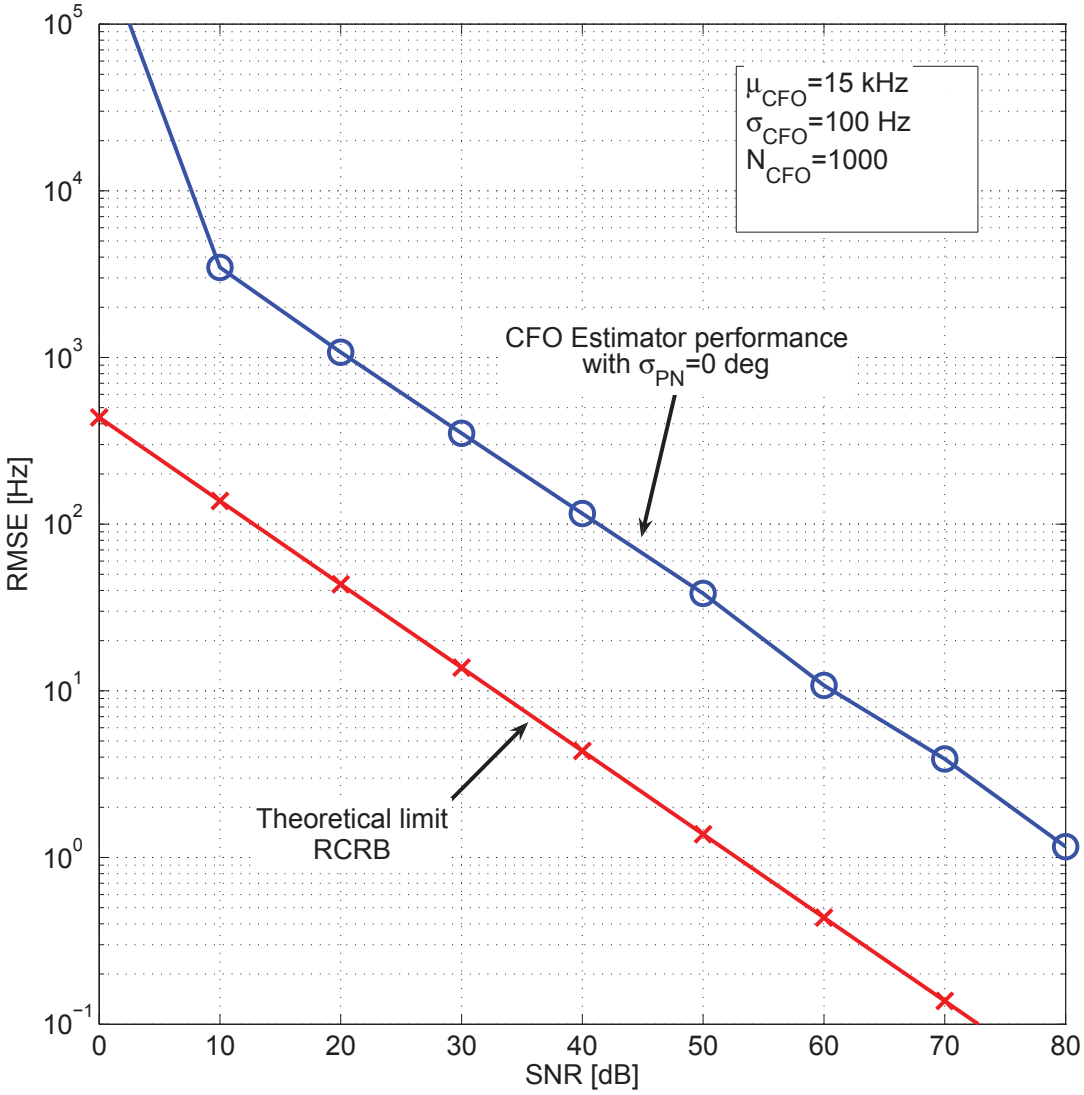

Figure 5.5: RMSE of the carrier frequency offset estimator in (5.10) as a function of SNR, with $L = 1$.

smaller than $\sqrt{2}\sigma_{CFO} = 141.4$ Hz for SNRs larger than approximately 38 dB. It follows that the estimation and compensation of $\Delta f^{(i)}$ is beneficial for SNRs larger than approximately 38 dB.

Phase Noise Effects

If we consider the COMP method and we do not neglect the PN contribution, (5.10) can be approximated as

$$\hat{\Delta f}^{(i)} \approx \Delta f^{(i)} + \xi^{(i)} + W_f^{(i)}, \tag{5.25}$$

where $W_f^{(i)}$ is the noise that affects the CFO estimation, and

$$\begin{aligned} &\xi^{(i)} \\ &= \frac{1}{2\pi N_{CFO} T} \left(\Delta\varphi^{(i)}(N_{CFO}T) - \Delta\varphi^{(i)}(0) \right) \end{aligned} \tag{5.26}$$

is a frequency shift due to the fact that the PN samples are not perfectly correlated. This frequency shift will determine an error floor in the RMSE of the CFO estimation, as already observed for the rotation factor $\varepsilon_1^{(i)}$.

From (5.26), we can obtain the standard deviation of $\xi^{(i)}$ as

$$\sigma_\xi = \frac{\sqrt{2\sigma_{PN}^2 - r_{PN}^{(i)}(N_{CFO}T)}}{\sqrt{2}\pi N_{CFO} T}, \tag{5.27}$$

where $r_{PN}^{(i)}(N_{CFO}T) = E\{\Delta\varphi^{(i)}(nT + N_{CFO}T)\Delta\varphi^{(i)}(nT)\}$ is the correlation of the samples $\Delta\varphi^{(i)}(nT)$ evaluated in $N_{CFO}T$. Then, if the PN samples were perfectly correlated after N_{CFO} sample periods, we would obtain $\sigma_\xi = 0$. On the other hand, if the PN samples are uncorrelated, with $N_{CFO} = 1000$ and $\sigma_{PN} = 1$ deg, we will obtain $\sigma_\xi = 277.8$ Hz. Hence, in this case the CFO compensation does not improve the performance since the effect of the PN is more detrimental than the CFO. In practical situations, the value of N_{CFO} can be chosen so that a tradeoff is made between the decrease of the correlation $r_{PN}^{(i)}(N_{CFO}T)$ and the overall decrease of σ_ξ computed as in (5.27).

5.5.2 Simulation Results

Carrier Frequency Offset Effects

In Fig. 5.6, the RMSE of the PO is shown as a function of the SNR evaluated by using the two methods described in Section 5.3, with $N_{AVG} = \{1, 10, 100, 1000\}$ and $L = 1$. In this case we have not considered the effect of the PN ($\sigma_{PN} = 0$ deg).

Now, let us consider the curves generated using the method NOCOMP. As we can observe, the increase of the SNR leads to better performance. Furthermore, by increasing N_{AVG} the

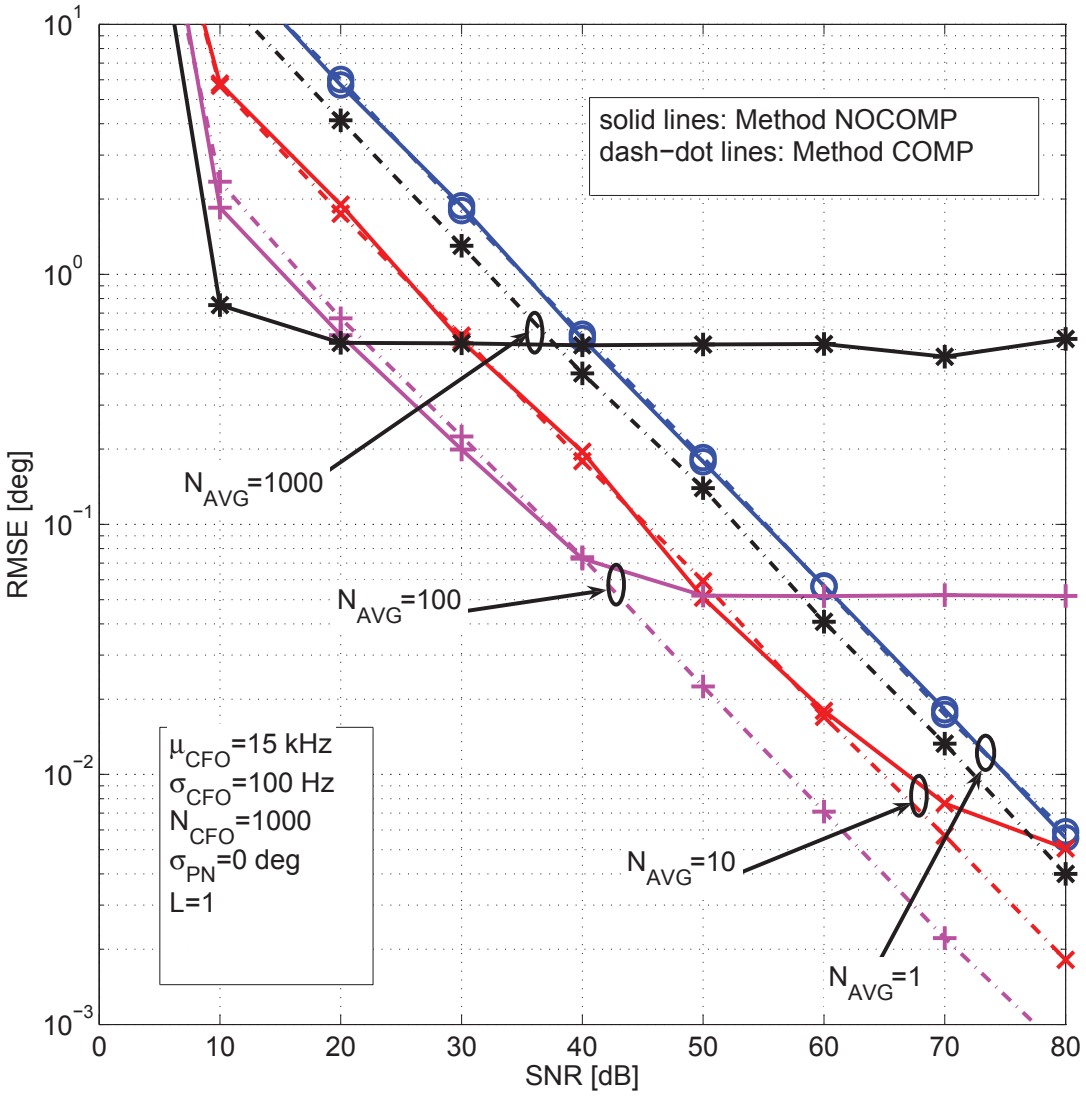

Figure 5.6: RMSE of the phase offset as a function of SNR and N_{AVG}, with the presence of carrier frequency offset, and $L = 1$.

RMSE decreases. However, for high SNR values the performance reaches a floor and this gets larger as the N_{AVG} increases. This is due to the presence of different CFOs among the array elements whose effect becomes dominant at high SNRs. In particular, with the considered parameters, we reach the values RMSE$\approx$ 0.05 deg with $N_{AVG} = 100$, and RMSE$\approx$ 0.5 deg with $N_{AVG} = 1000$ (also for the curves with $N_{AVG} = 1$ and $N_{AVG} = 10$ a floor in the performance occurs, but this is not visible with the considered SNR values), that are exactly the values of σ_{ε_1} obtained with (5.20) and reported in Fig. 5.4. Furthermore, in Fig. 5.6 we can observe that the curves obtained with the use of (5.11) do not experience a floor, as explained before. However, the RMSEs evaluated with $N_{AVG} = \{100, 1000\}$ are larger than those obtained with the method NOCOMP up to the SNR values lower than $\approx$ 38 dB, as

previously analyzed.

In Fig. 5.7 we show the aggregate RMSE of the DoA estimator in Chapter 3 when both the proposed calibration methods are used, with $N_{AVG} = \{1, 10, 100, 1000\}$, $N_{DOA} = 1$, and $L = 1$. The COMP and NOCOMP methods have identical performance with $N_{AVG} = 1$. It

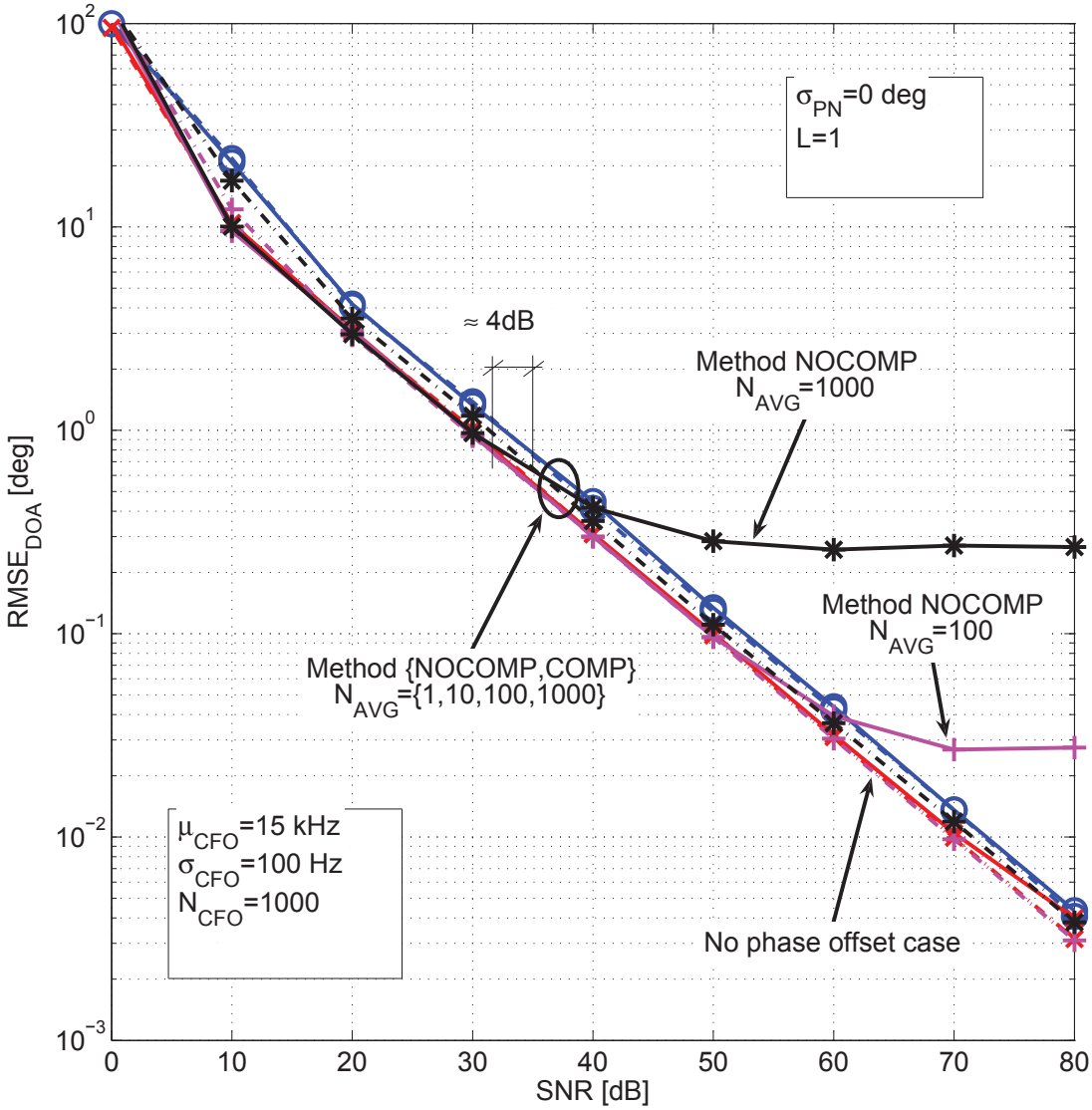

Figure 5.7: Aggregate RMSE of the DoA estimator as a function of SNR and N_{AVG}, with the presence of carrier frequency offset, and $L = 1$.

should also be noted that all the performance curves are concentrated into a range of 4 dB. The floor that occurs in Fig. 5.7 by using the method NOCOMP with $N_{AVG} = \{100, 1000\}$ is due to the CFO that is not compensated.

In Fig. 5.8, we consider a MP channel with $L = 2$ and $\gamma = \{10, 20, 30\}$ dB, and we show the RMSE of the PO as a function of the SNR, with $N_{AVG} = \{1, 10, 100, 1000\}$. It should

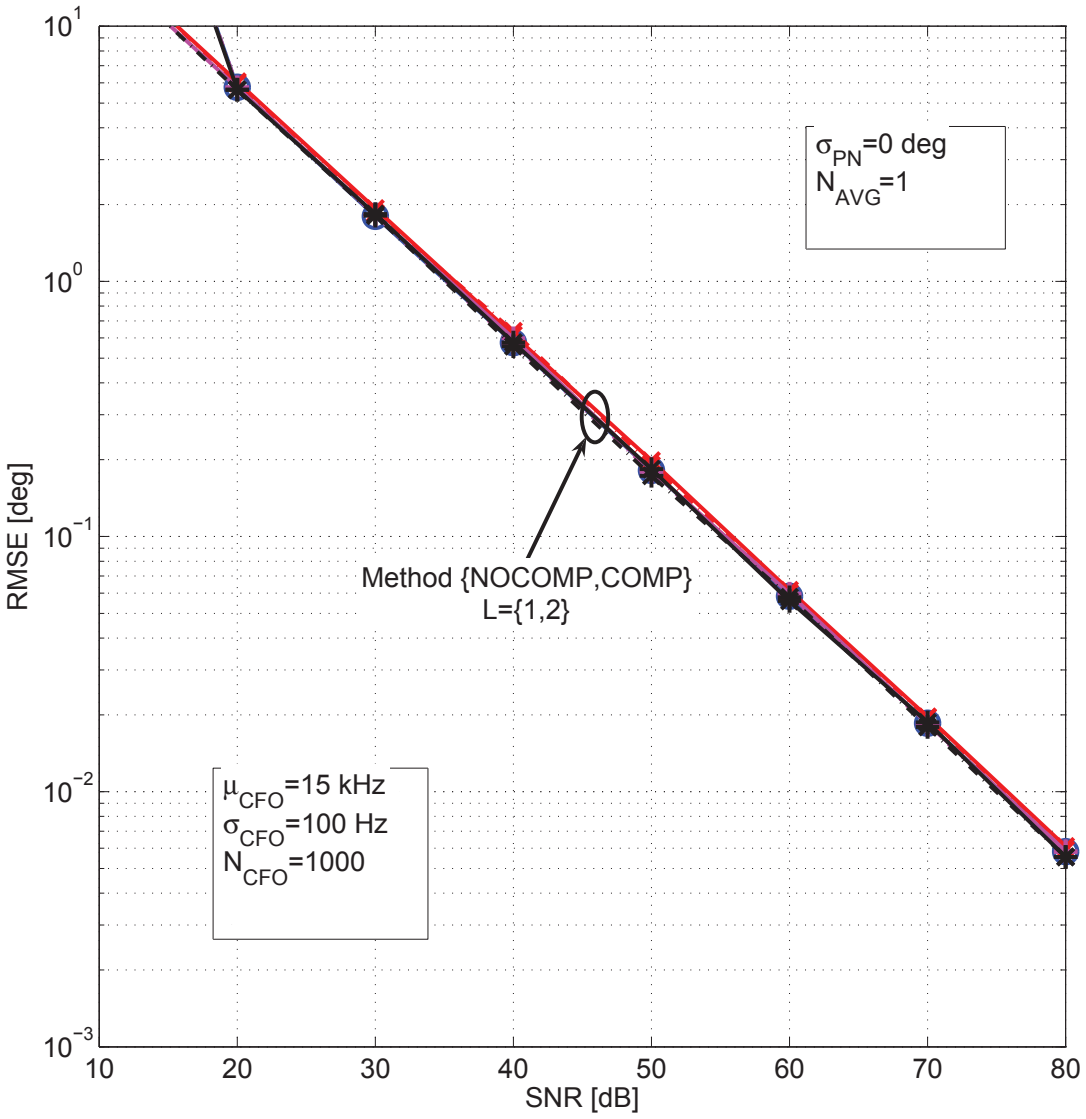

Figure 5.8: RMSE of the phase offset as a function of SNR and N_{AVG}, with the presence of carrier frequency offset, with $L = 2$.

be noted that the performance of the calibration method is not influenced by the presence of MP since the curve with $L = 1$ and those with $L = 2$ are practically overlapped.

Phase Noise Effects

In Fig. 5.9, we show the effect of the PN to the performance of the DoA estimator when we apply the method NOCOMP. We have considered the PN model described in Chapter 2, $N_{AVG} = \{1, 10\}$, and $N_{DOA} = 1$, while we have neglected the CFO, and $L = 1$. As we can observe, the error floor increases with the increase of N_{AVG}. In Fig. 5.10, we show the effect of the PN on the performance of the DoA estimator when we apply the calibration method,

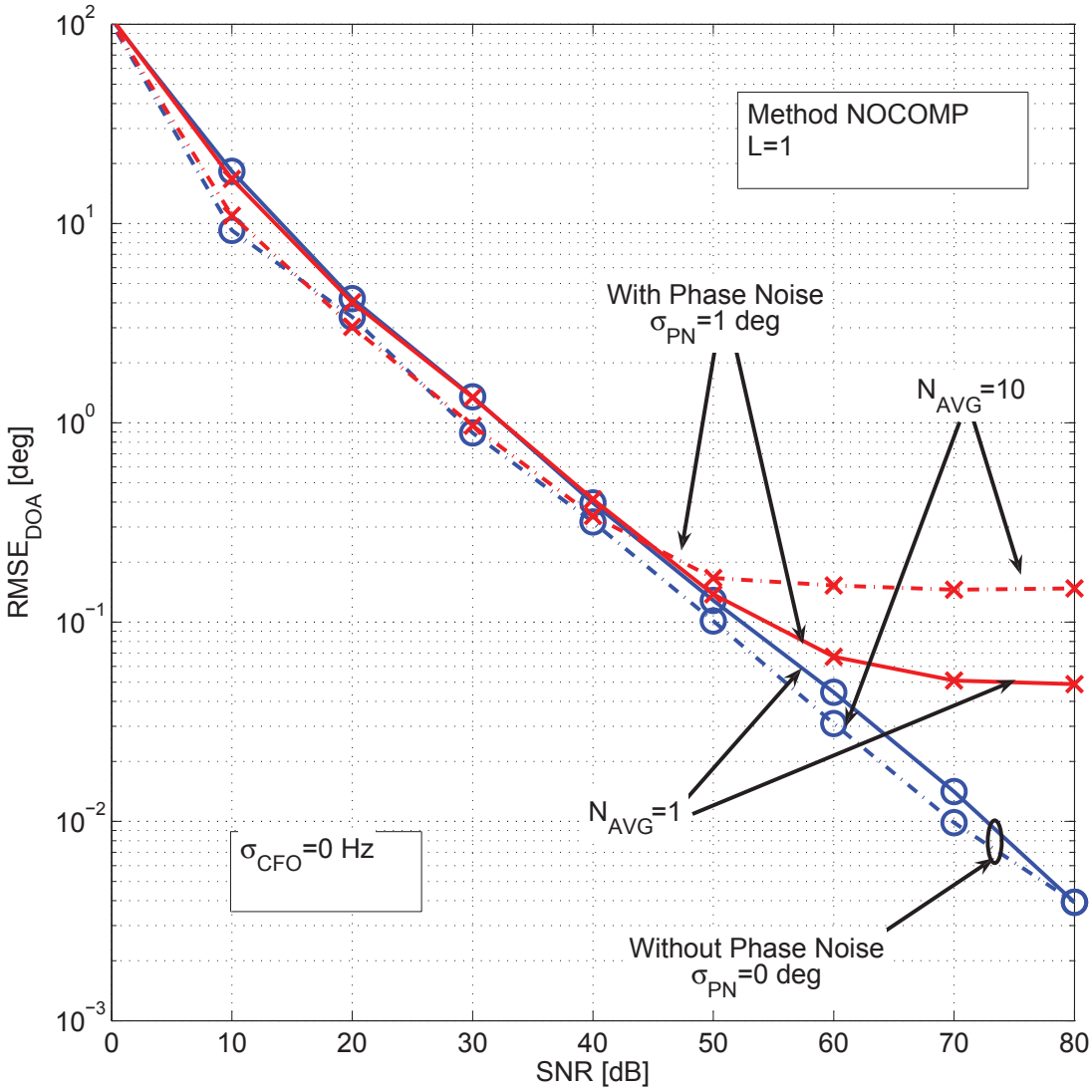

Figure 5.9: Aggregate RMSE of the DoA as a function of SNR and N_{AVG}, with the presence of phase noise, and $L = 1$.

with $N_{AVG} = \{10, 100\}$ and $N_{DOA} = 1$. Considering the curves associated to the method COMP, we can observe that the PN still limits the performance. It should be noted that with the values of PN and CFO considered, the two methods reach very similar performance. Assuming $N_{AVG} = 100$, the RMSE_{DoA} floor is as small as 0.4 deg. The error floor can be lowered with an opportunal choice of N_{CFO}.

5.6 Main Findings

We have considered the array calibration problem when PO, CFO, and PN occur among the array signals. We have proposed a novel technique for the calibration of the antenna array

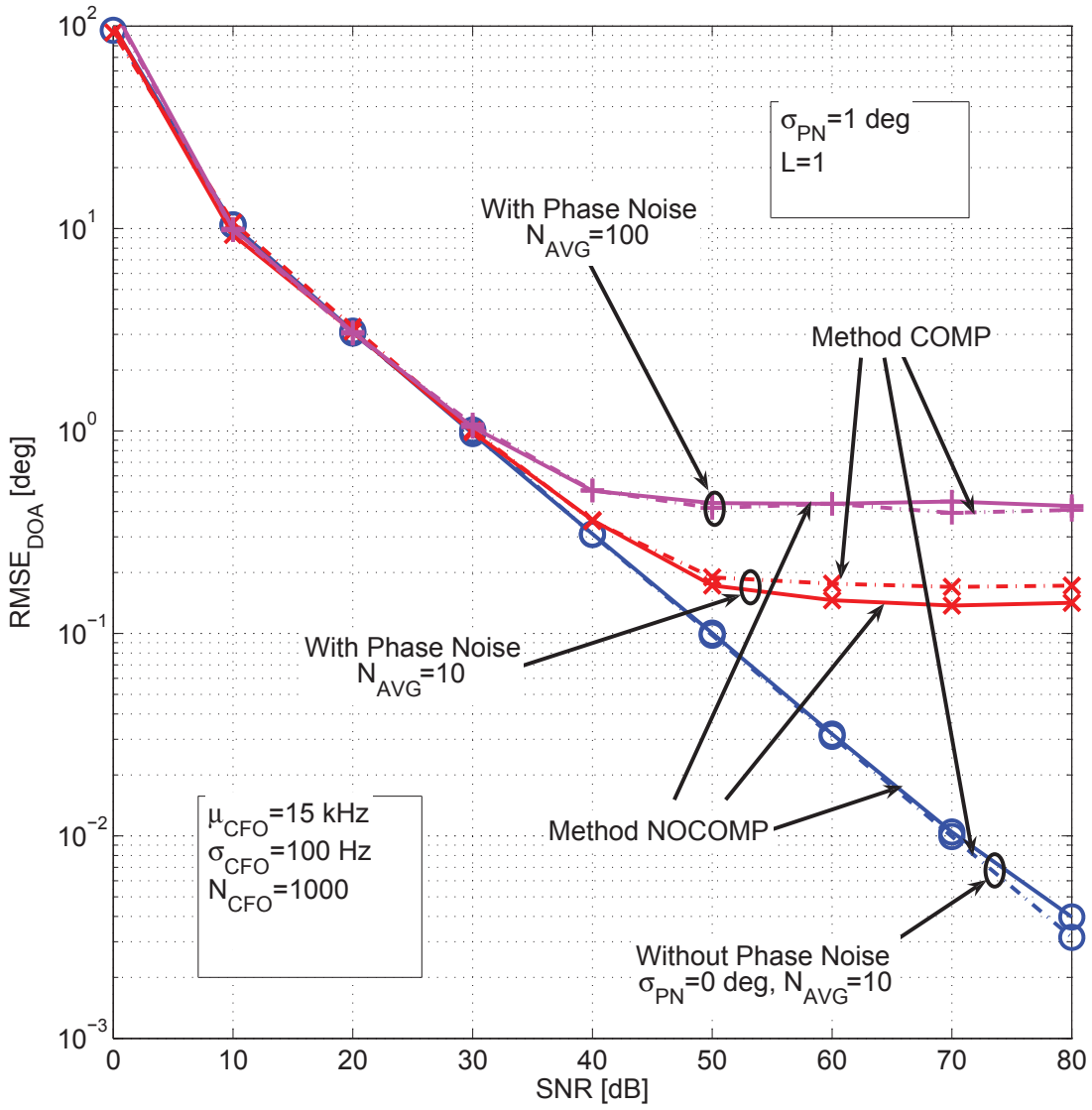

Figure 5.10: Aggregate RMSE of the DoA as a function of SNR, with $N_{AVG} = \{10, 100\}$, both the presence of carrier frequency offset and phase noise, and $L = 1$.

system that relies on the use of a particular antenna array which allows the estimation of the PO differences of the array. The array comprises a common antenna which brings the same signal to each receiver. After the calibration step is performed, analog switches can select the antennas for the DoA estimation. We have shown that the calibration method performance does not degrade in the case of a MP channel.

This calibration technique works with either equal CFOs or different CFOs among the receivers. To better address the latter case, we have proposed another method which firstly estimates the CFO differences and then it performs compensation. The analysis has revealed that the method without CFO compensation works better at low SNRs while at high SNRs

it exhibits an error floor. Consequently, at high SNRs it is beneficial to perform CFO compensation.

Another important issue is the effect of the PN. The PN compensation method can mitigate the effects of PN depending on its spectrum, i.e., if it is slowly time variant.

Chapter 6

Multiple Antenna Receiver Architectures for DoA Estimation

In Chapter 2, we have described the full-parallel uncoherent (FP) architecture, i.e., a multiple antenna receiver composed by independent receivers with uncoherent local oscillators (LOs). Next, in the following three chapters it is shown that the LO uncoherence can severely affect the performance of a direction finding (DF) system. In this chapter, we firstly describe different single radio frequency (RF) front-end (FE) receivers, and we compare them in terms of costs, analog complexity, non idealities, power consumption, etc. Multiple antenna receiver architectures are assessed, with particular emphasis on the advantages or disadvantages brought by them for the DF purpose. Next, we describe the non idealities that are introduced by the antenna array. Finally, some simulation results are shown in terms of root mean squared error (RMSE) in order to compare the proposed architectures, and to show the effect of the non idealities on the direction of arrival (DoA) estimation.

6.1 Introduction

In the last decades, the estimation of the DoA of wavefronts has been widely addressed. In particular, high-resolution DF algorithms have been developed [18] and theoretical analysis as well as simulation results have demonstrated their excellent performance. However, it was shown that improved results can be reached either with very high signal to noise ratio (SNR) or by increasing the number of antenna elements. For what the first aspect concerns, the performance of a real system in terms of achievable SNR is limited by practical issues. In fact, the real behaviour of a multiple antenna receiver differs from the ideal one because of the presence of several non idealities, as already described in the previous chapters. These can be divided in two main categories: the impairments due to the antenna array [35], and the impairments due to the multiple FEs, shown in Chapter 2. The former are strongly influenced by the manufacturing accuracy and, depending on the required DoA resolution,

have to be taken into account. The multiple FE non idealities, instead, are usually not considered in the DoA estimation literature, even if they can have a detrimental effect on the performance. For what the increasing of the antenna elements concerns, instead, it is usually limited by practical considerations, such as size, costs, and also complexity.

This chapter considers several implementation aspects related to the DoA estimation. Firstly, we provide an overview of single RF FE solutions which are the basis of a multiple antenna system, and we compare them in terms of non idealities, analog complexity, costs, power consumptions and chip area. After that, we introduce some possibilities to combine the single RF FEs in order to implement a multiple antenna receiver, showing their advantages and disadvantages in the context of DF. We also assess some multiplexed architectures, i.e., multiple antenna receiver realized with a single RF FE, and their capabilities to deal with the DoA estimation. Furthermore, we describe the imperfections introduced by the antenna array. Finally, we provide a quantitative comparison among these solutions to highlight the impact of the different impairments.

This chapter is organized as follows. In Section 6.2 we describe the single RF FE architectures. The multiple antenna receiver implementations are analyzed in Section 6.3. In Section 6.4, the impairments introduced by the antenna array are discussed. In Section 6.5 a numerical comparison is proposed in terms of root mean squared error (RMSE). Finally, Section 6.6 summarizes the main findings.

6.2 Single RF Front-End Architectures

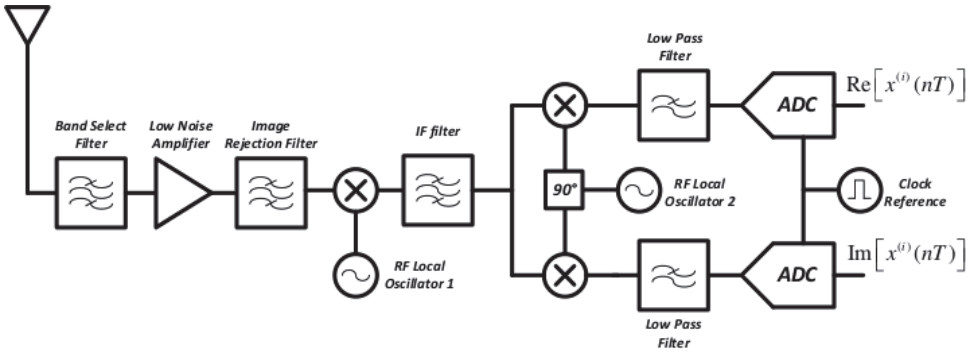

Figure 6.1: Super-heterodyne receiver.

The super-heterodyne receiver (the first receiver architecture for wireless communication), was introduced in 1918 [70]. In this solution (see Fig. 6.1), the translation of the RF frequency is divided into two (or more) conversion stages that bring to a non zero IF (intermediate frequency). It uses high quality filters to provide the desired performance, implemented using expensive SAW (surface acoustic wave) filters that are unsuitable for integration. This architecture guarantees optimum performance in terms of sensitivity and selectivity. However, the presence of the high-Q discrete components does not allow a full

integration on-chip which increases occupation area, complexity, and cost. Furthermore, if a in-phase and in-quadrature (I&Q) modulation stage is considered (that allows working with complex signals, as today required by most of the wireless standard), I&Q mismatches between in-phase and in-quadrature signal paths deteriorate the receiver performance.

In order to reduce complexity, the direct conversion receiver (or zero-IF) was proposed. In Fig. 6.2, we depict its main circuit blocks. As it can be observed, the signal captured by the

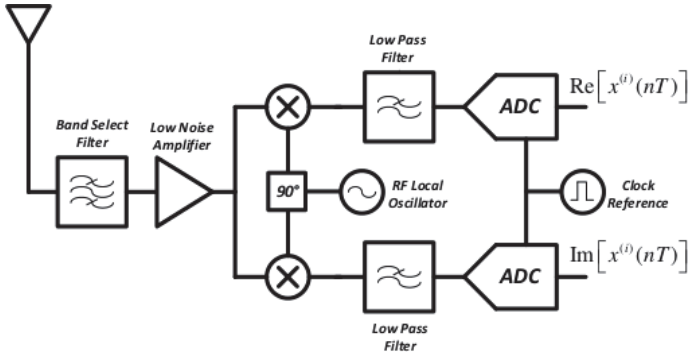

Figure 6.2: Direct conversion (or zero-IF) receiver.

antenna is directly downconverted to baseband, and this yields to a decrease of complexity (and costs) w.r.t. the super-heterodyne receiver, in addition of allowing a larger degree of integration. However, the reduced complexity comes at the expense of reduced performance. In fact, there are several drawbacks in this architecture among which the major limitation is the DC offset. This impairment is mainly due to transistor mismatches in the receiving path and ADC imperfections (that give a static contribution), spurious leakage to antenna and large near channel interferers leaking into the receiver LO port (that give a dynamic contribution). Other recognised problems are second-order distortion, flicker noise [31], and, as for the super-heterodyne, I&Q mismatches.

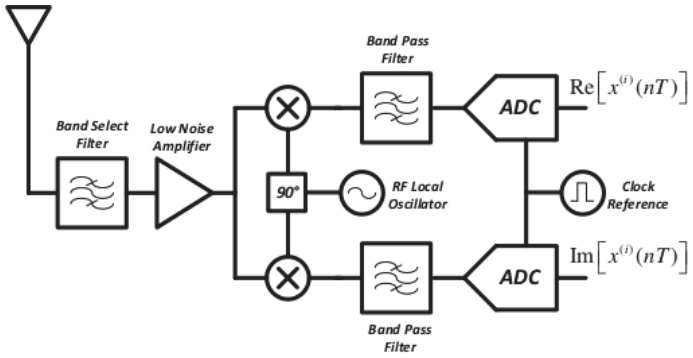

Figure 6.3: Low-IF receiver.

A similar configuration is the low-IF receiver (Fig. 6.3), in which the RF signal is mixed down to a nonzero IF (few hundred kHz to several MHz) instead of going directly to DC. This solution tries to combine the advantages of both the zero-IF receiver (i.e., integration) and the super-heterodyne receiver (i.e., performance). In fact, this architecture still allows

a high level of integration and does not suffer from the DC offset problems. Nonetheless, as in the super-heterodyne receiver, an image suppression step is required. It should also be noted that the downconversion at a frequency larger than zero involves the use of a larger ADC bandwidth and, consequently, it requires larger power consumption, besides increasing the noise floor. Finally, I&Q imbalances are still present.

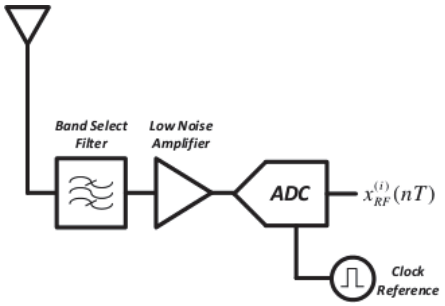

Figure 6.4: Band-pass sampling receiver.

Another possible configuration (that moves toward the software-defined radio concept [31]) is the band-pass sampling receiver, shown in Fig. 6.4. In this architecture, the signal is passed to the digital domain after band-pass filtering and low noise amplification. This configuration is based on the fact that all the energy from DC to the input analogue bandwidth of the ADC will be folded back to the first Nyquist zone, without any mixing down conversion needed. This is because a sampling circuit (included into the ADC) is replacing the mixer module. For what the I&Q downconversion concerns, this is digitally implemented and it allows obtaining better matching accuracy w.r.t. the analog solution. This architecture reduces the number of required components. However, some critical requirements exist, for example the bandwidth of the sample and hold circuit inside the ADC must include the RF carrier, which is a serious problem. Moreover, the noise energy outside the desired Nyquist zone has to be filtered in order to avoid a signal-to-noise ratio degradation. Nonetheless, even if the noise is filtered, it should be noted that this implementation has the worst performance in terms of noise.

The performance of the considered architectures are listed in Tab. 6.1, where SHR stands for super-heterodyne receiver, DCR for direct conversion receiver, LIFR for low-IF receiver, while BPSR stands for band-pass sampling receiver. The direct conversion receiver

Parameters	SHR	DCR	LIFR	BPSR
Complexity	High	Low	Low	Low
Cost	High	Low	Moderate	Low
Noise	Low	Moderate	Low	High
Image Frequency	Yes	No	Yes	No
DC Offset	No	Yes	No	No
I&Q Imbalance	Yes	Yes	Yes	No

Table 6.1: Comparison of the receiver architecture features.

is probably the best solution for DF applications that usually needs the use of many FEs. This is because of its good trade-off between complexity/costs and performance.

6.3 Multiple Antenna Systems Architectures

After the investigation of the single FE architectures (and having identified the direct conversion receiver as one of the best solution), in this section several implementations of a multiple antenna system are illustrated. Firstly, the implementation of a multiple antenna system by using multiple FEs is discussed, with particular emphasis on the influence of the LO signal distribution. Then, the architectures that rely on a single FE are assessed with respect to the DoA estimation problem.

6.3.1 Full-parallel architecture

In Fig. 6.5 is depicted a full-parallel multiple RF FE architecture, in which each antenna is connected to a dedicated analog chain. This architecture is an obvious solution, however its

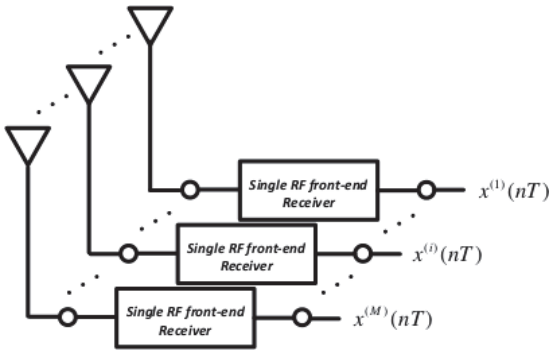

Figure 6.5: Full-parallel RF front-end architecture.

cost linearly increases with the number of required antennas. There exists also performance drawbacks adopting this solution, due to the inability of reproducing circuits with identical characteristics; this mainly leads to have mismatches among channels[1]. In the context of DF systems, these imbalances may deteriorate the overall performance [71]. These channel mismatches can be of gain or phase. Gain mismatches, that can lead to a little SNR deterioration, can be in the order of $1-2$ dB. Phase mismatches (we are not taking into account neither the phase contributions introduced by the LO signals nor the one due to different cable lengths that will be addressed separately), that have a detrimental effect in this application, are usually limited to few degree fractions, but they directly affect the DoA performance. However, the phase imbalances are usually static and they can be calibrated.

Another non ideality in the full-parallel architecture is due to the limited channel isolation. Usually, multiple receiver system can reach $40-50$ dB of channel isolation, so this

[1]With channel we mean the entire cascade from the antenna to the ADCs.

effect can usually be neglected.

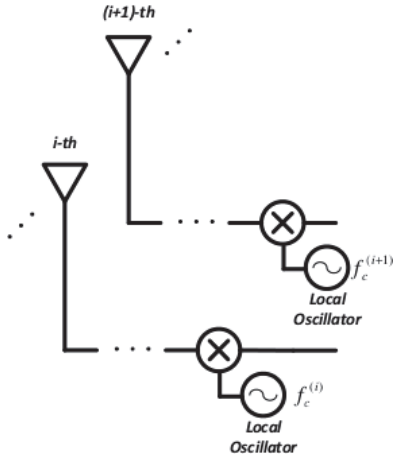

Figure 6.6: Uncoherent local oscillators.

A fundamental aspect in this kind of implementation is the generation of the RF LO signals. In fact, if we consider a full-parallel system with uncoherent RF LOs (which we refer to it simply as FP in the following), as depicted in Fig. 6.6, each signal will have to cope with its own carrier frequency offset (CFO), phase offset (PO), and phase noise (PN). These impairments generate time-variant phase mismatches among the channels that lead to a wrong DoA estimate as shown in Chapter 3. In order to cope with this problem, a calibration procedure has to be implemented [35], and this involves additional computational resources. However, a calibration usually compensate static phase imbalance, so the dynamic contribution limits the DoA estimator performance, as shown in Chapter 3.

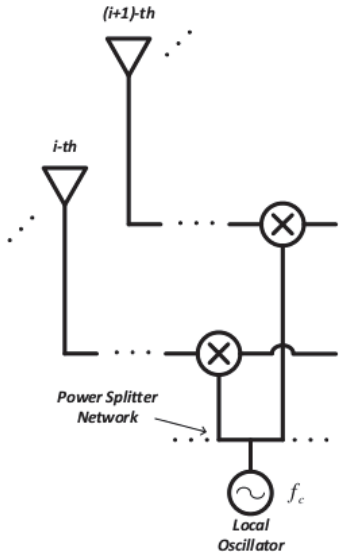

Figure 6.7: Coherent local oscillators.

Another possibility is to use a full-parallel architecture with a common LO (coherent) as in Fig. 6.7 (which we refer to it as FPC in the following), where the LO signal and its non

idealities is shared with all the channels. In this way the impairments affect the output signals equally, and the common phase contribution does not influence the DoA estimation, since most of the developed high-resolution algorithms are invariant to a common rotation factor. This can also be deducted from the following consideration: the DoA estimation algorithms are based on the phase differences estimation among the different antenna signals. By using the same LO signal for the downconversion step, non idealities equally affect each channel and do not influence the DoA estimate. On the contrary, by using different LO signals, the differences among carrier frequency offsets (CFOs), phase offsets (POs) and phase noises (PNs) deteriorate the performance, as shown in Chapter 3.

It should be noted that the implementation of a full-parallel FE system, particularly if it requires many antennas, can be done by integrating embedded receivers that already include their own RF LO generation system. Hence, in this case the generation and distribution of a common LO signal requires more efforts.

6.3.2 Multiplexed architectures

In order to reduce the costs of the full-parallel solution, the use of a single common FE for the elaboration of all the received signals was proposed in [72] for data communication. The single common FE is shared with all the antenna elements by using a multiplexing technique. Three different possibilities are described in the literature: time-division, frequency-division, and code-division multiplexing. *Time-multiplexed* (TMX) architecture is the simplest solu-

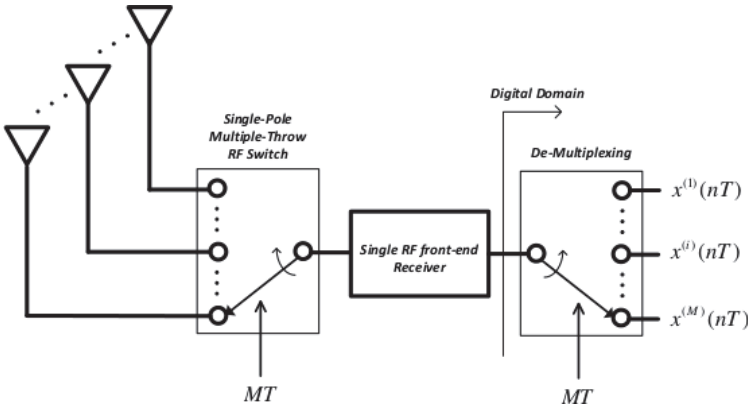

Figure 6.8: Time-multiplexed single RF front-end architecture.

tion (Fig. 6.8). This system is realized with a single RF FE shared with all the antenna elements by time-multiplexing the antenna signals using a single-pole multiple-throw RF switch. This architecture, since it has only one RF FE circuit, does not suffer for mismatches among the channels. However this system requires wider bandwidth, e.g., at least M-times the bandwidth of the RF FE of the full-parallel case (where M is the number of antenna elements), which leads to an increase of the power requirements since the ADCs have to be sampled at higher rate. Another shortcoming of this multiplexing solution is the

signal to noise ratio (SNR) degradation [72], [73] due to the increased bandwidth, and also due to the switch losses. For what the applicability of this architecture to DF concerns, it should be noted that, differently from the full-parallel case, symbol synchronization is required [74].

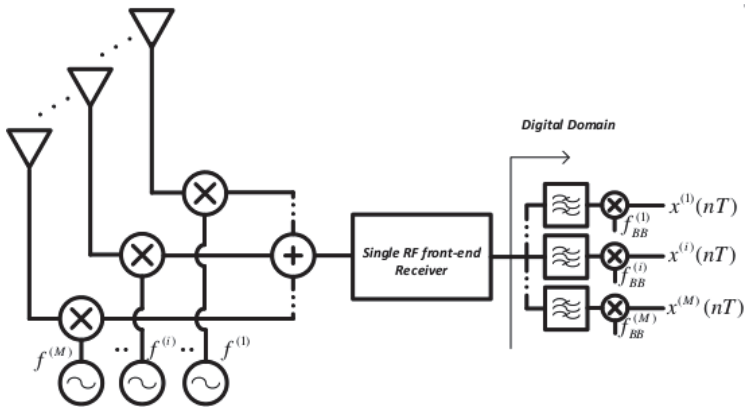

Figure 6.9: Frequency-multiplexed single RF front-end architecture.

The second architecture is the *frequency-multiplexed* (FMX), depicted in Fig. 6.9. In this system, the M signals from the antennas are multiplexed together by applying a different frequency offset to each of them. This offset will corresponds to a radio channel spacing [44]. As for the TMX solution, the FMX architecture requires a single RF FE with wider bandwidth, e.g., M-times the bandwidth of the full-parallel case. Morever, the generation of the M RF signals closely spaced makes this solution very challenging. For this reason, it is not usually considered as a viable solution.

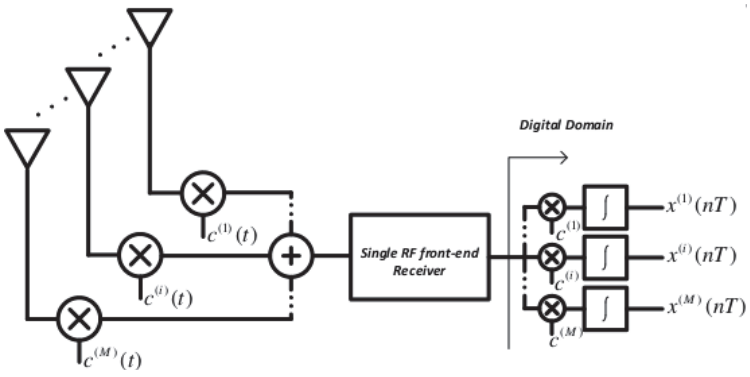

Figure 6.10: Code-multiplexed single RF front-end architecture.

The last architecture is the *code-multiplexed* (CMX) [73], illustrated in Fig. 6.10. In this structure, the received signal at each antenna is uniquely identified by the application of an orthogonal code, e.g., Walsh functions. After that, all the resultant signals are combined into one signal that passes through the single RF receiver. The combined signals can then be separated by making use of the orthogonal property of the codes. Even this solution requires at least M-times bandwidth increase. Moreover, it requires more effort w.r.t. the TMX solution to implement the code modulators.

Parameters	FP	FPC	TMX	FMX	CMX
Complexity	Low	Low	Low	High	Moderate
Cost	High	High	Low	Low	Low
Losses	None	None	Switch	Mixers	Code mod.
Gain Mismatches	Yes	Yes	No	No	No
Phase Mismatches	Yes	Yes	No	No	No
LO Coherence	No	Yes	Yes	Yes	Yes
I&Q Imbalance	Yes	Yes	Yes	Yes	Yes

Table 6.2: Pros and cons of the multiple antenna system architectures.

A practical advantage in contrast to the TMX and the FMX solution is the immunity of this system to adjacent channel interferer, as explained in [73].

In Tab. 6.2 we report pros and cons of the discussed architectures. If higher SNRs are required, a FPC solution will be preferable. However, its cost linearly increases with the number of antennas. For this reason, when the application requires many elements, a multiplexed solution can be adopted.

In order to cope with the increase of the noise level, in particular if the number of elements is high, a possible way is to implement a hybrid architecture, i.e., we divide the array into small subarrays that are connected to several multiplexed FEs. For example, if we have an array of $M = 10$ elements, we can use five CMX FEs in parallel. In this way, we have halved the number of FEs with a loss of only 3 dB.

It should be noted that the I&Q imbalance can have detrimental effects for the coherent architectures (as much as for the uncoherent), even if this is never taken into account in the literature. Furthermore, with respect to the direct conversion receiver, also the DC offset can affect the DoA estimation performance as it has been shown in Chapter 3. Nonetheless, simple post-processing algorithms can reduce its effect, yielding it negligible for this application.

Finally, the channel isolation performance of the multiplexed architectures depend on the orthogonality properties of the multiplexer. For example, in the TMX and CMX cases, an ortogonality loss can be introduced by an uncorrect synchronization between multiplexer and demultiplexer, even if this problem can be avoided with a good circuit design.

6.4 Antenna Array Impairments

In this section we describe the non idealities that can affect an antenna array. These can be:

1. manufacturing inaccuracies,

2. non omnidirectional antennas,

3. mutual coupling,

4. correlation among the antenna signals caused by the environment,

5. phase offsets due to different cable lengths.

These contributions do not depend on the multiple antenna system FE architecture and they are usually present. Now we introduce all these effects, except for the correlation among the antenna signals that has not been considered in this work.

6.4.1 Manufacturing Inaccuracies

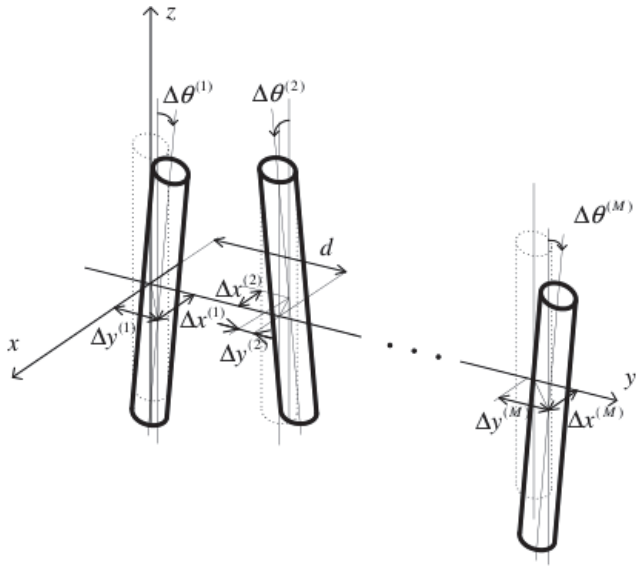

Figure 6.11: Examples of array location errors.

The manufacturing inaccuracies due to the finite precision of the tools that realize the antenna array can cause several mismatches among the antenna elements. One of this is the non correct displacement of the antenna array elements, as shown in Fig. 6.11. These imperfections bring to a distortion of the array manifold. This is a well known problem in the literature, and many solutions have been proposed to deal with. Obviously, the effect of this impairment to the final performance depends on how the displacement error is modeled. In [39], a two dimensional Gaussian distribution is considered for what the displacement errors concern. In Section 6.5 we will consider the same model.

Other inaccuracies occur in the fabrication of the antennas that can lead to different antenna gains, particularly if the elements are misaligned w.r.t. the polarization of the impinging wave. Nonetheless, all these fabrication inaccuracies may have a marginal contribution and usually they can be neglected.

6.4.2 Non Omnidirectional Antennas

Each element of a real antenna array has a gain which is function of the DoA [71], as we have also shown in Chapter 4. Nevertheless, as explained in 6.3, this non uniform radiation

pattern can introduce an SNR degradation, but it has not a direct impact on the DoA performance, and for this reason we will not addressed it in the following analysis.

6.4.3 Mutual Coupling

According to the spatial Nyquist criteria, the element of an antenna array for DoA estimation should be spaced up to $\lambda/2$. Since the elements are close together, mutual coupling occurs [75, 76]. This effect changes the phase distribution of the electric current in the array elements. As a result, gain, bandwidth, radiation pattern, and input impedance of the antenna array are affected. There is a huge literature in this field, for both modeling and compensation algorithms.

6.4.4 Different Cable Lengths

Finally, we address the connection cable from the antenna element to the FE input. In fact, if the cable lengths $l_{link}^{(i)}$ are not equal, a different phase rotation $\zeta^{(i)}$ among the element of the array manifold will be introduced. A minimum difference in cable length $\Delta = 0.1$ mm can generate a phase shift equal to $2\pi f_c \frac{\Delta}{c_0} = 0.28$ deg if $f_c = 2.4$ GHz, and 0.7 deg if $f_c = 5.8$ GHz. Thus, as function of the desired accuracy, these phase shift can be neglected or not.

6.5 Architecture Comparison

In order to test the performance of the receiver architectures, we will consider, without loss of generality, the estimation of a single source signal from direction $\phi_0 = 30$ deg, with the well-known subspace based root-MUSIC algorithm [18] using N samples. The source is a single-tone signal at frequency $f_c = 2.412$ GHz that impinges to a linearly equispaced (LES) antenna array of $M = 4$ elements, with interelement distance $d = \frac{\lambda}{2}$.

The performance will be analyzed in terms of root mean squared error (RMSE) which is defined as RMSE $= \sqrt{E\left\{|\phi_0 - \tilde{\phi}_0|^2\right\}}$, where $\tilde{\phi}_0$ is the estimated AoA. The RMSE will be shown as function of the SNR obtained with a single receiver in the full-parallel case.

6.5.1 System Model

All the impairments described in this work, with the exception of the I&Q imbalance, can be described by the following model

$$\mathbf{x}(nT) = \mathbf{\Psi}(nT, \phi_0)\mathbf{a}(\phi_0)s(nT) + \mathbf{w}(nT),\ n \in \{0, .., N-1\}, \tag{6.1}$$

where $\mathbf{x}(nT)$ is the M-length received signal vector, $s(nT)$ is the received baseband signal, $\mathbf{a}$ is the array manifold as in (1.8), $\mathbf{w}(nT)$ is the M-length complex noise vector, while

$\mathbf{\Psi}(nT, \phi_0)$ is the squared matrix that describes the various impairments. As it can be noted, $\mathbf{\Psi}(nT, \phi_0)$ can be a function of both the temporal index, e.g., when different CFOs $f^{(i)}$ and time-variant PNs $\varphi^{(i)}(nT)$ occur, i.e., $\mathbf{\Psi}$ is diagonal with $\psi_{i,i} = e^{j2\pi f^{(i)} nT + j\varphi^{(i)}(nT)}$, and the AoA, e.g., when describes the non omnidirectional gain of the antennas $g^{(i)}(\phi_0)$, i.e., $\mathbf{\Psi}$ is diagonal with $\psi_{i,i} = g^{(i)}(\phi_0)$, or the non correct displacement of the elements, i.e., $\mathbf{\Psi}$ is diagonal with $\psi_{i,i} = e^{-j\frac{2\pi}{\lambda}\Delta_x^{(i)}\cos(\phi_0) - j\frac{2\pi}{\lambda}\Delta_y^{(i)}\sin(\phi_0)}$, where $\Delta_x^{(i)}$ and $\Delta_y^{(i)}$ are the displacement errors. Furthermore, it has a symmetric Toeplitz structure in the case of mutual coupling (with unitary diagonal). In this analysis, the out-of-diagonal elements of the mutual coupling matrix are: $\psi_1 = 0.0916 + j0.1509$, $\psi_2 = -0.0511 - j0.0603$, $\psi_3 = 0.0375 + j0.0339$ as in [76].

When the I&Q imbalance effect has to be taken into account, the system model becomes [77]

$$\mathbf{x}(nT) = \mu\mathbf{a}(\phi_0)s(nT) + \nu\mathbf{a}^*(\phi_0)s^*(nT) + \mathbf{w}(nT), \tag{6.2}$$

where μ and ν are the coefficents that describe the amount of I&Q imbalance. In this analysis, we have assumed 1 dB of I&Q gain imbalance and 1 deg of I&Q phase imbalance.

6.5.2 Numerical Results

In this part we perform several simulations in order to understand the effect of the impairments. In this analysis, we assume that a phase pre-calibration has been performed in order to compensate all the static phase contributions. Furthermore, we do not address the case directional antennas. Firstly, we compare the performance of the different architectures with only the LO impairments. We have chosen the code-multiplexed solution from the multiplexed architectures to make a comparison with the other architectures. Next, we consider only the coherent solutions to investigate the effect of the other impairments.

In Fig. 6.12 we show the performance of FP, FPC, and CMX architectures as function of the SNR, with $N = \{1, 10, 100\}$ samples, when CFOs and PN are present. Firstly, we can observe that the multiplexed architecture have a 6 dB penalty with respect to the full-parallel ones. As described above, this is due to the bandwidth enhancement that increases the noise floor. Furthermore, it should be noted that for high SNR values, the $N = 10$ FP performance slightly deteriorates, while the $N = 100$ curve is strongly impaired. This is due to the CFOs and the PN impairments. As explained in Chapter 3, the performance degradation is a function of the receiver parameters, and the number of samples.

In Fig. 6.13, a comparison among the other impairment's effect is done, considering only the coherent architectures. For completeness, we have reported the performance for both the FPC and the CMX architectures. The considered impairments are the mutual coupling, the I&Q imbalance, and the antenna displacement error. In particular, we have considered a standard deviation of the displacement error of 1% respect to the interelement distance. It should be observed that the antenna displacement error seems to be the more benign impairment. Contrarily, the mutual coupling and the I&Q imbalance can drastically

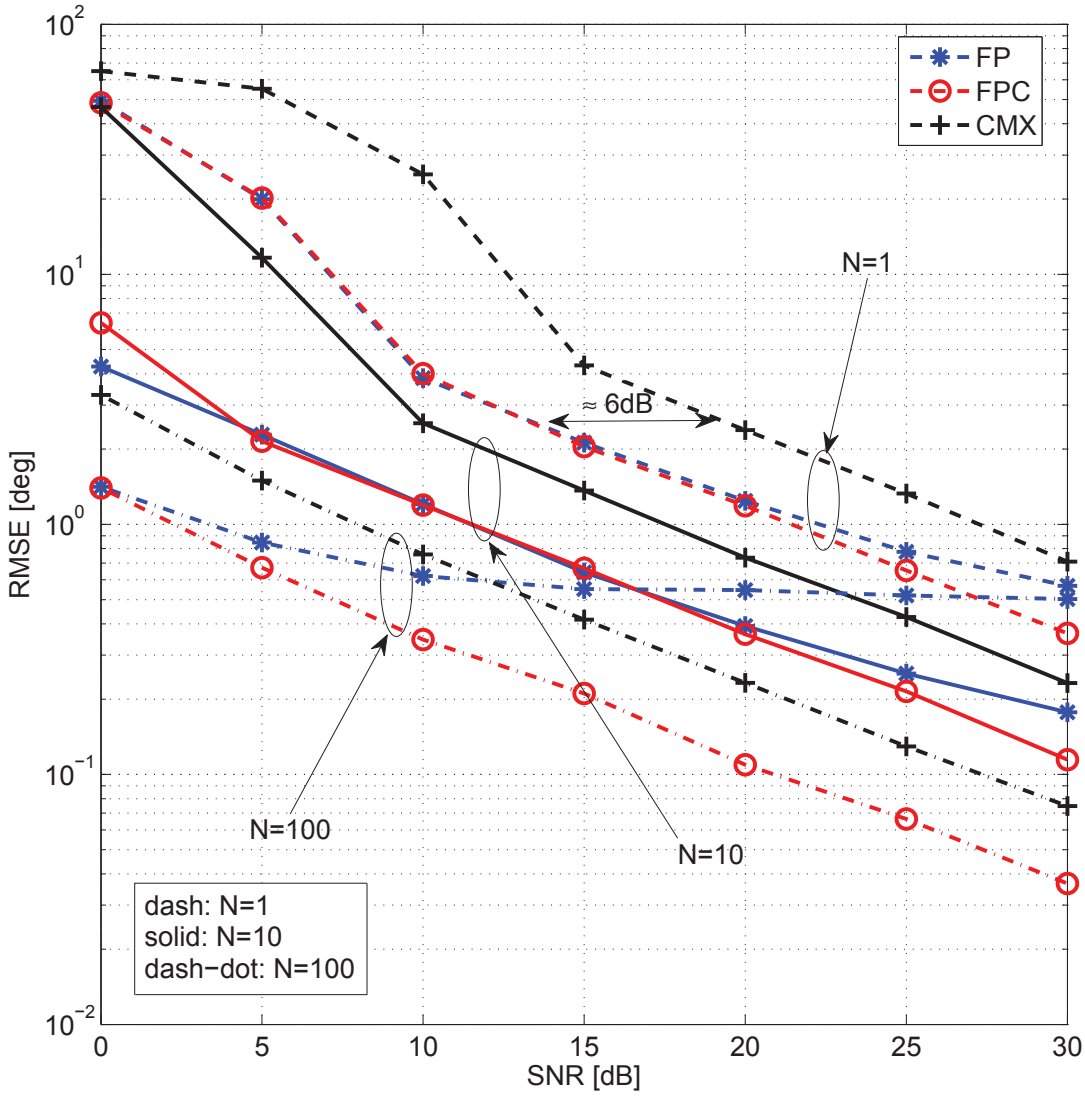

Figure 6.12: RMSE comparison among different architectures as function of the SNR, with the LO impairments.

affect the performance. Obviously, the error floor values depend on the amount of the mutual coupling and I&Q imbalance. Nonetheless, both the impairments should be taken into account.

6.6 Main Findings

We have considered several implementation issues for a direction finding system. Firstly, we have described several single RF FE implementations, and we have compared them in terms of complexity, costs, and non-idealities. We have highlighted that the use of a direct conversion architecture is preferable due to its good trade-off between integration level and

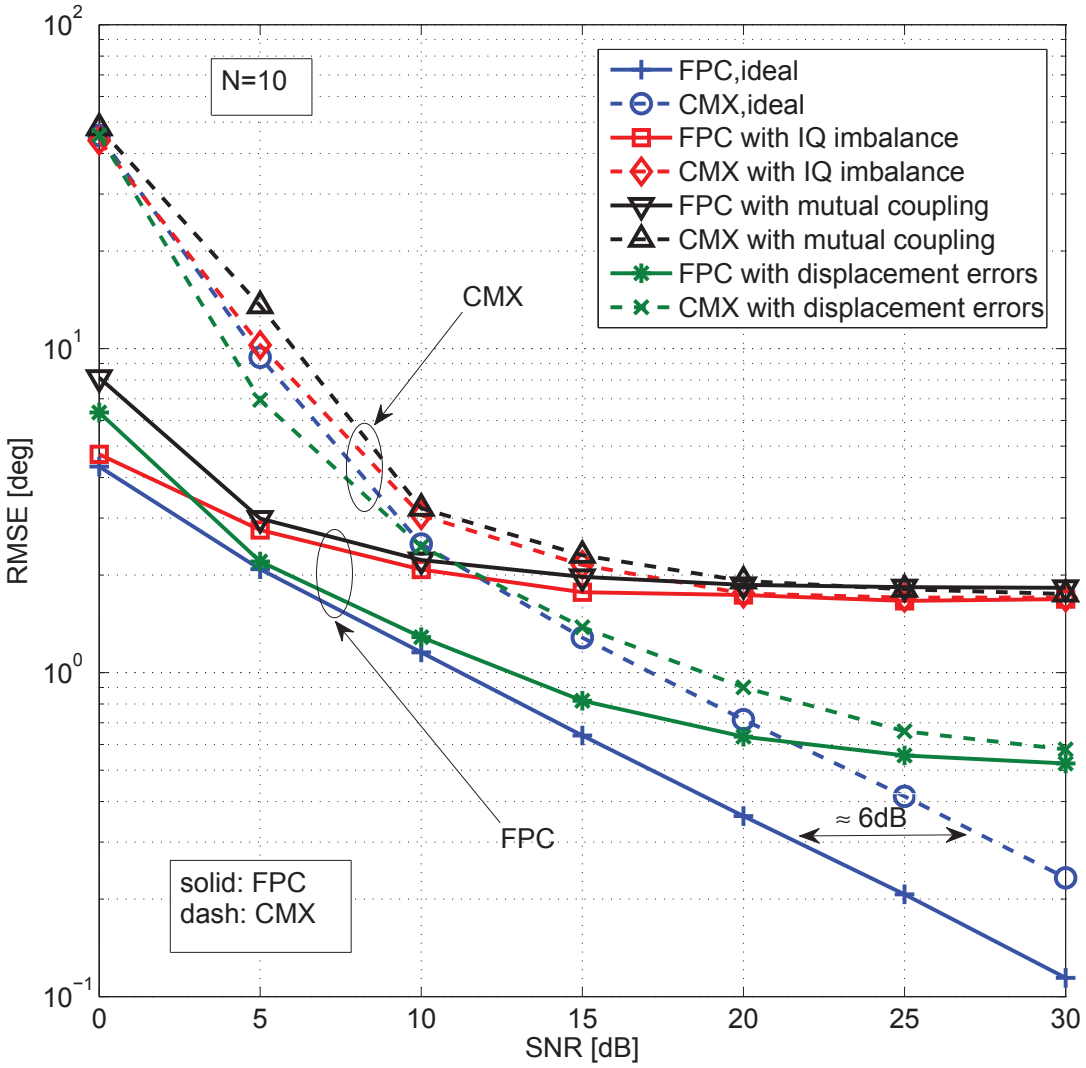

Figure 6.13: RMSE for both the full-parallel coherent and code-multiplexed architectures as function of the SNR, in the presence of the impairments, with $N = 10$.

performance. Successively, we have shown the multiple receiver architectures that can be used for the purpose of the DoA estimation. In this respect, if high SNR is required, a FPC solution is preferable. However, its cost linearly increases with the number of antennas. For this reason, when the application requires many elements, a multiplexed solution can be adopted, even if the performance deteriorates at least by a factor M. In order to counteract the noise floor increase, a hybrid solution can be adopted. The hardware impairments that can affect the performance with the different architectures have been described. In the numerical results we have compared the performance of three architectures, namely, FP, FPC, and CMX. We have shown that the coherent solution reaches the best performance. However, its accuracy is mainly limited by both mutual coupling and I&Q imbalance effects.

Chapter 7

DoA Estimation in Multipath Channels

In the previous chapters, we have deeply investigated the direction of arrival (DoA) estimation problem in the presence of different hardware non idealities. Now, we address a new issue, i.e., the DoA estimation in multipath (MP) channels. We firstly give a general overview on the problem, and then we propose a DoA estimation scheme that overcomes the limitations of the superresolution techniques. Our method exploits the training symbol of a cyclic prefixing (CP) orthogonal frequency division multiplexing (OFDM) communication technique, and we analyze it with different channel parameters.

7.1 Introduction

The MP propagation is a serious problem in DoA estimation. If we consider the superresolution techniques, e.g., Multiple Signal Classification (MUSIC) [16], or Estimation of Signal Parameters Via Rotational Invariance Techniques (ESPRIT) [17], they have a limitation in the number of resolvable signals, i.e., the number of impinging signals has to be lower than the number of antenna elements. Therefore, even if we knew the maximum number of multipath components (MPCs), this would be reasonably high, so the system would need a very large antenna array, increasing size and costs (as described in Chapter 6).

Another great limitation of these techniques regard the capabilities at resolving *coherent* signals[1], as it could occur in MP channels. In fact, it is well known that the superresolution techniques cannot resolve coherent signals directly, but require the use of a pre-processing method, called Spatial Smothing (SS) [21], [22]. This solution, although it allows the DoA estimation of coherent signals, it decreases the effective size of the antenna array, i.e., the number of antenna elements has to be higher than in the case of uncoherent signals.

In this respect, the Joint Angle and Delay Estimation (JADE) algorithm has been presented in [23]. This solution, that aims at estimating DoAs and delays of the MPCs using a collection of space-time channel estimates, can work in cases where the total number of

[1] In [21], coherent signals are defined as fully correlated signals.

impinging signals exceeds the number of antennas. However, like the traditional MUSIC and ESPRIT, it needs to compute an eigendecomposition that is computationally expensive. Other complex algorithms that do not rely on the eigendecomposition have been proposed to deal with the MP propagation [24], [25], [26].

Motivated by these considerations, in this chapter we propose a line-of-sight (LOS) DoA estimation approach based on the first arrival path (FAP) identification. The proposed algorithm is composed by the following steps: a) a coarse synchronization that identifies the start of the transmitted frame; b) a time domain channel estimation; c) a threshold based fine synchronization that accurately selects the FAP; d) a low complexity single source DoA estimation. The above steps are applied to a CP-OFDM transmission technique. CP avoids both inter-symbol interference (ISI) and inter-carrier interference (ICI) if the synchronization error is within the so called *ISI-free zone* of the CP [78], and this allows the correct estimation of the channel impulse response (CIR). The coarse synchronization, the time domain channel estimation, and the fine synchronization are based on the algorithm proposed by Minn et al. in [78] that shows better performance than other synchronization procedures usually considered in the OFDM literature [79]. Finally, the low complexity single source DoA estimator is described in Chapter 3.

Our algorithm overcomes the limitations described above. In fact, it is capable to distinguish between the LOS DoA and a MPC spaced by one sample period. Further, we will show that the proposed technique guarantees good performance also when the LOS DoA is corrupted by a MPC with delay less than one sample period. In this case, when the power of the overlapped MPCs is high, e.g., small indoor environments, we propose to combine the FAP identification with a smooth-MUSIC; this increases the number of required antenna elements and the overall algorithm complexity, but as it will be shown, improves the performance up to Ricean K factor [80] values of $7-8$ dB. Moreover, this method works regardless of the number of antenna (at least two) or the number of impinging signals. Finally, it does not involve an eigendecomposition.

The rest of the chapter is organized as follows. The problem statement is described in Section 7.2. After that, we presents the single-input multiple-output (SIMO) system model, including the CP-OFDM transmission scheme (Section 7.3). Section 7.4 summarizes the coarse and the fine synchronization procedures, the time domain channel estimation, and the DoA estimation. In Section 7.5 we describe the channel model, and how the performance of our method can be improved by using smooth-MUSIC on the FAP. Performance evaluation and simulation results are descibed in Section 7.6. Finally, main findings are provided in Section 7.7.

7.2 Problem Statement

Let us consider a scenario in which a single user transmits the upconverted signal $s(t)e^{j2\pi f_c t}$ (f_c is the carrier frequency) to a base station (BS) equipped with a multiple antenna array with M elements. The transmitted signal undergoes MP propagation, and we can write the (noiseless) RF received signal at the i-th antenna element as

$$x_{RF}^{(i)}(t) = \sum_{l=0}^{L-1} \rho_l s(t - \tau_l^{(i)}) e^{j2\pi f_c (t-\tau_l^{(i)})},\ i \in \{1, .., M\}. \tag{7.1}$$

where ρ_l is the propagation loss of the l-th path (assumed to be equal among the M receivers), while $\tau_l^{(i)} = \tau_{prop,l} + \Delta t^{(i)}(\phi_l)$ is the propagation delay between the trasmitter and the i-th receiver, composed by the delay between the transmitter and the first receiver $\tau_{prop,l}$, and the delay between the first and the i-th receiver due to the non zero DoA ϕ_l that, when a 1-D DoA estimation with linearly equispaced (LES) antenna array is considered, can be written as

$$\Delta t^{(i)}(\phi_l) = \frac{d}{c_0}(i-1)\cos(\phi_l),\ l \in \{0, .., L-1\},\ i \in \{1, .., M\}, \tag{7.2}$$

where d is the interelement distance, while c_0 is the speed of light. At this point, each receiver performs a downconversion so that the baseband signal at the i-th receiver can be expressed as

$$x^{(i)}(t) = \sum_{l=0}^{L-1} \alpha_l s(t - \tau_l^{(i)}) e^{-j2\pi f_c \Delta t^{(i)}(\phi_l) + j\Phi_l},\ i \in \{1, .., M\}, \tag{7.3}$$

where α_l is the resultant complex coefficient due to the propagation loss and the receiver gain, while Φ_l is a phase term that includes the phase $2\pi f_c \tau_{prop,l}$ and the phase of the local oscillator (LO).

It should be noted that until now we have not done any assumption on the transmitted signal $s(t)$, except that the signal can be correctly upconverted to the frequency f_c. Hence, we can define a generic (time invariant) channel response for the i-th antenna link as

$$h^{(i)}(t) = \sum_{l=0}^{L-1} \hat{\alpha}_l^{(i)} \delta(t - \tau_l^{(i)}),\ i \in \{1, .., M\}, \tag{7.4}$$

where

$$\hat{\alpha}_l^{(i)} = |\alpha_l| e^{j\angle\alpha_l} e^{-j\kappa d(i-1)\cos(\phi_l)},\ l \in \{0, .., L-1\},\ i \in \{1, .., M\}. \tag{7.5}$$

The description of the MP complex coefficients as in (7.5) is reasonable with limited angular spreads (ASs) [81], where the AS is the standard deviation of the DoA $\phi_l,\ l \in \{0, .., L-1\}$.

Differently to the CIR shown in (5.1), this channel model includes different cases, that we now analyze in detail.

7.2.1 Narrowband and Wideband Channel Models

As described in Chapter 1, the narrowband hypothesis holds true if $\frac{BW}{f_c} \ll \frac{1}{D}$, where BW is the signal bandwidth, f_c is the carrier frequency, while D is the array aperture in wavelength (in the case of a $\lambda/2$-spaced LES array (λ is the wavelength), $D = \frac{M-1}{2}$). If we consider the difference between the l-th tap delay of the first antenna element and the last, we can write

$$|\tau_l^{(M)} - \tau_l^{(1)}| = \frac{d}{c_0}(M-1)\cos(\phi_l) \leq \frac{d}{c_0}(M-1) = \left.\frac{M-1}{2f_c}\right|_{d=\frac{\lambda}{2}}, \tag{7.6}$$

where d is the interelement distance, c_0 is the speed of light, while ϕ_l is the DoA of the l-th path. Now, we assume that the sampling period of the system is taken according to the Nyquist criteria, i.e., $T = \frac{1}{2BW}$. In this case, rewriting the narrowband hypothesis as $\frac{1}{BW} \gg \frac{M-1}{2f_c}$ and comparing it with (7.6), it is possible to verify that $T > |\tau_l^{(M)} - \tau_l^{(1)}|$, so that the delays $\tau_l^{(i)},\ i \in \{1,..,M\}$ are not distinguishable.

From the above considerations we can deduce the following criteria: the CIR in (7.4) describes a wideband channel model, and it holds true if $T \leq |\tau_l^{(M)} - \tau_l^{(1)}|$; otherwise, if $T > |\tau_l^{(M)} - \tau_l^{(1)}|$, the channel model is narrowband and can be written as

$$h^{(i)}(t) = \sum_{l=0}^{L-1} \hat{\alpha}_l^{(i)} \delta(t - \tau_l),\ i \in \{1,..,M\}. \tag{7.7}$$

Usually, the wideband DoA estimators just exploit the delay differences among the antennas to estimate the DoA. As it can be observed from (7.6), the delay difference is a function of the interelement distance, and the larger the interelement distance, the more accurate the DoA estimation is. Examples of wideband DoA estimator can be found in [82], [83]. These works show that reasonable accuracy can be obtained with large interelement distances that no longer suit the case of co-located antennas, as instead it is reasonable to assume when a single BS with multiple antenna receiver is used. Therefore, the wideband DoA estimation is more suited to a distributed positioning system, e.g., in wireless sensor networks (WSN), or however when multiple BS are used.

Even in the narrowband, as described by the Cramer-Rao bound (CRB) reported in (1.10), the increase of the interelement distance improves the DoA estimation accuracy. However, while in the wideband case the support of (7.6) can be extended without limits, in the narrowband case the increase of d has to be limited. In fact, as shown in Chapter 1, the DoA information resides on the complex coefficient phase that has a limited support, i.e., $[0, 2\pi)$. More precisely, if we want to correctly estimate the DoA, the phase term $\kappa d\cos(\phi_l)$ has to be comprised between $-\pi$ and π because of the periodicity of the cosine function, yielding the constraint

$$\kappa d|\cos(\phi_l)| \leq \pi. \tag{7.8}$$

Now, if we want to correctly resolve the widest possible DoA range, i.e., $\phi_l \in [-\frac{\pi}{2}, \frac{\pi}{2}]$, the constraint becomes

$$d \leq \frac{\lambda}{2}. \tag{7.9}$$

This criteria is also called *spatial Nyquist criteria*, i.e., a signal with wavelength λ can be correctly resolved if it is "spatially sampled" using an antenna array with interelement distance that is at least two times the wavelength of the signal. For this reason, narrowband DoA estimators are more suited to be implemented using a multiple antenna receiver with co-located antennas, that is the main topic of this thesis.

Now, we describe our method that can be used in a narrowband scenario, e.g., when the industrial, scientific and medical (ISM) bands at 2.4 and 5.8 GHz are considered (these bands are covered by the system described in 2).

7.3 System Model Description

Let us assume a SIMO system model as in Fig. 1.3, where the multiple antenna receiver is equipped with a LES antenna array with M elements spaced by $\lambda/2$. In the case of frequency selective MP fading channel, whose CIR is shown in (7.7), assuming that the LOS component is always present, the signal at the input of the i-th receiver (with phase calibrated array, and in the absence of carrier frequency offset and sampling clock errors) can be written as

$$x^{(i)}(t) = \sum_{l=0}^{L-1} \hat{\alpha}_l^{(i)} s(t - \tau_l) + w^{(i)}(t),\ i \in \{1, .., M\}. \tag{7.10}$$

To proceed, it is necessary to estimate the complex channel coefficients $\hat{\alpha}_0^{(i)},\ i \in \{1, .., M\}$ from the signal in (7.10) that brings the LOS DoA information, as shown in (7.5). Then, it will be possible to apply the low complexity DoA estimator proposed in Chapter 3, i.e.,

$$\begin{aligned} z &= \frac{1}{M-1} \sum_{i=1}^{M-1} \tilde{\alpha}_0^{(i)} \cdot \tilde{\alpha}_0^{(i+1)^*}, \\ \tilde{\phi}_0 &= -\arccos\left(\frac{\angle z}{\kappa d}\right), \end{aligned} \tag{7.11}$$

where $\tilde{\alpha}_0^{(i)},\ i \in \{1, .., M\}$ is the estimate of the LOS complex channel coefficient.

To obtain the DoA estimation, we propose to perform the following steps:

- a coarse synchronization, in order to identify the beginning of the signal $s(t)$,
- a time domain channel estimation,
- a threshold-based fine synchronization, to estimate the position of the FAP.

These steps are implemented following the synchronization algorithm proposed by Minn et al. in [78]. We consider a CP-OFDM system since is one of the most used transmission technique. Further, differently to the zero padding (ZP) OFDM, if the coarse synchronization introduces a timing offset $\epsilon \in \{-\mu+\tau_L, -\mu+\tau_L+1, .., 0\}$ (the ISI-free zone), where μ is the CP length, the orthogonality among the subcarriers will not be destroyed by the introduction of ISI and ICI [84].

7.3.1 CP-OFDM Transmission Scheme

In Fig. 7.1, the main blocks of a CP-OFDM transmission scheme (baseband) are depicted. In a SIMO system, the transmitter is shared, while each output channel, i.e., each receiver, has to deal with its own channel, as in (7.10).

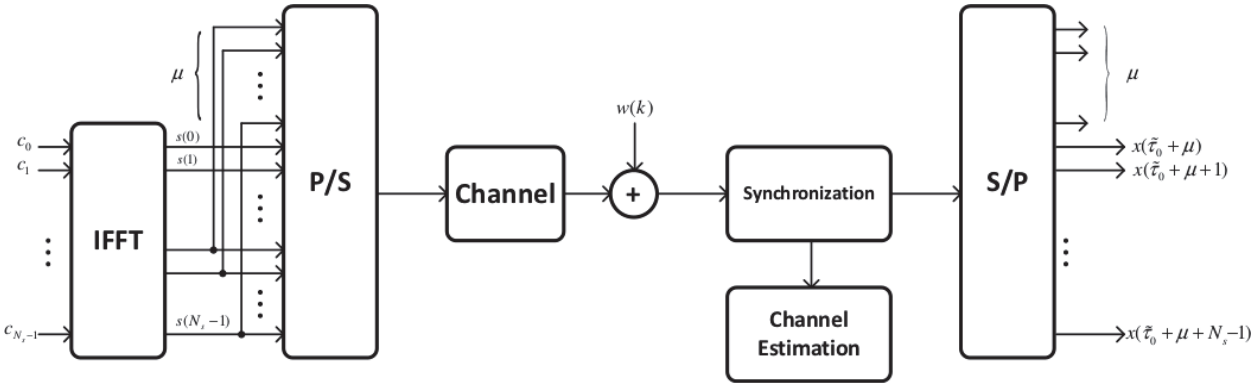

Figure 7.1: Main blocks of a CP-OFDM transmission scheme.

In the discrete time domain, the samples of the transmitted OFDM symbol at the output of the parallel-to-serial (P/S) block, assuming ideal Nyquist pulse shaping, can be written as

$$s(k) = \frac{N_s}{N_s+\mu} \sum_{n=0}^{N_s-1} c_n e^{j2\pi \frac{kn}{N_s}}, \; k \in \{-\mu, .., N_s-1\}, \tag{7.12}$$

where $c_n, \; n \in \{0, .., N_s-1\}$ are the subcarrier symbols, N_s is both the number of subcarriers and the number of the inverse fast Fourier transform (IFFT) points, while μ is the CP length.

These samples are convoluted with a specific CIR, and the results is corrupted by the additive noise. At the receiver, a synchronization block allows the recovering of the OFDM symbol start instant, in order to neglect the CP and to successively apply the fast Fourier transform (FFT) and an equalization process (the last two blocks are not shown in Fig. 7.1 since in this paper we do not consider the data recovery problem). As suggested in [78], the channel estimation step can be performed in the time domain on the received data samples. Nevertheless, it should be noted that the CP should be larger than the maximum dispersion of the channel $\tau_L - \tau_0$.

7.4 Synchronization, Channel Estimation, and DoA Estimation

The timing synchronization unit has to determine the starting point of the FFT window, that corresponds to the FAP delay τ_0 (plus the CP length μ).

Minn et al. [78] have proposed to transmit an OFDM training symbol with $Q = 4$ (or another power of two) identical portions each comprising $N_q = N_s/Q$ symbols. Each portion corresponds to the FFT of a quarter length Golay complementary sequence. We have extended Minn's timing metric to the case of multiple receivers, by simply averaging the correlation sequences $P^{(i)}(m),\ i \in \{1, .., M\}$ and the symbol energies $R^{(i)}(m),\ i \in \{1, .., M\}$. After the analog-to-digital conversion, the timing metric to be maximized can be expressed as

$$\Lambda_c(m) = \left(\frac{Q}{Q-1} \frac{|\bar{P}(m)|}{\bar{R}(m)} \right)^2, \tag{7.13}$$

where $\bar{P}(m) = \frac{1}{M} \sum_{i=1}^{M} P^{(i)}(m)$ and $\bar{R}(m) = \frac{1}{M} \sum_{i=1}^{M} R^{(i)}(m)$, while

$$\begin{aligned} P^{(i)}(m) &= \sum_{q=0}^{Q-2} p(q)p(q+1) \sum_{n=0}^{N_q-1} r^{(i)*}(m + qN_q + n) \\ &\quad \cdot r^{(i)}(m + (q+1)N_q + n), \\ R^{(i)}(m) &= \sum_{q=0}^{Q-1} \sum_{n=0}^{N_q-1} |r^{(i)}(m + n + qN_q)|^2, \end{aligned} \tag{7.14}$$

where $p(q),\ q \in \{0, .., Q-1\}$ denotes the sign of the repeated part of the training symbol. According to [78], we have adopted $Q = 4$ and $p = [-1, 1, -1, -1]$.

7.4.1 Coarse Synchronization

The coarse timing estimate can be obtained as

$$\tau_c = \arg \max_{m \in \mathbb{Z}} \{\Lambda_c(m)\} - \lambda_c, \tag{7.15}$$

where λ_c is a preadvancement that should be chosen higher than the (designed) mean shift of the timing point caused by the channel dispersion. In this way, the coarse timing estimate will be in the ISI-free part of the cyclic prefix.

7.4.2 Channel Estimation

The i-th maximum likelihood (ML) channel response estimate can be obtained as

$$\tilde{\mathbf{h}}^{(i)} = \left(\mathbf{S}^H \mathbf{S}\right)^{-1} \mathbf{S}^H \cdot \mathbf{r}^{(i)}(\tau_c),\ i \in \{1, .., M\}, \tag{7.16}$$

where $\tilde{\mathbf{h}}^{(i)}$ is the μ-length column vector that contains the complex path gains of the channel, while

$$\mathbf{S} = \begin{bmatrix} s(0) & s(-1) & \dots & s(-\mu+1) \\ s(1) & s(0) & \dots & s(-\mu+2) \\ \ddots & & & \\ s(N_s-1) & s(N_s-2) & \dots & s(N_s-\mu) \end{bmatrix} \tag{7.17}$$

is the matrix of the transmitted training symbol (including the cyclic prefix), and

$$\begin{aligned} &\mathbf{r}^{(i)}(\tau_c) \\ &= [r^{(i)}(\tau_c+\mu)\ r^{(i)}(\tau_c+\mu+1)\ ..\ r^{(i)}(\tau_c+\mu+N_s-1)]^T \end{aligned} \tag{7.18}$$

is the column vector of the received samples (excluding the cyclic prefix) in the window from $\tau_c+\mu$ to $\tau_c+\mu+N_s-1$.

7.4.3 Fine Synchronization

The FAP delay can be found as in the following. First, we denote with χ the channel response vector obtained by averaging each entry of the vector $\tilde{\mathbf{h}}^{(i)}$, in module, over the antenna elements, i.e., $\chi(m) = \frac{1}{M}\sum_{i=1}^{M}|\tilde{h}^{(i)}(m)|$. Secondly, the strongest tap gain χ_{max} is found as

$$\chi_{max} = \arg \max_{m\in\{0,..\mu-1\}} \{\chi(m)\}. \tag{7.19}$$

Then, the fine timing τ_f is given by

$$\tau_f = \arg \max_{m\in\{0,..,\mu-K\}} \{E_h(m)\}, \tag{7.20}$$

where

$$E_h(m) = \begin{cases} \sum_{k=0}^{\mu-1}\chi(m+k)^2, & \text{if } \chi(m) > \eta\cdot\chi_{max}, \\ 0, & \text{otherwise} \end{cases} \tag{7.21}$$

is the channel energy estimate contained in a window of length μ starting from the tap m if the channel energy estimate of the tap m is greater than the threshold η.

At this point, the FAP delay estimation $\tilde{\tau_0}$ can be found as

$$\tilde{\tau_0} = \tau_c + \tau_f. \tag{7.22}$$

It should be noted that in [78] the FAP delay estimation is furtherly preadvanced but we have found that, with our parameter setup, (7.22) minimizes the timing error.

7.4.4 DoA Estimation

The LOS DoA can be found by applying (7.11) with

$$z = \frac{1}{M-1} \sum_{i=1}^{M-1} \tilde{h}^{(i)}(\tau_f) \tilde{h}^{(i+1)^*}(\tau_f). \tag{7.23}$$

It should be noted that the DoA estimate can be improved by using L_{tr} CIR estimates, obtained by transmitting L_{tr} OFDM training symbols, and averaging z as it is done in Chapter 3.

7.5 Channel Model and DoA Estimation Improvement

We assume a single cluster channel model as in (7.7), where the FAP always comprises the LOS component. The total number of MPCs, $L-1$, is Poisson distributed, i.e., $L-1 \sim \mathcal{P}(\Lambda)$, where Λ is the normalized rms delay spread. Each MPCs is associated to a specific DoA ϕ_l as proposed in [68], so that the complex channel coefficient $\alpha_l^{(i)}$, in the case of a $\lambda/2$-spaced LES array, can be written as

$$\hat{\alpha}_l^{(i)} = \alpha_l e^{-j\pi(i-1)\cos(\phi_l)},\ l \in \{0, .., L-1\},\ i \in \{1, .., M\}. \tag{7.24}$$

The amplitude of the l-th MPC, $|\alpha_l|$, is modeled as a Rayleigh distributed random variable with statistic power that follows an exponential decay profile, i.e., $\Omega_l \sim e^{-\tau_l/\Gamma}$, with Γ the power-delay time constant, while its phase shift, $\angle\alpha_l$, is uniformly distributed. Furthermore, the DoAs $\phi_l,\ l > 0$ are Laplace distributed, with mean ϕ_0 and standard deviation AS (in the following we refer to it as angular spread).

We consider the path delays τ_l to be normalized w.r.t. the sample period. The FAP delay τ_0 is uniformly distributed within the range $[0, N-1]$. The interarrival times $\tau_l - \tau_0$ are exponentially distributed with parameter Λ.

It is possible that L' MPCs have an equal delay of the LOS component. These L' non-LOS (NLOS) components have power $\Omega_l,\ l \in \{1, .., L'\}$. The ratio K between the LOS power Ω_0 and the total power of these NLOS components is defined as

$$K = \frac{\Omega_0}{\sum_{l=1}^{L'} \Omega_l}. \tag{7.25}$$

It is worth noting that, when the factor K is low, the performance of the DoA estimator in (7.11) can be severely corrupted. In this case, we propose an improvement of the DoA estimator based on smooth-MUSIC [21]. In fact, when a NLOS component overlaps the LOS, we have to deal with a DoA estimation problem of coherent sources, and the classical MUSIC (or root-MUSIC) fails.

7.5.1 Smooth-MUSIC

In Chapter 3, we have described the root-MUSIC algorithm applied to a single source scenario. It can be easily extended to the case of multiple sources, e.g., N_t sources, by considering, after the eigendecomposition of the correlation matrix $\mathbf{R}$, the partition of the eigenvector matrix $\mathbf{Q}$ associated to the $M - N_t$ eigenvalues, instead of to the $M - 1$ eigenvalues, and computing the $M - N_t$ roots of the polynomial with coefficients $C_l,\ l \in \{0, .., M-1\}$. However, if two or more sources are correlated, the correlation matrix $\mathbf{R}$ is singular, and only the *incoherent* wavefronts will be resolved [21]. The spatial smooth-MUSIC pre-processing technique allows the recovering of the non singularity property of the covariance matrix, even when the signals are coherent.

In smooth-MUSIC, the M elements of the antenna array are subdivided into P overlapping subarrays, each with M' elements, e.g., the first subarray would include elements 1 through M', the second elements 2 through $M'+1$, etc. Therefore, $P = M - M' + 1$. Using the data from each subarray, P correlation matrix $\mathbf{R}_p,\ p \in \{1, .., P\}$ can be estimated, each of dimension $M' \times M'$. The MUSIC algorithm (we will use the root-MUSIC described in 3) then continues using the smoothed correlation matrix

$$\mathbf{R}_{\text{smooth}} = \frac{1}{P} \sum_{p=1}^{P} \mathbf{R}_p. \tag{7.26}$$

As also highlighted in the introduction, the effective size of the array decreases when smooth-MUSIC is applied. In fact, if we have $L'+1$ coherent sources, the minimum number of antenna elements needed is $M = 2(L'+1)$.

7.6 Numerical Results

The performance of the proposed algorithm has been investigated by simulations. In particular, we have analyzed the root mean-squared error (RMSE) obtained by the DoA estimator and defined as

$$\text{RMSE} = \sqrt{E\left\{\left(\phi_0 - \tilde{\phi}_0\right)^2\right\}}. \tag{7.27}$$

The CP-OFDM parameters that have been used are as follows: $N_s = 64$, CP length $\mu = 16$. The coarse synchronization pre-advancement is chosen as $\lambda_c = 10$. For what the channel model is concerned, we have considered $\phi_0 = 30$ deg and, where not specified, $\Gamma = 4$. Furthermore, the number of antennas is $M = 4$.

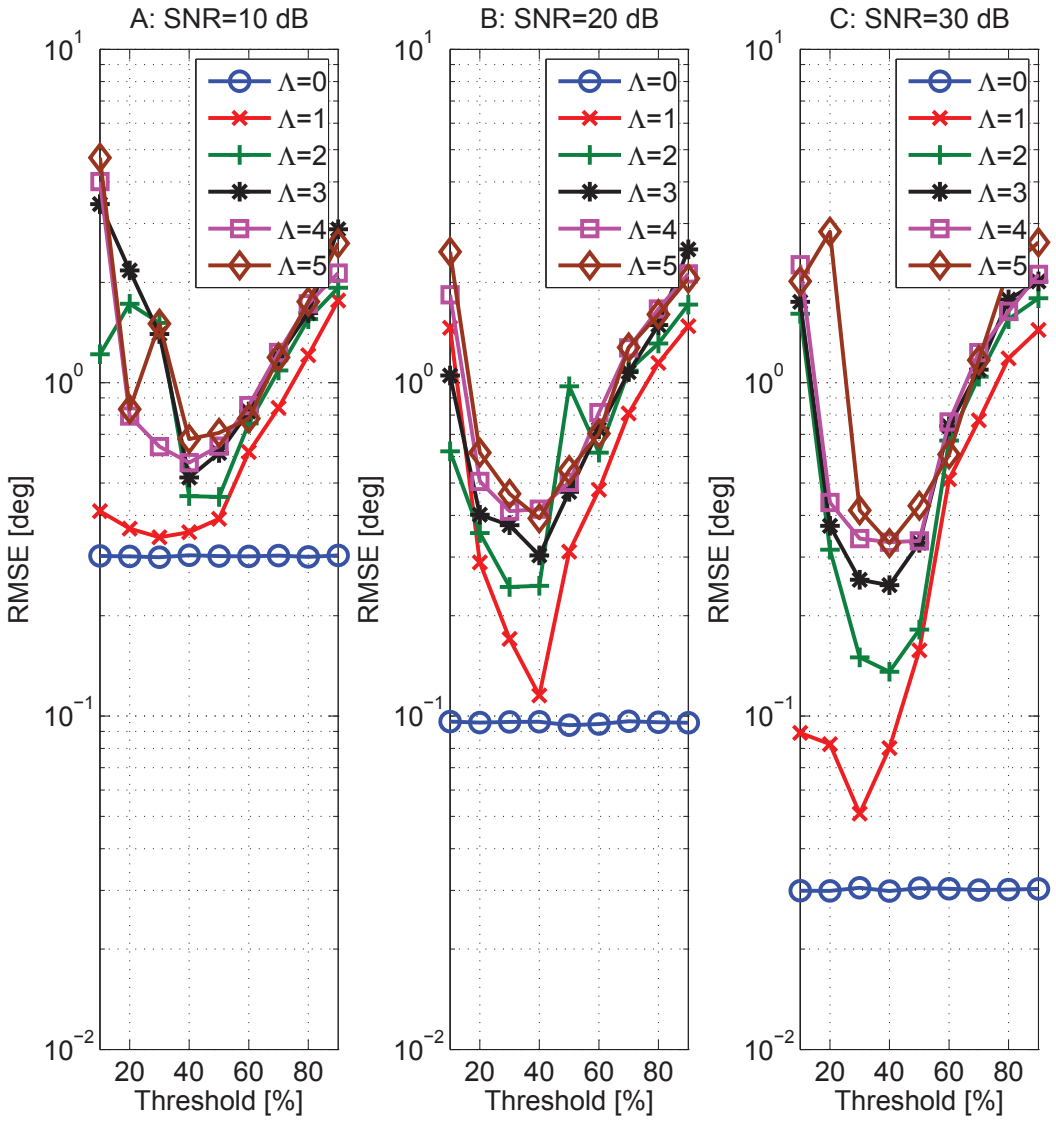

Figure 7.2: RMSE as function of the threshold η in percentage, with AS= 5 deg, and $K = \infty$. (A): SNR= 10 dB. (B): SNR= 20 dB. (C): SNR= 30 dB.

7.6.1 Choice of the Threshold

In Fig. 7.2 we show the performance as function of the threshold η expressed in percentage, with three different SNRs, and $K = \infty$. As it can be observed, in the three cases a good choice of the threshold could be $\eta = 0.4$, and this value will be considered in the following.

7.6.2 Scenario with $K = \infty$

In Fig. 7.3 we show the performance as function of the SNR and the rms delay spread Λ, with $K = \infty$, in the cases of ideal synchronization and by applying the synchronization herein proposed. It should be noted that, in the case of ideal channel ($\Lambda = 0$), the ideal

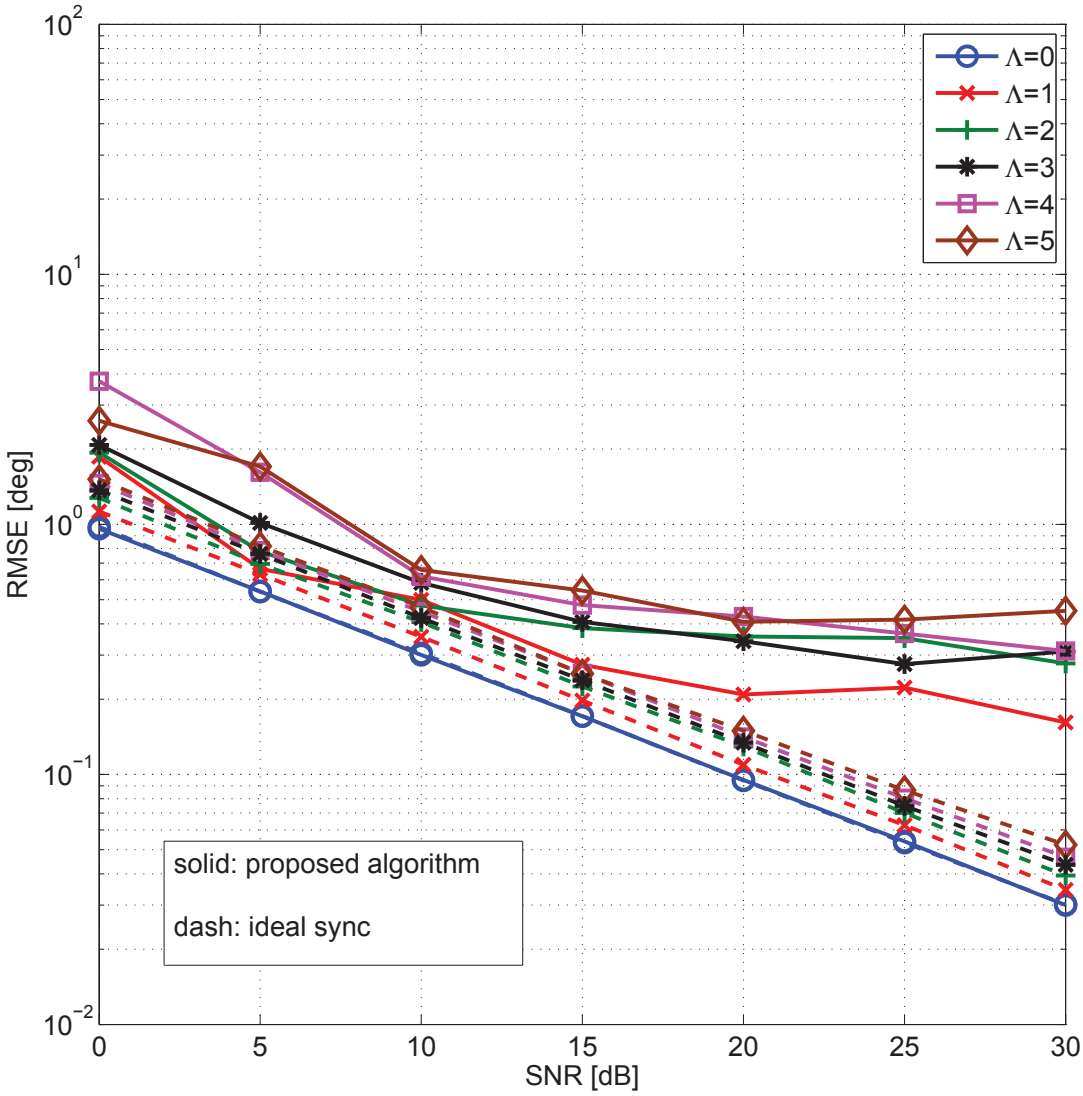

Figure 7.3: RMSE as function of both the SNR and the rms delay spread Λ, with AS= 5 deg.

synchronization curve and the one obtained by applying the proposed algorithm practically overlap, except for low SNRs. If we consider the ideal synchronization, we can observe a slight deterioration of performance with the increase of Λ. This behaviour is due to the decreasing of the total power associated to the LOS path when the number of the MPCs increases. When the synchronization algorithm is performed, with higher SNRs the performance curves reach an error floor due to the synchronization error that increases with the increase of Λ. However, in the worst case, we can apreciate the robustness of the proposed solution, that shows an error floor lower than 1 deg.

In Fig. 7.4 we show the performance as function of the channel parameters Λ, i.e., the normalized rms delay spread, and Γ, i.e., the channel power-delay time constant, with AS $= 5$

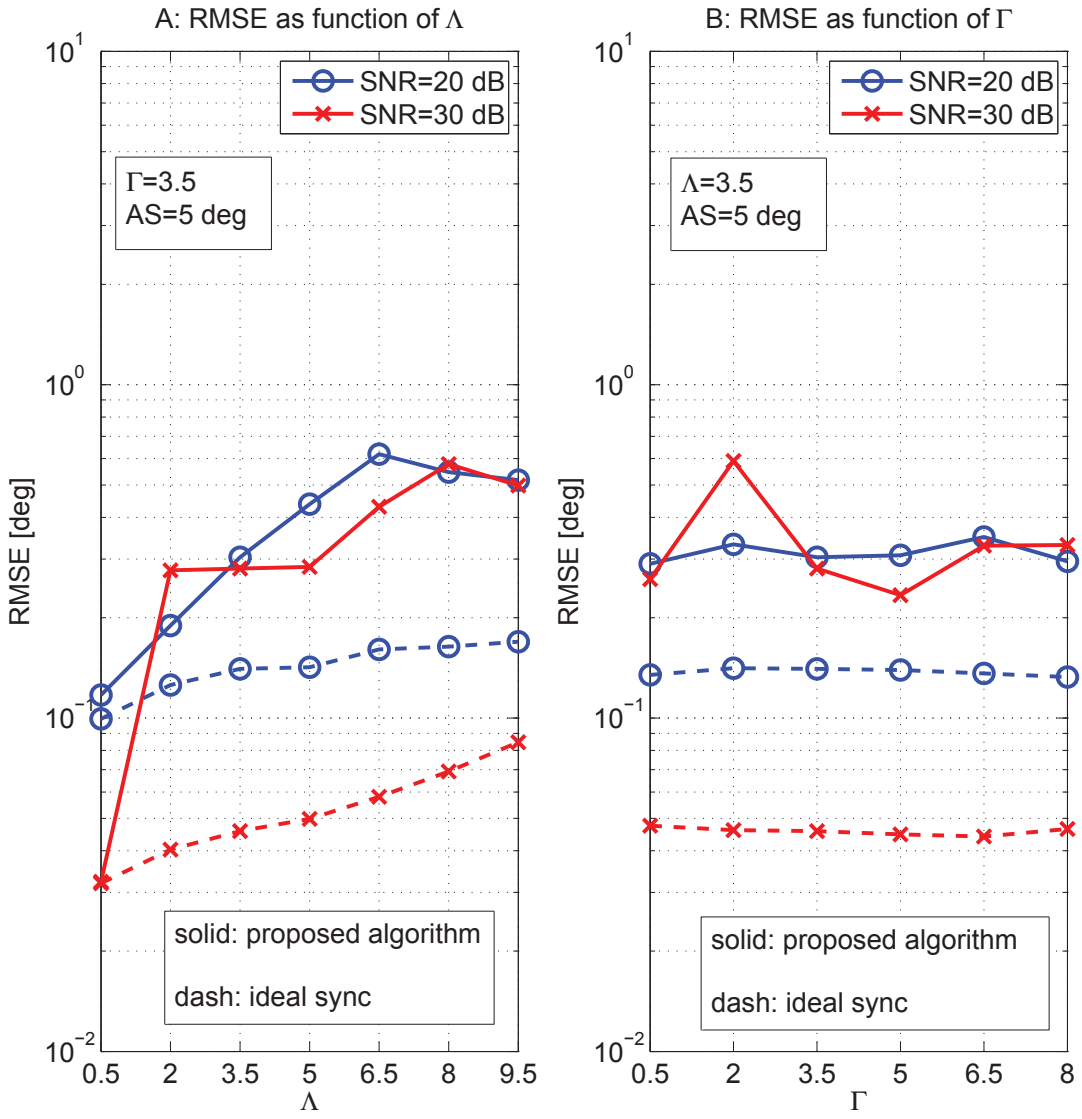

Figure 7.4: RMSE as function of the the channel parameters Λ (normalized rms delay spread) and Γ (channel power-delay time constant), AS $= 5$ deg, SNR$= \{20, 30\}$ dB, and $K = \infty$. (A): RMSE as function of Λ. (B): RMSE as function of Γ.

deg, SNR$= \{20, 30\}$ dB, and $K = \infty$. We can firstly observe in Fig. 7.4.A that the RMSE increases with the increase of Λ for both the ideal synchronization and the proposed method, as also observed in Fig. 7.3. In Fig. 7.4.B, instead, we figure out that the increase of Γ does not affect significantly the algorithm performance.

In Fig. 7.5 the performance of the algorithm is tested for different angular spread AS, with $\Lambda = 4$ and $K = \infty$. It can be observed that the performance deteriorates with the increase of the angular spread. However, with AS$=$ 20 deg, the error floor at the higher SNRs is approximately 1 deg.

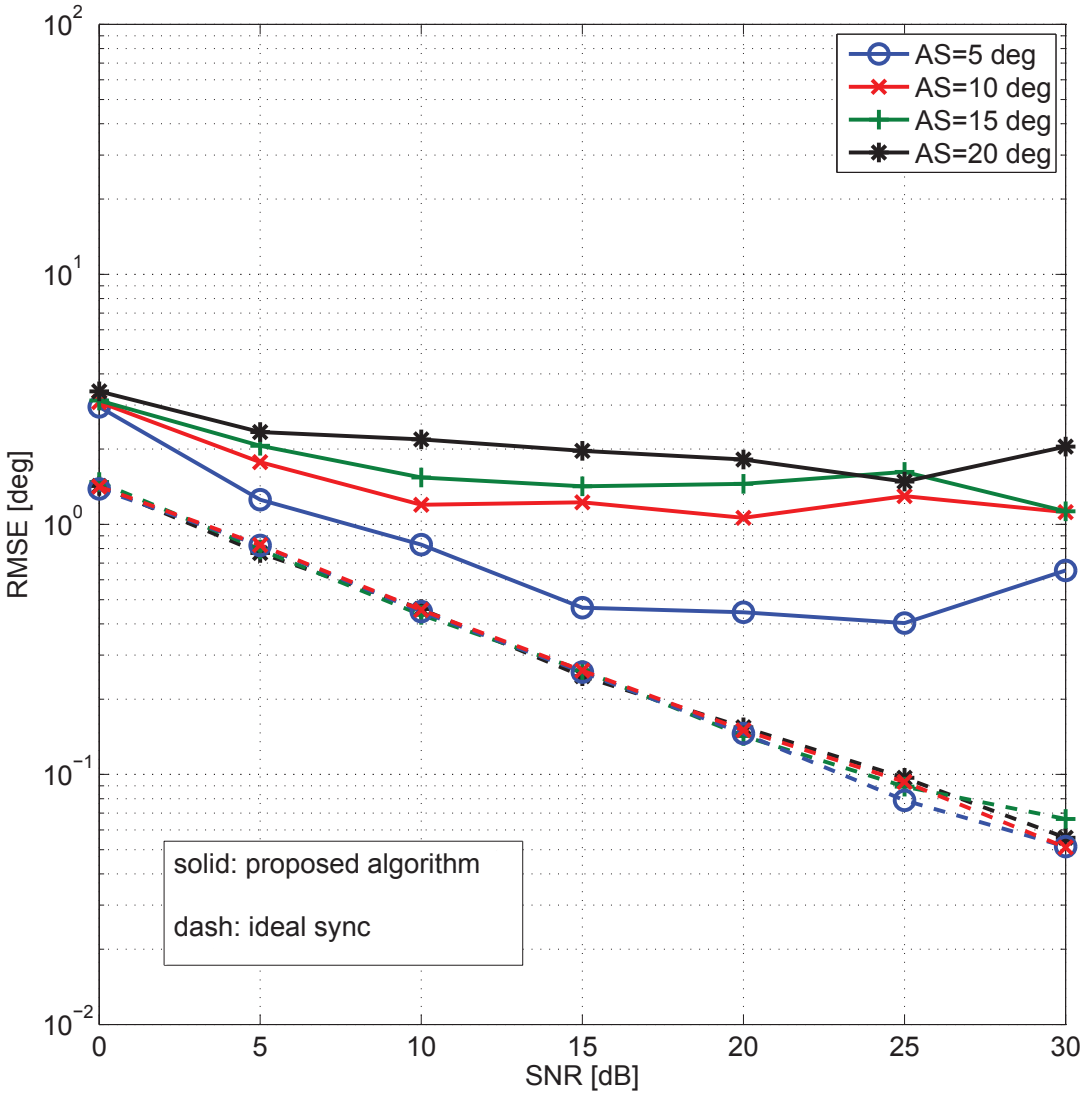

Figure 7.5: RMSE as function of both the SNR and the angular spread AS, with $\Lambda = 4$ and $K = \infty$.

7.6.3 Scenario with NLOS overlapping LOS component

In Fig. 7.6 we show the performance of the system with different values of K, i.e., when NLOS paths may overlap with the LOS, applying our method with the DoA estimator in (7.11), and with the smooth-MUSIC described in Section 7.5.1 ($P = 2$). As expected, the performance degrades with the decrease of K. However, we have observed acceptable error floors (below 1 deg) for values of K higher than 5 dB. Furthermore, our method with smooth-MUSIC works better than the DoA estimator in (7.11) up to $K = 10$ dB. For higher values, the proposed DoA estimator outperforms smooth-MUSIC. Therefore, if the channel manifests these values of K, our DoA estimator is preferable because has lower RMSE and

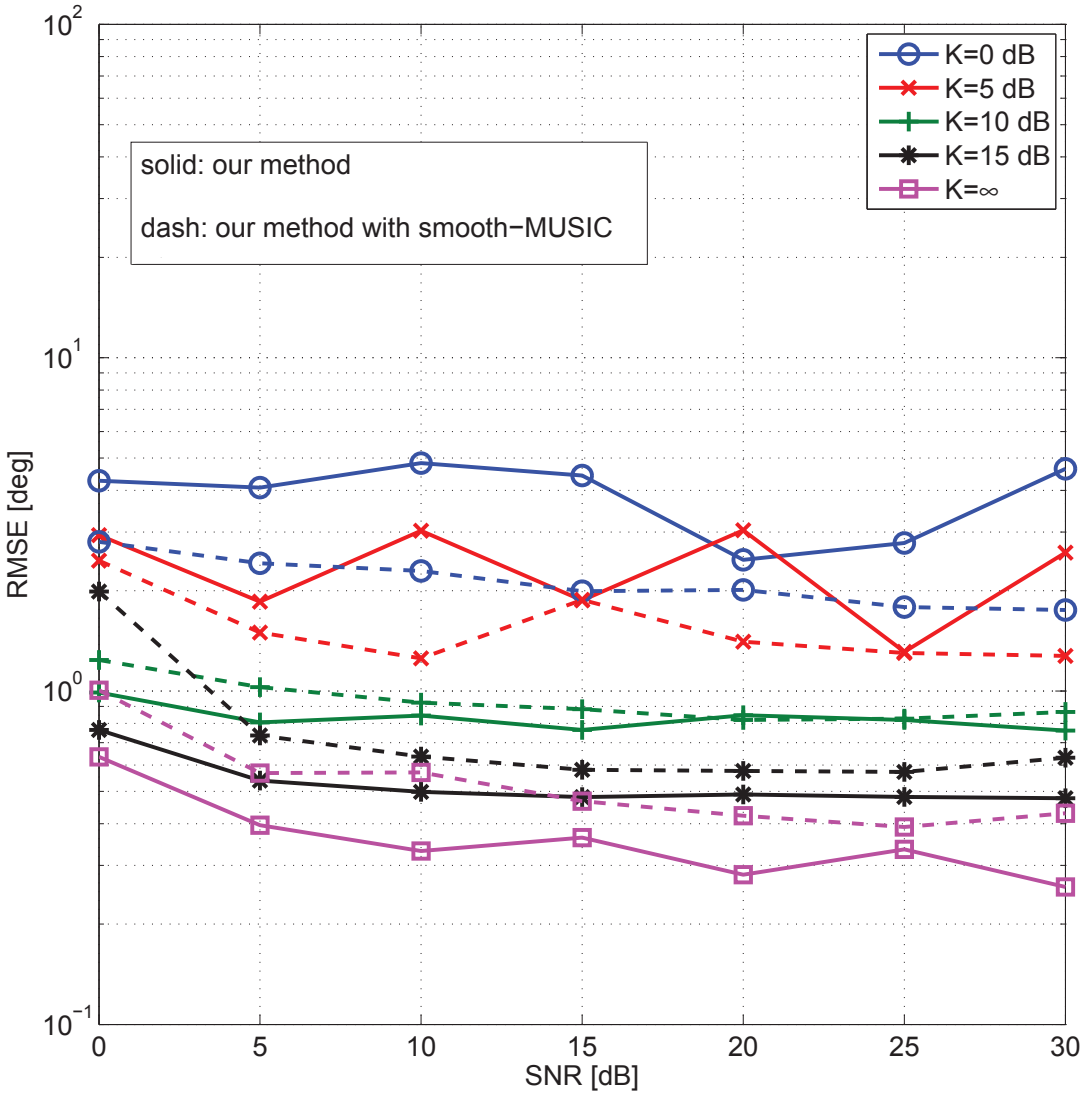

Figure 7.6: RMSE as function of both the SNR and the factor K, with $\Lambda = 4$, AS= 5 deg, and applying our method with the DoA estimator in (7.11) and with the smooth-MUSIC ($P = 2$).

also lower complexity. This is also confirmed by Fig. 7.7, where the performance of both our DoA estimator and smooth-MUSIC is shown as function of the factor K, with $\Lambda = 4$, SNR= $\{20, 30\}$ dB, and with different angular spread AS. Interestingly, the performance curve of our DoA estimator approaches the one of smooth-MUSIC at approximately $K = 7$ dB for both AS= 5 and AS= 20 deg, while the use of smooth-MUSIC is preferable when the angular spread is larger.

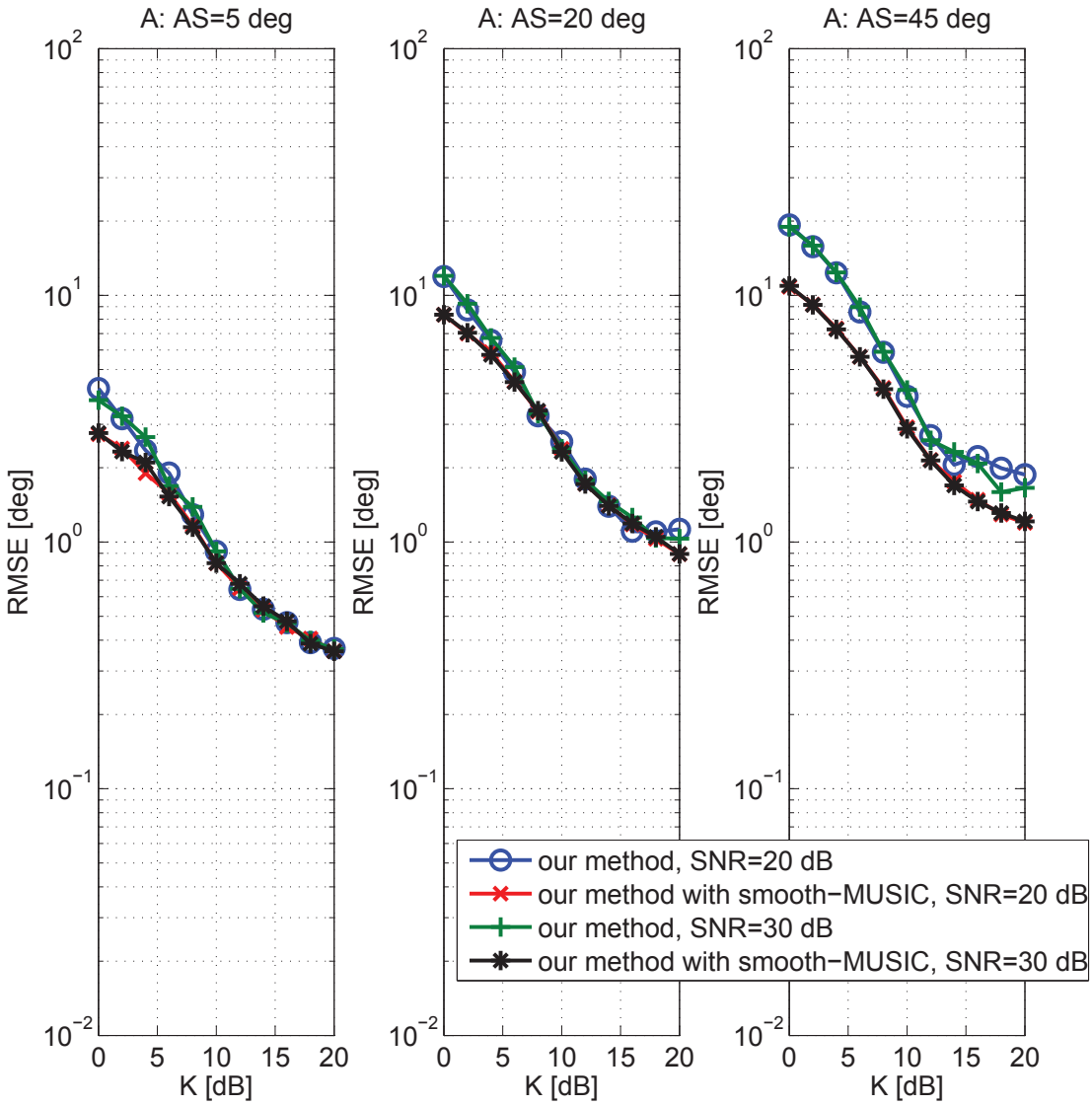

Figure 7.7: RMSE as function of the factor K, with $\Lambda = 4$, SNR= $\{20, 30\}$ dB, and applying our method with the DoA estimator in (7.11) and with the smooth-MUSIC ($P = 2$). (A): AS= 5 deg. (B): AS= 20 deg. (C): AS= 45 deg.

7.7 Main Findings

In this chapter, a DoA estimation algorithm for frequency selective channels is proposed. This method exploits the CP-OFDM transmission scheme, and performs a coarse synchronization to locate the OFDM symbol start, a channel estimation, and a threshold-based fine synchronization that exactly locates the first arrival path (FAP). These steps are included into the synchronization algorithm proposed by Minn et al. [78], whose timing metrics have been modified to comprise the case of a multiple antenna receiver. Once we have located the FAP component, a single source DoA estimator algorithm can be used. Several numeri-

cal results have confirmed the robustness of this method, also when LOS and NLOS paths overlap. In this case, when the factor K is lower than approximately 7 dB and the AS is limited, we have proposed to use our method with smooth-MUSIC, while for higher values of K we have shown that our DoA estimator (that has lower complexity than smooth-MUSIC) exhibits better performance.

Chapter 8

Conclusions

In this thesis, we have addressed the problem of direction of arrival (DoA) estimation for radio positioning systems. In particular, we have considered two main issues: the first is the effect of hardware impairments on the final performance. In this respect, we have firstly analyzed the simplest multiple antenna receiver architecture, the full-parallel (FP) architecture, i.e., when the multiple antenna receiver is composed by many independent (and uncoherent) single antenna receivers, providing a system model that can be used when DoA estimation has to be addressed. We have investigated the performance of this system, in terms of root mean squared error (RMSE) of the estimated DoA, both theoretically and with experimental measurements, when a simple correlation algorithm is used. We have compared it with the root-MUSIC method. Since this kind of architecture needs to be pre-calibrated, at least in terms of phase offsets (POs), we have proposed a new calibration method. Finally, we have analyzed other possible multiple antenna receiver architectures, and we have shown that other hardware impairments such as in-phase and in-quadrature (I&Q) imbalance can limit the DoA estimation performance, even if it is not usually considered in the literature.

The second issue that we have dealt with is the problem of DoA estimation in multipath channels. We have proposed a novel method that relies on the training symbol of a cyclic prefixing (CP) orthogonal frequency division multiplexing (OFDM) system, a modulation technique largerly used in the communication standards. The proposed method identifies the line-of-sight (LOS) path that carries the DoA information, and applies the simple correlation algorithm presented in the first part of this thesis.

The main findings are summarized in the following.

8.1 Hardware Impairments Characterization

The measurement activities done on the hardware platform have revealed that the major impairments are the direct current (DC) offset, the carrier frequency offsets (CFOs), the phase noise (PN) and the different phases among the receiver signals that can be introduced

by both the time delays of unequal cable connections between the array elements, and the use of local oscillators (LOs) that are not co-phased. We have found that the I&Q gain mismatch as well as the sampling time offsets introduced by the ADCs are of negligible entity in our application context.

8.2 DoA Estimation Algorithm Comparison

We have presented an algorithm for 2D-DoA estimation with 3D L-shaped arrays, considering a system model that comprises the hardware impairments previously found. The proposed estimation algorithm is straightforward and compensates the CFOs via differential signal combining, i.e., a correlation. The performance of the algorithm has been studied firstly via simulations for several system configurations and parameter setups. Furthermore, a comparison with the well-known root-MUSIC algorithm is performed. The results have highlighted the robustness for a wide range of angles and SNRs, and that our method performs as well as the root-MUSIC in the case of single source. Spatial and temporal averaging increases the noise immunity of the algorithm. However, while spatial averaging is always beneficial, the temporal averaging window length has to be selected according to the operating SNR in the presence of distinct CFOs between the RF receivers of distinct antenna elements.

The effects of DC offset and PN are also considered. It is shown that DC offset determines an error floor in the RMSE curves. Finally, it is shown that a PO calibration can be done using a local reference signal. It is beneficial to compensate the phase differences of the LOs that comprise a contribution due to the slowly time variant PN process.

This analysis has been validated also via experimental measurements done with the WiPLi Lab wireless testbed in an anechoic chamber, using the 1D release of the DoA estimation algorithm. The results have demonstrated that different temporally correlated PNs among the receivers limit the performance when the number of samples used for averaging increases.

8.3 Array Calibration

We have considered the array calibration problem when PO, CFO, and PN occur among the array signals. We have proposed a novel technique for the calibration of the antenna array system that relies on the use of a particular antenna array which allows the estimation of the PO differences of the array. The array comprises a common antenna which brings the same signal to each receiver. After the calibration step is performed, analog switches can select the antennas for the DoA estimation. We have shown that the calibration method performance does not degrade in the case of a MP channel.

This calibration technique works with either equal CFOs or different CFOs among the receivers. To better address the latter case, we have proposed another method which firstly

estimates the CFO differences and then it performs compensation. The analisys has revealed that the method without CFO compensation works better at low SNRs while at high SNRs it exhibits an error floor. Consequently, at high SNRs it is beneficial to perform CFO compensation.

Another important issue is the effect of the PN. The PO compensation method can mitigate the effects of PN depending on its spectrum, i.e., if it is slowly time variant.

8.4 Multiple Antenna Receiver Architectures

We have investigated several implementation issues for a direction finding (DF) system. Firstly, we have described several single RF front-end (FE) implementations, and we have compared them in terms of complexity, costs, and non-idealities. We have highlighted that the use of a direct conversion architecture is preferable due to its good trade-off between integration level and performance. Successively, we have discussed the multiple receiver architectures that can be used for the purpose of the DoA estimation. In this respect, if high SNR is required, a full-parallel coherent (FPC) solution is preferable. However, its cost linearly increases with the number of antennas. For this reason, when the application requires many elements, a multiplexed solution can be adopted, even if the performance deteriorates at least by a factor M (the number of antenna elements). In order to counteract the noise floor increase, a hybrid solution can be adopted. The hardware impairments that can affect the performance with the different architectures have been described. In the numerical results we have compared the performance of 3 architectures: FP, FPC, and code-multiplexed (CMX). We have shown that the coherent solution reaches the best performance. However, its accuracy is mainly limited by both mutual coupling and I&Q imbalance effects.

8.5 DoA Estimation with Multipath Propagation

We have proposed a DoA estimation algorithm for frequency selective channels. This method exploits the CP-OFDM transmission scheme, and performs a coarse synchronization to locate the OFDM symbol start, a channel estimation, and a threshold-based fine synchronization that exactly locates the first arrival path (FAP). These steps are included into the synchronization algorithm proposed by Minn et al. [78], whose timing metrics have been modified to comprise the case of a multiple antenna receiver. Once we have located the FAP component, a single source DoA estimator algorithm can be used. Several numerical results have confirmed the robustness of this method, also when LOS and NLOS paths overlap. In this case, when the factor K (the ratio between the power of the LOS path and the total power of the NLOS rays that overlap the LOS) is lower than approximately 7 dB and the angular spread (AS) is limited (up to 20 deg in our simulation results), we have proposed to use our

method with smooth-MUSIC, while for higher values of K we have shown that our DoA estimator (that has lower complexity than smooth-MUSIC) exhibits better performance.

Chapter 9

Appendix

9.1 Measurement Setup for the Characterization of Receiver Gain and Bandwidth

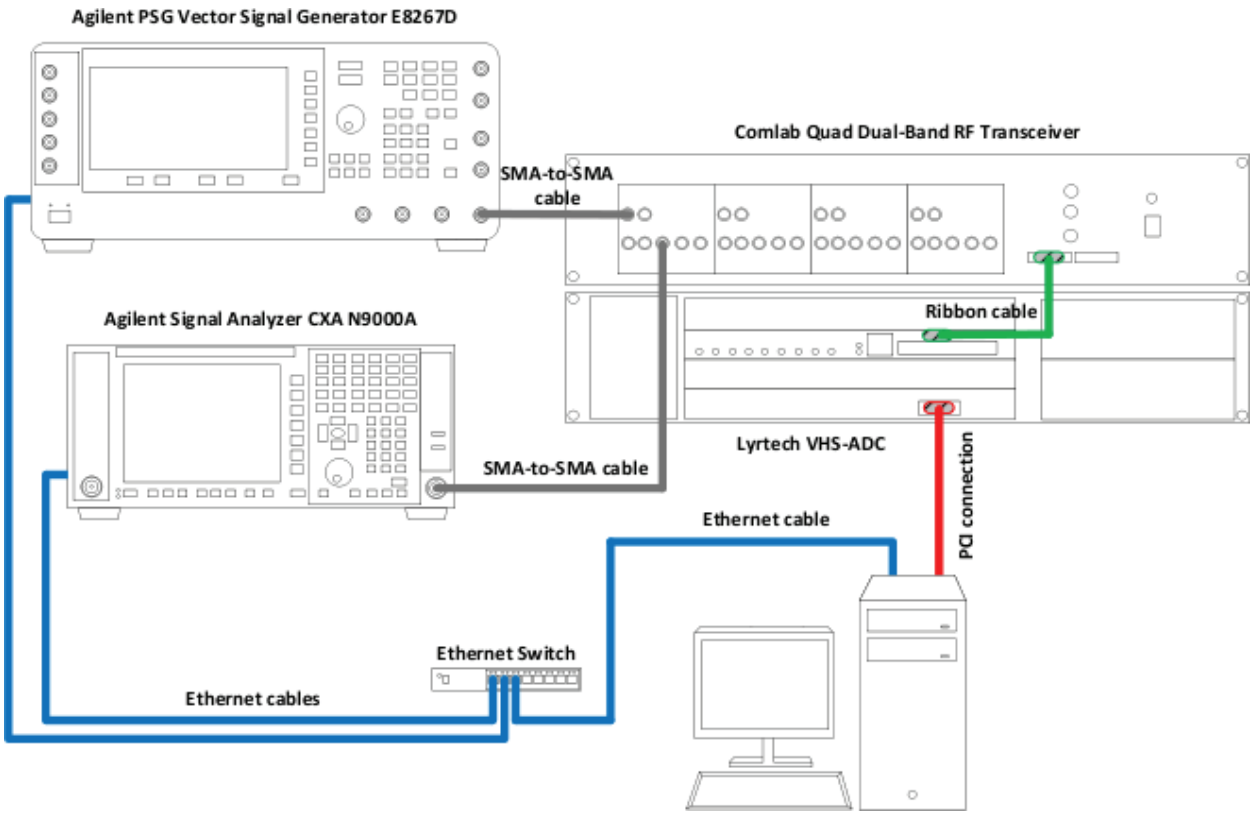

Figure 9.1: Measurement setup for the characterization of both gain and bandwidth.

The measurement setup for the characterization of both gain and bandwidth, shown in Fig. 9.1, is composed by the following equipments:

- Agilent PSG Vector Signal Generator E8267D;

- Agilent Signal Analyzer CXA N9000A.

The signal generator feds the RF input channel of one receiver of the quad dual-band RF transceiver with a single tone signal at the frequency $f_c + f_{bb}$, where $f_c = 2.412$ GHz is the carrier frequency, while f_{bb} has been chosen as $f_{bb} = 1$ MHz. After that, the signal analyzer measures the power $P_{r,dBm}$ (in dBm) of the downconverted signal at the frequency f_{bb}. The signal analyzer has been set with resolution bandwidth RBW equal to 10 kHz.

Next, the signal generator is directly connected to the signal analyzer that measures the effective power of the single tone signal, $P_{t,dBm}$. It should be noted that the SMA-to-SMA cable used to perform the RF connection between the signal generator and the receiver has to be the same used to connect the signal generator to the signal analyzer; in this way, its attenuation does not alter the measurement.

Finally, the receiver gain can be obtained as $G_{dB} = P_{r,dBm} - P_{t,dBm}$. The bandwidth, instead, is found looking for the baseband frequency f_{bb} that corresponds to a 3 dB reduction of the gain w.r.t. the value found at $f_{bb} = 1$ MHz.

The gain (and the bandwidth) has been measured on both the I&Q outputs, and for all the receiver.

9.2 Noise Figure Measurement Setup

The noise figure measurement setup is shown in Fig. 9.2. The RF input of each receiver

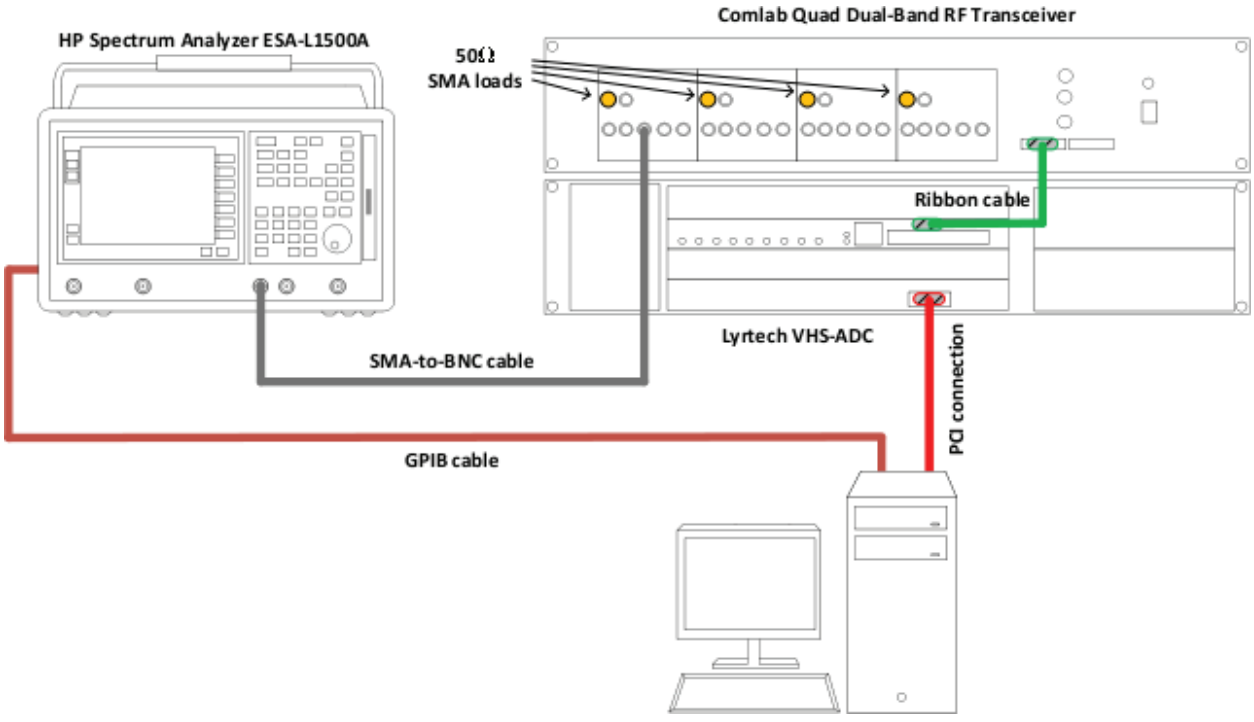

Figure 9.2: Noise figure measurement setup.

is connected to a 50Ω load. The output (both I&Q paths have been measured), instead,

is connected to the input of the spectrum analyzer, HP Spectrum Analyzer ESA L-1500A, that is set with resolution bandwidth RBW of 30 kHz.

The *display average noise level* (DANL), i.e., the noise floor level displayed by the spectrum analyzer, can be expressed as

$$\text{DANL [dBm]} = -174 \text{ dBm/Hz} + 10\log_{10}(\text{RBW}) + \text{NF}_{tot,\text{dB}} + G_{\text{dB}}, \tag{9.1}$$

where -174 dBm/Hz is the thermal noise contribute due to the 50Ω load, $\text{NF}_{tot,\text{dB}}$ is the noise figure (in dB) of the cascade of the receiver and the spectrum analyzer, while G_{dB} is the receiver gain (in dB) previously measured. The noise figure of the cascade of the receiver and the spectrum analyzer can be written, for linear quantity, as

$$\text{NF}_{tot} = \text{NF} + \frac{\text{NF}_{sa} - 1}{G}, \tag{9.2}$$

where NF is the noise figure of the receiver, NF_{sa} is the noise figure of the spectrum analyzer, while G is the receiver gain, i.e., $G = 10^{G_{dB}/10}$. The above equation, called Friis formula [29], can be used to obtain the receiver noise figure, NF. It should be noted that the noise figure of the spectrum analyzer is equal to $\text{NF}_{sa,\text{dB}} = 27$ dB.

9.3 Background Noise Measurement Setup

The background noise measurement setup is shown in Fig. 9.3. The RF input of each

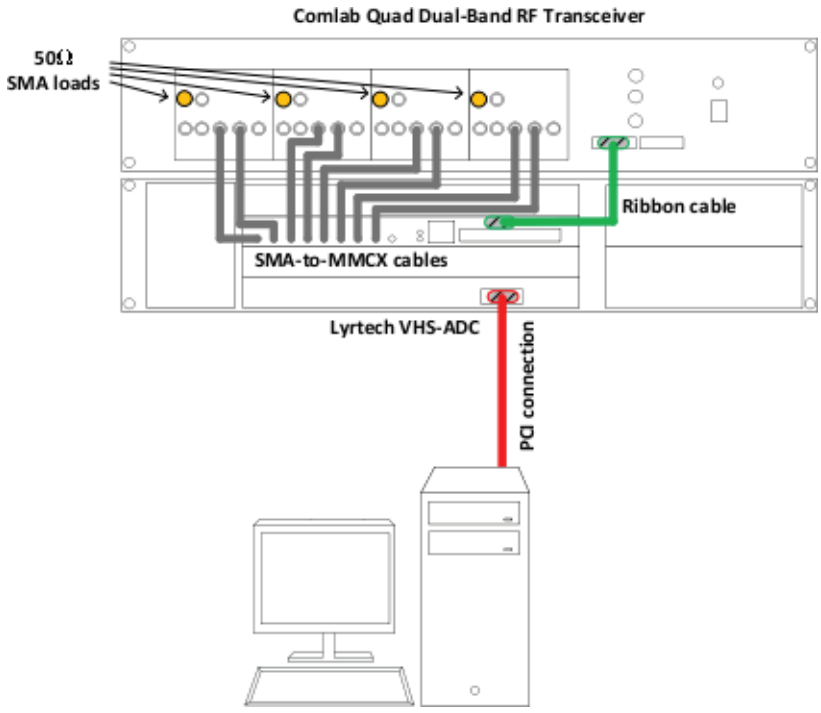

Figure 9.3: Background noise measurement setup.

receiver is connected to a 50Ω load. The I&Q outputs, instead, are connected to the ADC inputs of the Lyrtech VHS-ADC acquisition board.

We have acquired $N = 1024$ samples per channel, and we have computed the background noise power (in dBV) as

$$N_{0,dBV} = 10\log_{10}\left(\frac{1}{N}\sum_{n=0}^{N-1}|x(nT) - \mu_x|^2\right), \qquad \mu_x = \frac{1}{N}\sum_{n=0}^{N-1}x(nT), \tag{9.3}$$

where $x(nT) = x_I(nT) + jx_Q(nT)$.

9.4 DC Offset and Signal-to-DC Offset (SDR) Measurement Setup

The DC offset measurement setup is shown in Fig. 9.4. The signal generator, Agilent PSG

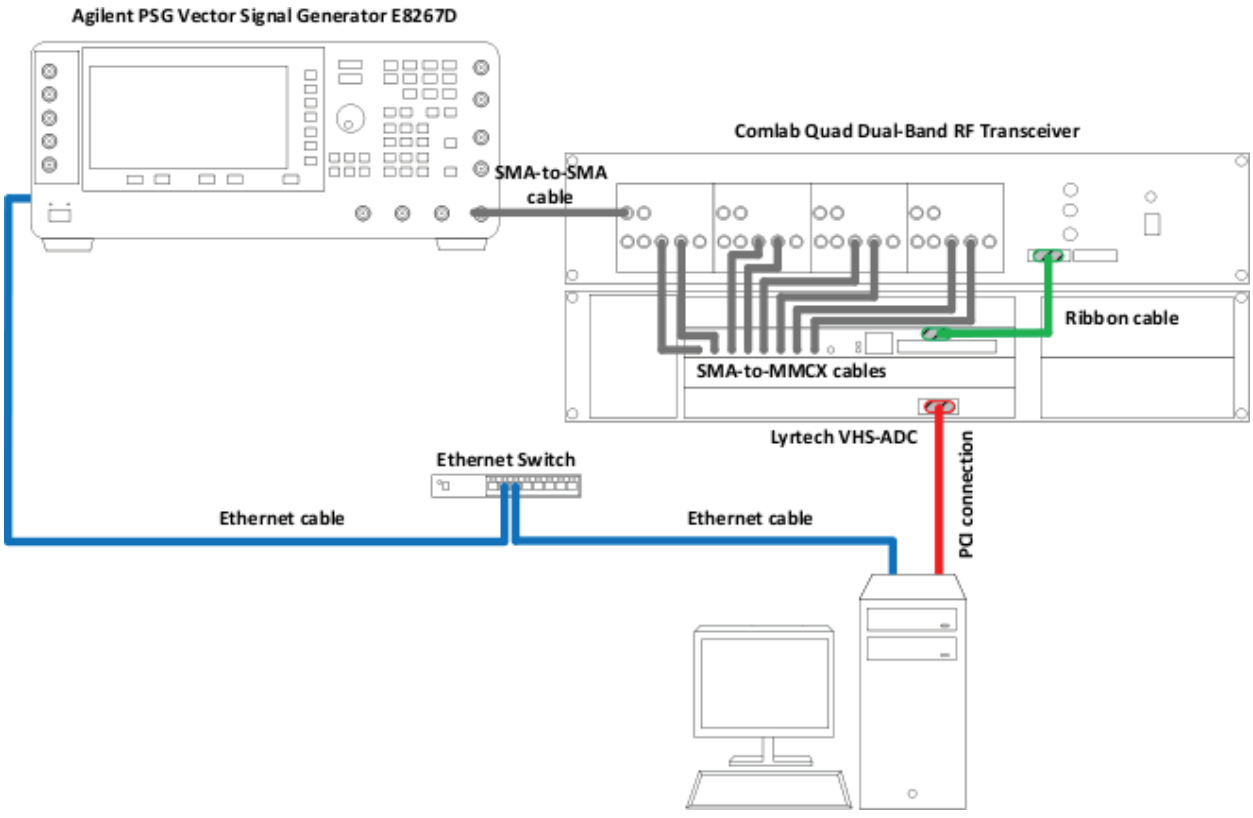

Figure 9.4: DC offset measurement setup.

Vector Signal Generator E8267D, is connected to the RF input of each receiver with a SMA-to-SMA cable. This cable has to be chosen as short as possible. The I&Q outputs, instead, are connected to the ADC inputs of the Lyrtech VHS-ADC acquisition board.

Performing a fast Fourier transform (FFT) unilateral spectrum (the FFT is computed on N acquired samples, and only a half of the FFT points N_{fft} are taken, while the amplitudes are multiplied by two), we measure the power (in V^2) of the DC offset (at zero frequency) and the power of the injected single tone signal (at baseband frequency f_{bb}). We have considered the following parameters: $N = 1024$, $N_{fft} = 1024$, $f_{bb} = 1$ MHz.

9.5 Measurement Setup for Phase Offset, Carrier Frequency Offset, and Phase Noise Characterization

We have considered the measurement setup shown in Fig. 9.5. It is composed by the following equipments:

- Agilent PSG Vector Signal Generator E8267D;
- Agilent Infiniium DSO 91304A.

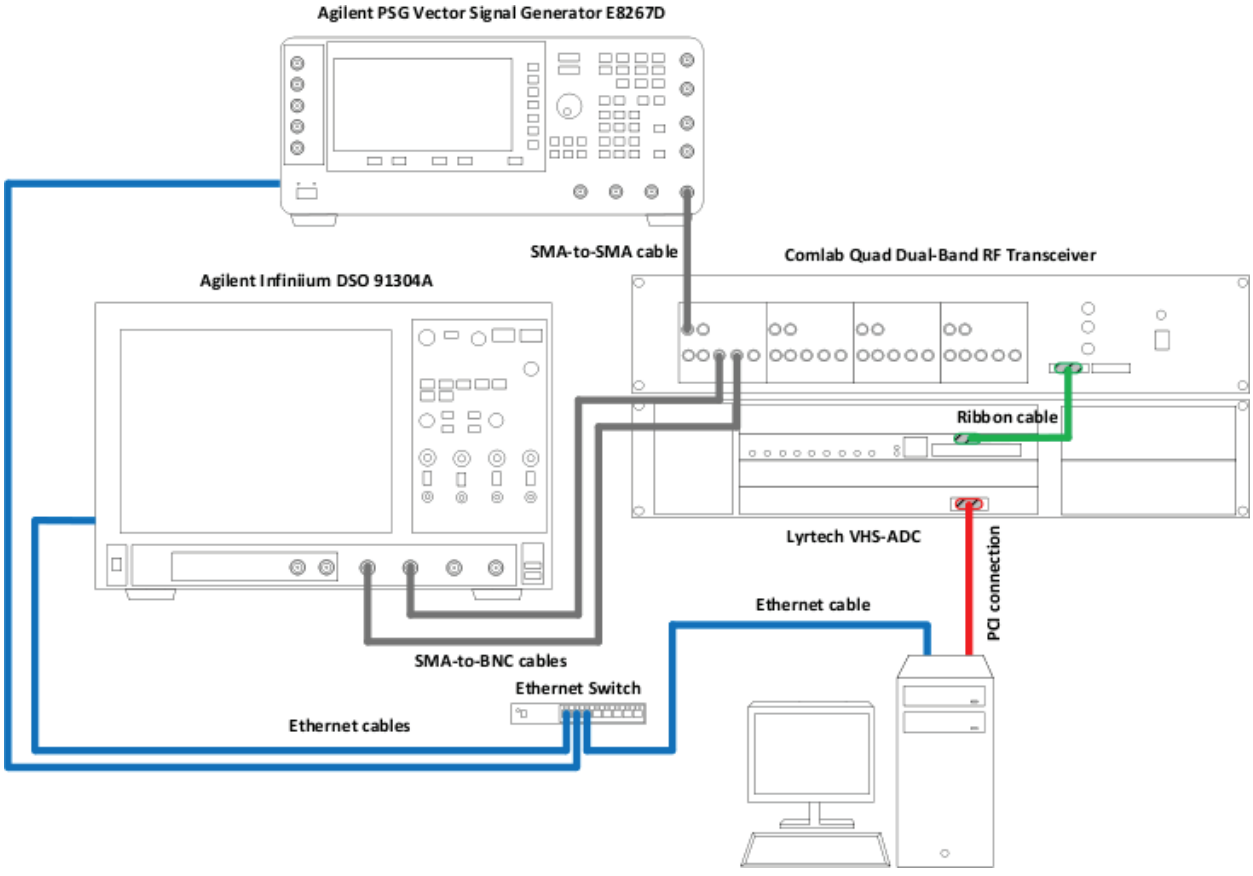

Figure 9.5: Measurement setup for the characterization of phase and carrier frequency offset, and phase noise using a digital oscilloscope.

An RF single tone signal at the nominal carrier frequency $f_c = 2.412$ GHz is generated by the signal generator that is connected to the input of one receiver of the quad dual-band

transceiver with a short SMA-to-SMA cable. Then, the I&Q outputs are connected to two inputs of the Infiniium oscilloscope that stores 10000 samples per channel at 1 MS/s (Mega samples per second). These sample traces, $x_I(nT)$ and $x_Q(nT)$, are then processed to obtain the signal $x(nT) = x_I(nT) + jx_Q(nT)$ that is used to obtain firstly the phase offset and the carrier frequency offset as described in Chapter 2, and to compute the periodogram that shows the phase noise spectrum.

For what the phase noise concerns, it is also characterized using the spectrum analyzer HP Spectrum Analyzer ESA L-1500A, as shown in Fig. 9.6. The resolution bandwidth RBW is set to 10 kHz.

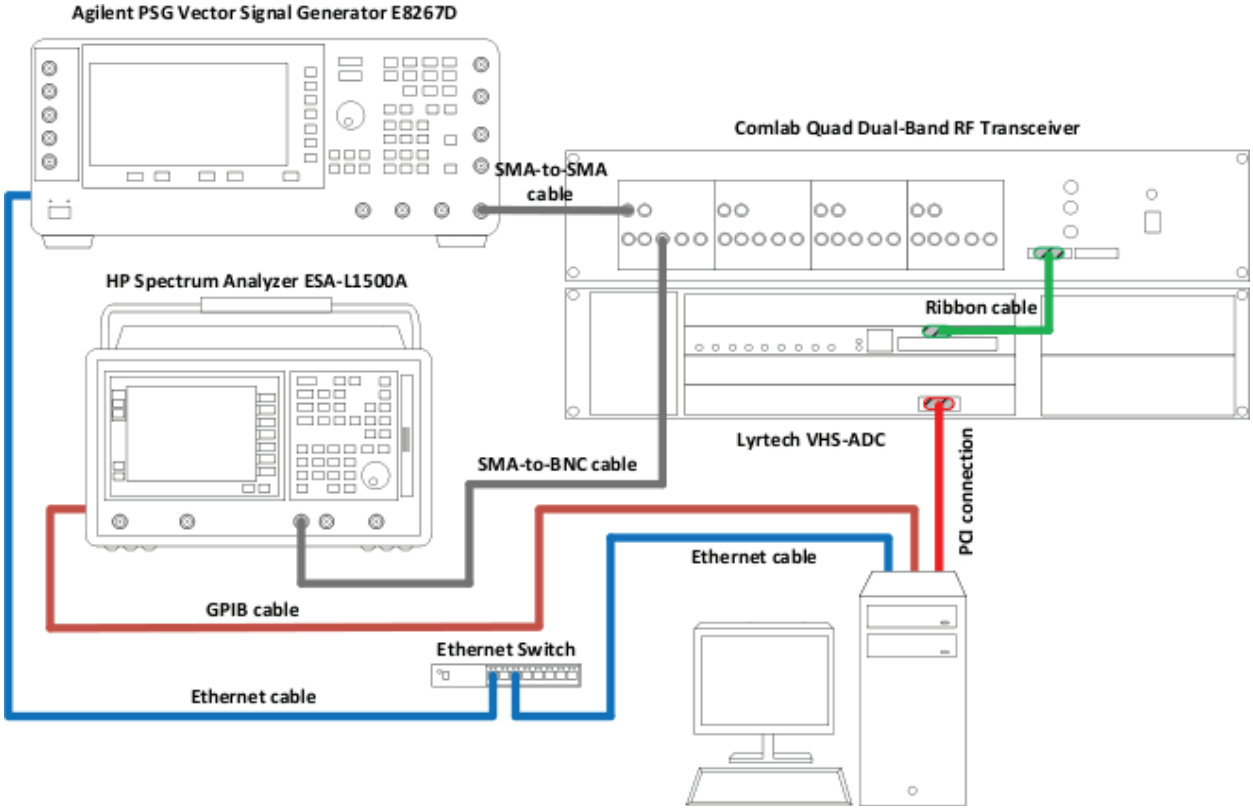

Figure 9.6: Measurement setup for the characterization of the phase noise using a spectrum analyzer.

9.6 Measurement Setup for the Characterization of the ADC Non Linearity

The ADC non linearity has been measured with the setup in Fig. 9.7. A waveform signal generator, the Agilent Pulse Function Arbitrary Generator 81150A , has been used to generate a single tone signal at the frequency 1.26955 MHz. This signal is injected to each ADC input, and the acquired samples (at sampling frequency $F_s = 26$ MHz) are processed

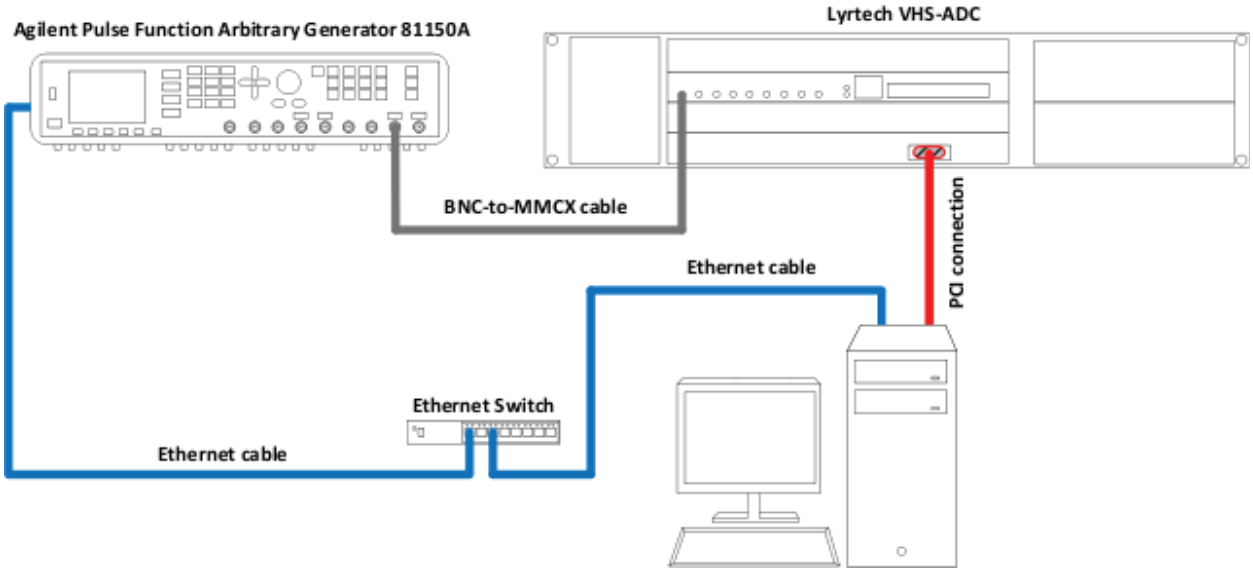

Figure 9.7: Measurement setup for the ADC non linearity characterization.

to obtain the unilateral FFT spectrum. The number of FFT points is equal to the number of acquired samples, i.e., $N_{fft} = N = 1024$.

9.7 Cramer-Rao Bound for the Carrier Frequency Offset Estimator

We have evaluated herein the Cramer-Rao bound for the carrier frequency offset estimation from the signal in (5.9), neglecting both the phase offset and the phase noise, and under the assumption that we do not know either the statistics of $\Delta f^{(i)}$ or the statistics of $A(nT)$. Furthermore, for the sake of simplicity, in the notation we do not report the apex (i).

The unknown parameters are the carrier frequency offset Δf, and the values of the signal amplitude $|A(nT)|^2,\ n \in \{0, .., N_{CFO} - 1\}$. Then, the vector of the unknown parameters can be defined as $\theta = [\Delta f, |A(0)|^2, .., |A((N_{CFO} - 1)T)|^2]$.

At this point we can define the probability density function of the vector $\mathbf{\Lambda} = [\Lambda(0), .., \Lambda((N_{CFO} - 1)T)]$ conditioned by the unknown parameters θ as

$$p(\mathbf{\Lambda}|\theta) = \prod_{n=0}^{N_{CFO}-1} \frac{1}{\pi\sigma_W} \times \exp\left\{ \frac{1}{\sigma_W^2} \left| \Lambda(nT) - |A(nT)|^2 e^{j2\pi\Delta f nT} \right|^2 \right\} \tag{9.4}$$

and the log-likelihood function $L(\theta)$ obtained by applying the logarithm on $p(\mathbf{\Lambda}|\theta)$ and

neglecting the constant terms,

$$\begin{aligned} L(\theta) = \frac{1}{\sigma_W^2} \sum_{n=0}^{N_{CFO}-1} & \Lambda(nT)|A(nT)|^2 e^{-j2\pi\Delta f nT} \\ & + \Lambda(nT)^*|A(nT)|^2 e^{j2\pi\Delta f nT} - |A(nT)|^4. \end{aligned} \tag{9.5}$$

After calculating the derivatives and evaluating their expectation we obtain

$$E\left\{\frac{\partial^2 L(\theta)}{\partial\theta_i \partial\theta_j}\right\} = 0, \ i \neq j, \tag{9.6}$$

which allows evaluating the Cramer-Rao bound as

$$\begin{aligned} CRB(\Delta f) &= -\frac{1}{E\left\{\frac{\partial^2 L(\theta)}{\partial\theta_1^2}\right\}} \\ &\approx \frac{3}{(2\pi T)^2 \gamma_\Lambda N_{CFO}(N_{CFO}-1)(2N_{CFO}-1)}, \end{aligned} \tag{9.7}$$

where γ_Λ is the approximated signal to noise ratio of the signal in (5.9) (we have approximated $|A(nT)|^4$ as a constant). We have also used $\sum_{n=0}^{N-1} n^2 = \frac{N(N-1)(2N-1)}{6}$.

Bibliography

[1] G. Sun, J. Chen, W. Guo, and K. J. R. Liu, "Signal processing techniques in network-aided positioning: A survey of state-of-the-art positioning designs," *IEEE Signal Processing Mag.*, vol. 12, July 2005.

[2] K. W. Cheung, H. C. So, W.-K. Ma, and Y. T. Chan, "A constrained least squares approach to mobile positioning: Algorithms and optimality," *EURASIP Journal on Applied Signal Processing*, vol. 2006, pp. 1–13, 2005.

[3] H. Liu, H. Darabi, P. Banerjee, and J. Liu, "Survey of wireless indoor positioning techniques and systems," *IEEE Trans. Syst., Man, Cybern. C*, vol. 37, pp. 1067–1080, Nov. 2007.

[4] X. Li, "RSS-based location estimation with unknown pathloss model," *IEEE Trans. Wireless Commun.*, vol. 5, Dec. 2006.

[5] M. Laaraiedh, S. Avrillon, and B. Uguen, "Enhancing positioning accuracy through RSS based ranging and weighted least square approximation," in *Proc. of the International Conference on Positioning and Context-Awareness (POCA), Antwerpen, Belgique*, 2009.

[6] S. Gezici, Z. Tian, G. B. Giannakis, H. Kobayashi, A. F. Molisch, H. V. Poor, and Z. Sahinoglu, "Localization via ultra-wideband radios: A look at positioning aspects of future sensor networks," *IEEE Signal Processing Mag.*, pp. 70–84, July 2005.

[7] I. Guvenc, S. Gezici, and Z. Sahinoglu, "Ultra-wideband range estimation: Theoretical limits and practical algorithms," in *Proc. of the IEEE International Conference on Ultra-Wideband (ICUWB'08)*, vol. 3, pp. 93–96, Sept. 2008.

[8] S. Gezici and H. V. Poor, "Position estimation via ultra-wide-band signals," *Proc. IEEE*, vol. 97, Feb. 2009.

[9] S. Wu, Q. Zhang, R. Fan, and N. Zhang, "Match-filtering based TOA estimation for IR-UWB ranging systems," in *Proc. of the International Wireless Communications and Mobile Computing Conference (IWCMC'08)*, pp. 1099–1105, Aug. 2008.

[10] I. Guvenc, Z. Sahinoglu, A. F. Molisch, and P. Orlik, "Non-coherent TOA estimation in IR-UWB systems with different signal waveforms," in *Proc. of the 2nd International Conference on Broadband Networks (BroadNets 2005)*, vol. 2, pp. 1168–1174, Oct. 2005.

[11] I. Guvenc and Z. Sahinoglu, "Threshold-based TOA estimation for impulse radio UWB systems," in *Proc. of the IEEE International Conference on Ultra-Wideband (ICUWB'05)*, pp. 420–425, 2005.

[12] D. Dardari, C.-C. Chong, and M. Z. Win, "Analysis of threshold-basaed TOA estimators in UWB channels," in *Proc. of the 14th European Signal Processing Conference (EUSIPCO 2006), Florence, Italy*, Sept. 2006.

[13] M. Dashti, M. Ghoraishi, and J. ichi Takada, "Optimum threshold for ranging based on ToA estimation error analysis," in *Proc. of the 20th IEEE International Symposium on Personal, Indoor and Mobile Radio Communications (PIMRC 2009), Tokyo*, pp. 988–992, Sept. 2009.

[14] H. Krim and M. Viberg, "Two decades of array signal processing research," *IEEE Signal Processing Mag.*, vol. 13, pp. 67–94, July 1996.

[15] A. B. Gershman, M. Rübsamen, and M. Pesavento, "One- and two- dimensional direction-of-arrival estimation: an overview of search-free techniques," *Signal Processing*, vol. 90, pp. 1338–1349, 2010.

[16] R. O. Schmidt, "Multiple emitter location and signal parameter estimation," *IEEE Trans. Antennas Propagat.*, vol. AP-34, pp. 276–280, Mar. 1986.

[17] R. Roy and T. Kailath, "ESPRIT - estimation of signal parameters via rotational invariance," *IEEE Trans. Acoust., Speech, Signal Processing*, vol. 37, pp. 984–995, July 1989.

[18] H. K. Hwang, Z. Aliyazicioglu, M. Grice, and A. Yakovlev, "Direction of arrival estimation using a root-MUSIC algorithm," in *Proc. of International MultiConference of Engineers and Computer Scientists, IMECS 2008*, Mar. 2008.

[19] M. Haardt and J. A. Nossek, "Unitary ESPRIT: How to obtain increased estimation accuracy with a reduced computational burden," *IEEE Trans. Signal Processing*, vol. 43, May 1995.

[20] H. Nguyen and H. L. V. Trees, "Comparison of performance bounds for DOA estimation," in *Proc. of the 7th IEEE Workshop on Statistical Signal and Array Processing*, pp. 313–316, June 1994.

[21] T. J. Shan, M. Wax, and T. Kailath, "On spatial smoothing for direction-of-arrival estimation of coherent signals," *IEEE Trans. Acoust., Speech, Signal Processing*, vol. ASSP-33, no. 4, pp. 806–811, 1985.

[22] T. T. Williams, S. Prasad, A. K. Mahalanabis, and L. H. Sibul, "An improved spatial smoothing technique for bearing estimation in a multipath environment," *IEEE Trans. Acoust., Speech, Signal Processing*, vol. ASSP-36, pp. 425–432, Apr. 1988.

[23] M. C. Vanderveen, C. B. Papadias, and A. Paulraj, "Joint angle and delay estimation (JADE) for multipath signals arriving at an antenna array," *IEEE Commun. Lett.*, Jan. 1997.

[24] S. Yoo, S. Kim, D. H. Youn, and C. Lee, "Multipath mitigation technique using null-steering beamformer for positioning system," in *Proc. IEEE 57th Vehicular Technology Conference Spring, VTC 2003-Spring*, Apr. 2003.

[25] W. D. Wirth, "Direction of arrival estimation with multipath scattering by space-time processing," *Signal Processing*, vol. 84, pp. 1677–1688, 2004.

[26] M. Cedervall and R. L. Moses, "Efficient maximum likelihood DOA estimation for signals with known waveforms in the presence of multipath," *IEEE Trans. Signal Processing*, vol. 45, Mar. 1997.

[27] Lyrtech (Nutaq). Website online at `http://nutaq.com`.

[28] Analog Devices, "14-bit, 80 MSPS/105 MSPS A/D converter AD6645," tech. rep., One Technology Way, P.O. Box 9106, Norwood, MA 02062-9106, U.S.A. Available online at `http://www.analog.com`.

[29] B. Razavi, *RF Microelectronics*. Prentice Hall Communications Engineering and Emerging Technologies, 1998.

[30] Maxim, "Single-/Dual-band 802.11a/b/g world-band transceiver ICs," tech. rep., 2004. Available online at `http://www.maxim-ic.com/datasheet/index.mvp/id/4532`.

[31] P. B. Kenington, *RF and Baseband Techniques for Software Defined Radio*. Norwood, MA 02062: Artech House, 2005.

[32] S. H. Han and J. H. Lee, "An overview of peak-to-average power ratio reduction techniques for multicarrier transmission," *IEEE Wireless Communications*, pp. 56–65, Apr. 2005.

[33] B. Lindoff and P. Malm, "BER performance analysis of a direct conversion receiver," *IEEE Trans. Commun.*, vol. 50, pp. 856–865, May 2002.

[34] P. Robertson and S. Kaiser, "Analysis of the effect of phase-noise in orthogonal frequency division multiplex (OFDM) system," in *Proc. IEEE ICC'95, Seattle*, June 1995.

[35] K. R. Dandekar, H. Ling, and G. Xu, "Smart antenna array calibration procedure including amplitude and phase mismatch and mutual coupling effects," in *Proc. IEEE International Conference on Personal Wireless Communications (ICPWC 2000)*, pp. 293–297, 2000.

[36] M. P. Wylie, S. Roy, and H. Messer, "Joint DOA estimation and phase calibration of linear equispaced (LES) arrays," *IEEE Trans. Signal Processing*, vol. 42, pp. 3449–3459, Dec. 1994.

[37] A. Paulraj and T. Kailath, "Direction of arrival estimation by eigenstructure methods with unknown sensor gain and phase," in *Proc. IEEE International Conference on Acoustics, Speech and Signal Processing (ICASSP'88)*, (New York City), pp. 2681–2684, Apr. 1988.

[38] I. J. Gupta, J. R. Baxter, S. W. Ellingson, H.-G. Park, H. S. Oh, and M. G. Kyeong, "An experimental study of antenna array calibration," *IEEE Trans. Antennas Propagat.*, vol. 51, no. 3, 2003.

[39] Y. Inoue and H. Arai, "Effect of mutual coupling and manufacturing error of array for DOA estimation of ESPRIT algorithm," *Electronics and Communications in Japan, Part I Communications*, vol. 89, no. 9, pp. 68–75, 2006.

[40] J. G. Proakis, *Digital Communications*. New York: McGraw Hill, 3rd ed., 1995.

[41] H. Meyr, M. Moeneclaey, and S. A. Fetchel, *Digital Communication Receivers: Synchronization, Channel Estimation, and Signal Processing*. New York: Wiley-Interscience, 2nd ed., 1997.

[42] C. Reck, U. Berold, J. Weinzierl, and L. P. Schmidt, "Direction of arrival estimation from secondary surveillance radar signals in presence of hardware imperfections," in *Proc. of the 5th European Radar Conference*, Oct. 2008.

[43] Y. Hua, T. K. Sarkar, and D. D. Weiner, "An L-shaped array for estimating 2-D directions of wave arrival," *IEEE Trans. Antennas Propagat.*, vol. 39, pp. 143–146, Feb. 1991.

[44] T. Kaiser, A. Bourdoux, H. Boche, J. R. Fonollosa, J. B. Andersen, and W. Utschick, *Smart antennas: State of the art, Eurasip Book Series in Signal Processing and Communications*. Hindawi Publishing Corporation, 2005.

[45] R. M. Rao, W. Zhu, S. Lang, C. Oberli, D. Browne, J. Bhatia, J.-F. Frigon, J. Wang, P. Gupta, H. Lee, D. N. Liu, S. G. Wong, M. Fitz, B. Daneshrad, and O. Takeshita, "Multi-antenna testbeds for research and education in wireless communications," *IEEE Communications Magazine*, pp. 72–81, Dec. 2004.

[46] M. Rupp, S. Caban, and C. Mehlführer, "Challenges in bulding MIMO testbeds," in *Proc. of the European Signal Processing Conference (EUSIPCO), Poznan*, 2007.

[47] M. Rupp, C. Mehlführer, and S. Caban, "Testbeds and rapid prototyping in wireless system design," *EURASIP Newsletter*, vol. 17, pp. 32–50, Sept. 2006.

[48] J. A. García-Naya, M. González-López, and L. Castedo, "An overview of MIMO testbed technology," in *Proc. of the 4th International Symposium on Image/Video Communications over Fixed and Mobile Networks (ISIVC '08)*, July 2008.

[49] Signalion GmbH. Website online at `http://www.signalion.com`.

[50] D. Bates, S. Henriksen, B. Ninness, and S. R. Weller, "A 4×4 FPGA-based wireless testbed for LTE applications," in *Proc. of IEEE 19th International Symposium on Personal, Indoor and Mobile Radio Communications, (PIMRC 2008)*, Sept. 2008.

[51] S. Caban, C. Mehlführer, R. Langwieser, A. L. Scholtz, and M. Rupp, "Vienna MIMO testbed," *EURASIP Journal on Applied Signal Processing*, vol. 2006, no. Article ID 54868, pp. 1–13, 2006.

[52] S. Lang, R. M. Rao, and B. Daneshrad, "Design and development of a 5.25 GHz software defined wireless OFDM communication platform," *IEEE Communications Magazine, Radio Communications Supplement*, pp. 6–12, June 2004.

[53] P. Gupta, W. Zhu, M. P. Fitz, H. Lee, D. N. Liu, and S. W. G. Wong, "Field test results for space-time coding," in *Proc. of the Thirty-Seventh Asilomar Conference on Signals, Systems and Computers*, Nov. 2003.

[54] K. S. Bialkowski, A. Postula, A. Abbosh, and M. E. Bialkowski, "2×2 MIMO testbed for dual 2.4 GHz/5 GHz band," in *Proc. of International Conference on Electromagnetics in Advanced Applications, (ICEAA 2007)*, 2007.

[55] S. Caban, C. Mehlfürer, L. W. Mayer, and M. Rupp, "2×2 MIMO at variable antenna distances," in *Proc. of Vehicular Technology Conference*, 2008.

[56] D. Kim and M. Torlak, "Rapid prototyping of a cost effective and flexible 4×4 MIMO testbed," in *Proc. of IEEE 5th Sensor Array and Multichannel Signal Processing Workshop, (SAM 2008)*, July 2008.

[57] P. G. Jr., R. Hang, D. Truhachev, and C. Schlegel, "A portable MIMO testbed and selected channel measurements," *EURASIP Journal on Applied Signal Processing*, vol. 2006, no. Article ID 51490, pp. 1–11, 2006.

[58] A. G. i Fàbregas, M. Guillaud, D. T. M. Slock, G. Caire, K. Gosse, S. Rouquette, A. R. Dias, P. Bernardin, X. Miet, J.-M. Conrat, Y. Toutain, A. Peden, and Z. Li, "A MIMO-OFDM testbed for wireless local area networks," *EURASIP Journal on Applied Signal Processing*, vol. 2006, no. Article ID 18083, pp. 1–20, 2006.

[59] Agilent Technologies, "Agilent E8267D PSG vector signal generator datasheet," tech. rep., Feb. 2012. Available online at `http://cp.literature.agilent.com/litweb/pdf/5989-0697EN.pdf`.

[60] T. Cooper, J. McCormack, R. Farrell, and G. Baldwin, "Toward scalable, automated tower-top phased array calibration," in *Proc. of the IEEE 65th Vehicular Technology Conference (VTC 2007 Spring), Dublin, Ireland*, 2007.

[61] P. Cherntanomwong, J. Takada, H. Tsuji, and R. Miura, "Array calibration using measured data for precise angle-of-arrival estimation," in *Proc. of WPMC 2005, Aalborg, Denmark*, 2005.

[62] D. Zeyang and D. Yuming, "Fast active calibration for uniform linear array with amplitude and phase errors," in *Proc. of the 2009 International Workshop on Information Security and Application (IWISA 2009), Qingdao, China*, 2009.

[63] C. Wang and J. A. Cadzow, "Direction-finding with sensor gain, phase and location uncertainty," in *Proc. IEEE International Conference on Acoustics, Speech and Signal Processing (ICASSP'91)*, pp. 1429–1432, July 1991.

[64] Q. Xu, H. H. Tao, and G. S. Liao, "Array gain and phase error correction based on GA," *Systems Engineering and Electronics*, vol. 28(5), pp. 654–657, 2006.

[65] B. H. Wang, Y. L. Wang, and H. Chen, "Array calibration of angularly dependent gain and phase uncertainties with instrumental sensors," in *Proc. of IEEE International Symposium on Phased Array Systems and Technology, Boston, Massachusetts, USA*, 2003.

[66] L. Bing and L. Guisheng, "Method for array gain and phase uncertainties calibration based on ISM and ESPRIT," *Journal of Systems Engineering and Electronics*, vol. 20(2), pp. 223–228, 2009.

[67] Y. Shimada, H. Yamada, and Y. Yamaguchi, "Blind array calibration technique using ICA," in *Proc. of ISAP 2007, Niigata, Japan*, 2007.

[68] R. B. Ertel, P. Cardieri, K. W. Sowerby, T. S. Rappaport, and J. H. Reed, "Overview of spatial channel models for antenna array communications systems," *IEEE Personal Commun. Mag.*, pp. 10–22, Feb. 1998.

[69] D. M. Pozar, *Microwave Engineering*. John Wiley and Sons, 1997.

[70] A. A. Abidi, "Direct-conversion radio transceivers for digital communication," *IEEE Journal on Solid-State Circuits*, vol. 30, pp. 1399–1410, Dec. 1995.

[71] E. Tuncer and B. Friedlander, *Classical and Modern Direction-of-Arrival Estimation*. Burlington, MA: Academic Press, 2009.

[72] A. Mohammadi and F. M. Ghannouchi, "Single RF front-end MIMO transceivers," *IEEE Communication Magazine*, pp. 104–109, Dec. 2001.

[73] F. Tzeng, A. Jahanian, D. Pi, and P. Heydari, "A CMOS code-modulated path-sharing multi-antenna receiver front-end," *IEEE Journal on Solid-State Circuits*, vol. 44, pp. 1321–1335, May 2009.

[74] G. Krishnamurthy and K. G. Gard, "Time division multiplexing front-ends for multi-antenna integrated wireless receivers," *IEEE Transactions on Circuits and Systems I*, vol. 57, pp. 1231–1243, June 2010.

[75] T. T. Zhang, H. T. Hui, and Y. L. Lu, "Compensation for the mutual coupling effect in the ESPRIT direction finding algorithm by using a more effective method," *IEEE Transactions on Antennas and Propagation*, vol. 53, pp. 1552–1555, Apr. 2005.

[76] Z. Liu, Z. Huang, F. Wang, and Y. Zhou, "DOA estimation with uniform linear arrays in the presence of mutual coupling via blind calibration," *Signal Processing*, vol. 89, pp. 1446–1456, 2009.

[77] M. Valkama, M. Renfors, and V. Koivunen, "Advanced methods for I&Q imbalance compensation in communication receivers," *IEEE Transactions on Signal Processing*, vol. 49, pp. 2335–2344, Oct. 2001.

[78] H. Minn, V. K. Bhargava, and K. B. Letaief, "A robust timing and frequency synchronization for OFDM systems," *IEEE Trans. Wireless Commun.*, vol. 2, July 2003.

[79] A. A. Nasir, S. Durrani, and R. A. Kennedy, "Performance of coarse and fine timing synchronization in OFDM receivers," in *Proc. 2nd International Conference on Future Computer and Communication, ICFCC 2010*, May 2010.

[80] V. Erceg *et al.*, "TGn channel models," *IEEE P802.11 Wireless LANs*, May 2004. Available online at `http://www.802wirelessworld.com:8802/`.

[81] B. Ottersten, "Array processing for wireless communications," in *Proc. 8th IEEE Signal Processing Workshop on Statistical Signal and Array Processing, Corfu*, pp. 466–473, June 1996.

[82] E. Lagunas, M. Najar, and M. Navarro, "Joint TOA and DOA estimation compliant with IEEE 802.15.4a standard," in *Proc. of 5th International Symposium on Wireless Pervasive Computing (ISWPC), Modena, Italy*, pp. 157–162, May 2010.

[83] L. Taponecco, A. A. D'Amico, and U. Mengali, "Joint TOA and AOA estimation for UWB localization applications," *IEEE Trans. Wireless Commun.*, vol. 10, July 2011.

[84] C. R. N. Athaudage and R. R. V. Angiras, "Sensitivity on FFT-equalized zero-padded OFDM systems to time and frequency synchronization errors," in *Proc. IEEE 16th International Symposium on Personal, Indoor and Mobile Radio Communications, PIMRC 2005*, Sept. 2005.

Curriculum Vitae

Daniele Inserra received the BSc Degree (2007) and the MSc Degree (2009) in electrical engineering both from the University of Udine. Since 2010 is a Ph.D. student in telecommunications. During these years has gained experience in infomobility, wireless and power line communication systems, radio localization and positioning techniques, hardware/software co-design, rapid prototyping methodologies, hardware and RF devices characterization and measurement systems.

Currently, he is a member of the WiPLi Lab, wireless and power line communications laboratory. He is also IEEE member and member of the Circuit and Systems (CAS) and Microwave Theory and Techniques (MTT) societies.